INL/RPT-25-87542

Advanced Reactor Technologies -
Gas-Cooled Reactor Program

Summary Report Of The FY-25 Computational Fluid Dynamics Verification And Validation Exercises In The Advanced Reactor Technologies - Gas-Cooled Reactor Program

SEPTEMBER 2025

Sinan Okyay,
Victor Coppo Leite,
Logan Hiland,
Sierra Tutwiler,
David Reger, and
Gerhard Strydom

Idaho National Laboratory

Battelle Energy Alliance manages INL for the U.S. Department of Energy's Office of Nuclear Energy

INL/RPT-25-87542

Summary Report Of The FY-25 Computational Fluid Dynamics Verification And Validation Exercises In The Advanced Reactor Technologies - Gas-Cooled Reactor Program

Sinan Okyay,
Victor Coppo Leite,
Logan Hiland,
Sierra Tutwiler,
David Reger, and
Gerhard Strydom
Idaho National Laboratory

September 2025

Idaho National Laboratory
Advanced Reactor Technologies - Gas-cooled Reactor Program
Idaho Falls, Idaho 83415

http://www.inl.gov

Prepared for the
U.S. Department of Energy
Office of Nuclear Energy
Under DOE Idaho Operations Office
Contract DE-AC07-05ID14517

Page intentionally left blank

Advanced Reactor Technologies - Gas-cooled Reactor Program

Summary Report of the FY-25 Computational Fluid Dynamics Verification and Validation Exercises in the Advanced Reactor Technologies - Gas-Cooled Reactor Program

INL/RPT-25-87542

September 2025

Technical Reviewer: (Confirmation of mathematical accuracy, and correctness of data and appropriateness of assumptions.)

SUNMING QIN (Affiliate) Digitally signed by SUNMING QIN (Affiliate)
Date: 2025.09.04 12:59:30 -06'00'

Sunming Qin Date
Nuclear Engineer

Approved by:

KIP KLEIMENHAGEN (Affiliate) Digitally signed by KIP KLEIMENHAGEN (Affiliate)
Date: 2025.09.04 14:09:25 -06'00'

Kip L. Kleimenhagen Date
ART Project Manager

TRAVIS MITCHELL (Affiliate) Digitally signed by TRAVIS MITCHELL (Affiliate)
Date: 2025.09.04 13:53:44 -06'00'

Travis R. Mitchell Date
ART Program Manager

MICHELLE SHARP (Affiliate) Digitally signed by MICHELLE SHARP (Affiliate)
Date: 2025.09.04 12:50:21 -06'00'

Michelle T. Sharp Date
INL Quality Assurance

Page intentionally left blank

ABSTRACT

Verification and Validation (V&V) of numerical tools is critical for ensuring reasonable predictions during design, safety analysis, and licensing. Recent work in the Advanced Reactor Technologies - Gas-Cooled Reactor (ART-GCR) program has focused on V&V of common computational fluid dynamics (CFD) tools used within the Untied States. This report presents an update on these CFD V&V activities. The Generation IV Forum (GIF) very high-temperature reactor (VHTR) Computational Methods, Validation, and Benchmarking (CMVB) is an international organization dedicated to the verification and validation of high-temperature gas-cooled reactor (HTGR) simulation tools. Participation in the CMVB adds value to V&V activities, as it allows access to a wider range of data and provides valuable benchmarking exercises. Three HTGR phenomena are targeted: reactor cavity cooling system (RCCS) performance, core bypass flow, and lower plenum mixing. Simulations of the University of Wisconsin-Madison (UW-Madison) RCCS facility were performed with Reynolds-averaged Navier-Stokes (RANS) in StarCCM+. The results are compared for both forced and natural convection conditions, with both exhibiting good agreement with experimental measurements. The Idaho National Laboratory (INL) matched index of refraction (MIR) and Korean Atomic Energy Research Institute (KAERI) bypass flow experiments are used to validate CFD predictions of bypass flow. Simulations are performed with RANS in StarCCM+ and with large-eddy simulation (LES) in NekRS. Finally, preliminary simulations of the Institute of Nuclear and New Energy Technology (INET) lower plenum mixing facilities are presented. Initial work has developed models containing LES, RANS, and porous media models. These preliminary models are presented and compared to each other to gauge differences in predictions when using each of the three methods.

Page intentionally left blank

ACKNOWLEDGMENTS

This research made use of Idaho National Laboratory's computing resources, which are supported by the U.S Department of Energy (DOE) Office of Nuclear Energy and the Nuclear Science User Facilities under contract no. DE-AC07-05ID14517. This work also used resources of the Oak Ridge Leadership Computing Facility at Oak Ridge National Laboratory, which is supported by the DOE Office of Science under contract no. DE-AC05-00OR22725.

Page intentionally left blank

CONTENTS

FIGURES

TABLES

Page intentionally left blank

ACRONYMS

ANL	Argonne National Laboratory
ART-GCR	Advanced Reactor Technologies - Gas-Cooled Reactor
AVR	Arbeitsgemeinschat Versuchsreaktor
CFD	computational fluid dynamics
CMVB	Computational Methods, Validation, and Benchmarking
GA-MHTGR	General Atomics' Modular High-Temperature Gas Reactor
GIF	Generation IV Forum
HTGR	high-temperature gas-cooled reactor
HTR-PM	High Temperature Reactor - Pebble Bed Module
INET	Institute of Nuclear and New Energy Technology
INL	Idaho National Laboratory
KAERI	Korean Atomic Energy Research Institute
LES	large-eddy simulation
LFR	lead-cooled fast reactor
LWR	light-water reactor
MIR	matched index of refraction
NPP	nuclear power plant
NSTF	Natural Convection Shutdown Heat Removal Test Facility
PBMR	pebble-bed modular reactor
PBR	pebble-bed reactor
PIV	particle image velocimetry
RANS	Reynolds-averaged Navier-Stokes
RCCS	reactor cavity cooling system
REV	representative elementary volume
RPV	reactor pressure vessel
SFR	sodium-cooled fast reactor
SNU	Seoul National University

TRISO	tri-structural isotropic
UW-Madison	University of Wisconsin-Madison
V&V	Verification and Validation
VHTR	very high-temperature reactor

Summary Report of the FY-25 Computational Fluid Dynamics Verification and Validation Exercises in the Advanced Reactor Technologies - Gas-Cooled Reactor Program

1. INTRODUCTION

Advanced nuclear reactors have attracted renewed research interest in recent years. The advancement of artificial intelligence and other data center systems has only increased this interest, as these systems afford opportunities to provide a wealth of stable energy solutions for meeting the world's enormous energy needs. Additionally, the U.S. Department of Energy (DOE) has expressed great interest in deployment of advanced reactors to promote American energy independence and stability.

High-temperature gas-cooled reactors (HTGRs) are one of several advanced nuclear reactors being developed currently in the United States. Typically, these reactors are composed primarily of graphite embedded with tri-structural isotropic (TRISO) fuel particles that house the nuclear material. An inert gas, typically helium, serves as the coolant. The operating temperatures for these reactors are in the range of 500°C–900°C, providing efficiency advantages over traditional light-water reactor (LWR) designs and enabling HTGRs to generate process heat for industrial applications.

Currently, a large focus of the Advanced Reactor Technologies - Gas-Cooled Reactor (ART-GCR) methods program is Verification and Validation (V&V) of simulation tools commonly used for HTGR analysis. Experimental facilities for HTGR phenomena are often performed using small-scale separate-effects test facilities, while simulations can provide a broader understanding of reactor performance. Validation of high-fidelity tools is therefore imperative to ensure that simulations are accurately depicting reactor performance. A current focus of the ART-GCR program is the utilization of available separate-effects test facilities to perform validation of commonly used simulation tools in the United States.

This validation effort in ART-GCR is being performed in collaboration with the Generation IV Forum (GIF)-very high-temperature reactor (VHTR) Computational Methods, Validation, and Benchmarking (CMVB) program. The GIF CMVB is an international organization that focuses on validation of computational methods and codes for the simulation of HTGR thermal-hydraulics and other relevant HTGR physics. This international collaboration promotes the exchange of experimental and simulation data for the purpose of validating and verifying the performance of modern simulation tools. Participation in the CMVB has provided the ART-GCR program with additional access to experimental data from international test facilities, providing valuable insight from facilities that would be costly to reproduce within the United States.

Current work within the ART-GCR program is aimed at obtaining a better understanding of several HTGR phenomena identified as being of great importance for HTGR deployment and operation. The phenomena of interest are as follows:

1. **Reactor Cavity Coolant System Performance**: The reactor cavity cooling system (RCCS) acts as the ultimate heat sink for an HTGR during a loss-of-cooling accident. It is therefore imperative that the RCCS be properly modeled so as to inform both design- and safety-related calculations. The RCCS performance is complex, involving natural convection, radiative heat transfer, and other complex phenomena. Validation of RCCS models can provide valuable insight into proper modeling strategies for predicting RCCS performance.

2. **Core Bypass Flow**: In both prismatic and pebble-bed HTGRs, the reflector is made up of stacked graphite blocks. The interfaces between these blocks are imperfect, and small gaps often exist between

the blocks. These gaps provide additional pathways via which the coolant can flow, allowing it to flow around the core rather than through it. Such flow is therefore referred to as "core bypass flow." Core bypass flow is an important phenomenon in HTGR analysis, because the amount of bypass flow can significantly impact the core outlet temperature, as well as the temperature in the reflector. Bypass flow can exceed 10% of the total system mass flow rate, leading to large differences in the coolant's mass flow rate through the core. Due to these large differences, properly predicting core bypass flow is critical for ensuring the accuracy of safety analysis calculations.

3. **Lower Plenum Mixing**: Upon exiting the core, the coolant in a pebble-bed reactor (PBR) enters the lower plenum before proceeding to the steam generator. The coolant temperature at the exit of the core is typically nonuniform, with hotter fluid near the center of the reactor and cooler fluid near the reflector walls. These nonuniformities are undesirable, as they may impact the performance and integrity of the reactor steam generator. Therefore, the lower plenum in an HTGR is designed to promote coolant mixing so as to homogenize the coolant temperature before it leaves the reactor and enters the steam generator. This mixing process is highly complex and difficult to model accurately. And the complex geometry of the lower plenum adds further challenges when simulating lower plenum mixing, as these features can invalidate many assumptions in lower-fidelity models.

This report documents the current progress with ART-GCR in regard to the validation of computational fluid dynamics (CFD) simulation tools by using available experimental data.

2. CODES AND METHODS

Simulation of the multiple experimental facilities covered in this report primarily utilized large-eddy simulation (LES) and Reynolds-averaged Navier-Stokes (RANS) methods. These simulations were performed in the NekRS and StarCCM+ codes, respectively. This section introduces the simulation methods and the codes that were employed.

2.1. Large Eddy Simulations - LES

In LES, the larger 3D turbulent structures are directly resolved, whereas the effects of the smaller scale motions are modeled. There are several ways to achieve this modeling. For the present work, it was achieved by filtering the velocity field when solving the Navier-Stokes equations. The general filtering operation is introduced in [1].

The filter function is homogeneous, (i.e., independent of x). a filtered version of the Navier-Stokes equations can be written, such that the filtered continuity equation is:

$$\nabla \cdot \bar{u} = 0 \tag{1}$$

And the filtered momentum equation is:

$$\frac{\partial \bar{u}}{\partial t} + \nabla \cdot (\bar{u}\bar{u}) = -\frac{1}{\rho}\nabla \bar{p} + \nu \nabla^2 \bar{u} + \nabla \cdot \tau_{\text{SGS}} \tag{2}$$

where $\bar{p}$ is the filtered pressure and τ_{SGS} is the subgrid-scale stress. This term models the turbulent motion in a fluid at scales smaller than the grid [2]. Therefore, it is defined as:

$$\tau_{\text{SGS}} \equiv -(\overline{uu} - \bar{u}\bar{u}) \tag{3}$$

Lastly, in LES, the filter and grid must be sufficient to resolve 80% of the total energy everywhere [3]. Additionally, LES has some criteria in the mesh resolution:

- The mesh resolution in the domain should be sufficient to resolve the Taylor micro-scales defined in following equation:

$$\lambda = \sqrt{\frac{10\nu k}{\epsilon}} \tag{4}$$

  where λ is the Taylor micro-scale, k is the turbulent kinetic energy, ν is the kinematic viscosity, and ϵ is the rate of energy dissipation.
- In wall-resolved LES, the mesh resolution near wall cells must have $y^+ < 1$ to resolve the boundary layer.
- In wall-resolved LES, there should be 10 grid points within the $y^+ < 30$ [4].

2.2. NekRS

NekRS is an open-source CFD solver that utilizes the spectral element method (SEM), a high-order weighted residual technique that combines the geometric flexibility of finite elements with the rapid convergence and computational efficiency of global spectral methods [5]. In the SEM, the solution is represented as Nth-order tensor-product polynomials within each element in a quadrilateral (2D) or hexahedral (3D) conformal mesh, known as p-type refinement finite element methods. The polynomials are constructed at N + 1 Gauss-Lobatto-Legendre (GLL) collocation points, which correspond to nonuniform h-type refinement in finite element methods. Figure 1 shows the differences between the mesh elements and GLL points on the pipe cross-section when using different polynomial orders. NekRS offers solutions that require high computational performance and solution accuracy. Recent work has summarized significant progress, including a full-core simulation of a small modular reactor [6]. The NekRS code was employed to perform LES in the present work.

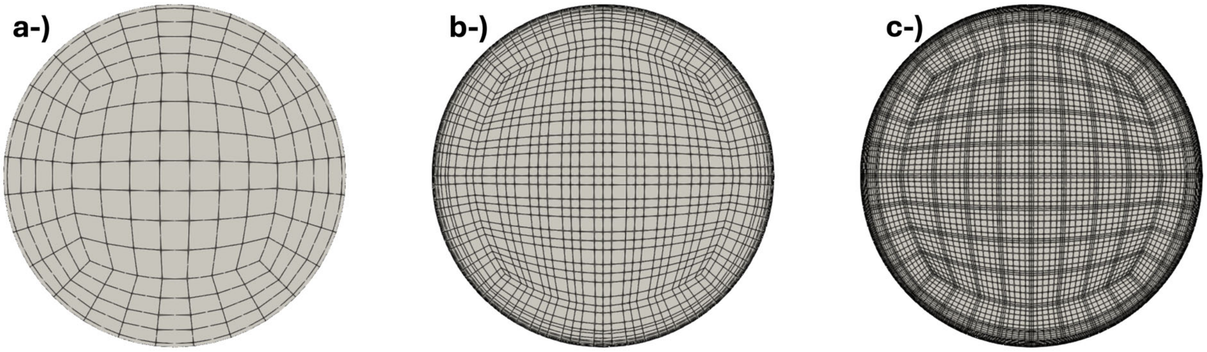

Figure 1. Difference between the mesh and GLL points: (a) mesh elements, (b) GLL points in 3rd polynomial order, and (c) GLL points in 7th polynomial order.

2.3. Reynold's-Averaged Navier Stokes - RANS

The thermal hydraulics of the system can be described using the mean conservation of mass, momentum, and energy equations. These conservation equations are solved in the RANS methodology. However, the Reynolds stress term appears in the derivation of the mean conservation of momentum equation from the Navier-Stokes equation when it is derived via Reynolds decomposition. RANS models rely on the Boussinesq hypothesis (Equation 5), constituting a proportional relationship between the mean strain rate tensor and the Reynolds stress. This term allows for the effects of components with fluctuating velocities (e.g., $\langle u_1'^2 \rangle$,

$\left\langle u_2'^2\right\rangle$, $\left\langle u_3'^2\right\rangle$, $\langle u_1' u_2'\rangle$, $\langle u_1' u_3'\rangle$, and $\langle u_2' u_3'\rangle$) to be taken into account, and for average properties to be calculated without needing to resolve turbulent structures. For the derivation, refer to [3].

$$-\rho\left\langle u_i' u_j'\right\rangle = 2\mu_t S_{ij} - \frac{2}{3}\rho k \delta_{ij} \tag{5}$$

where ρ is the fluid density, μ_t is the dynamic turbulent viscosity (or eddy viscosity), k is the turbulent kinetic energy, δ_{ij} is the Kronecker delta, and S_{ij} is the mean strain rate tensor, which can be calculated per:

$$S_{ij} = \frac{1}{2}\left(\frac{\partial\langle u_i\rangle}{\partial x_j} + \frac{\partial\langle u_j\rangle}{\partial x_i}\right) \tag{6}$$

The mean conservation of mass and momentum under the Boussinesq hypothesis become the RANS equations:

$$\nabla\cdot\langle u_j\rangle = 0 \tag{7}$$

$$\frac{\partial\langle u_i\rangle}{\partial t} + \langle u_j\rangle\cdot\nabla\langle u_i\rangle = -\frac{1}{\rho}\nabla\langle p\rangle + \nabla\cdot\left[(\nu+\nu_t)\left(\nabla\langle u_i\rangle + (\nabla\langle u_j\rangle)^\top\right)\right] + \rho\langle\mathbf{f}_i\rangle \tag{8}$$

Estimation of the kinematic eddy viscosity ($\nu_t = \mu_t/\rho$), which refers to the viscosity of turbulent structures in the system, requires extra modeling. The models used in this study are introduced in the next subsection.

The conservation of energy equation becomes:

$$\frac{\partial\langle T\rangle}{\partial t} + \langle\mathbf{u}\rangle\cdot\nabla\langle T\rangle = \nabla\cdot\left[(\alpha+\alpha_t)\nabla\langle T\rangle\right] \tag{9}$$

where $\langle T\rangle$ is the Reynolds-averaged temperature, $\alpha = \frac{k}{\rho c_p}$ is the thermal diffusivity of the fluid, and α_t is the turbulent thermal diffusivity, modeled as:

$$\alpha_t = \frac{\nu_t}{\mathrm{Pr}_t} \tag{10}$$

The closure problem of Reynolds stress modeling is an active area of research. Numerous models have been developed to find a good generalized approximation. These models are commonly categorized as algebraic, linear, and nonlinear eddy-viscosity models. The turbulence models covered in this section are the Spalart-Allmaras, k-ϵ, k-ω, and Reynold's stress transport turbulence models. All utilize different techniques to estimate the Reynold's stress.

2.3.1. Spalart-Allmaras turbulence model

The Spalart-Allmaras model determines turbulent eddy viscosity by solving a transport equation for the modified diffusivity ($\tilde{\nu}$). It is a one-equation model that requires an algebraic prescription of a length scale [7]. The Spalart-Allmaras model is a low-Reynolds-number model, meaning it is applied without wall functions. Thus, a fine mesh is necessary to resolve the boundary layer.

Turbulent eddy viscosity is calculated as:

$$\mu_t = \rho f_{\nu 1}\tilde{\nu} \tag{11}$$

where $f_{\nu 1}$ is the damping function [8]. The transport equation of the modified diffusivity ($\tilde{\nu}$) is calculated as:

$$\frac{\partial}{\partial t}\rho\tilde{\nu} + \nabla\cdot(\rho\tilde{\nu}\langle\mathbf{u}\rangle) = \frac{1}{\sigma_{\tilde{\nu}}}\nabla\cdot\left[(\mu+\rho\tilde{\nu})\nabla\tilde{\nu}\right] + P_{\tilde{\nu}} + S_{\tilde{\nu}} \tag{12}$$

where $\tilde{\nu}$ is the modified diffusivity, $P_{\tilde{\nu}}$ is the production term, and $S_{\tilde{\nu}}$ is the source term. For the theory behind each term in the transport equation of $\tilde{\nu}$, refer to [7]. Information on the implementation can be obtained from the STARCCM+ user manual [8].

2.3.2. k-ϵ turbulence model

The k-ϵ turbulence model is a two-equation model that solves transport equations for the turbulent kinetic energy (k) and turbulent dissipation rate (ϵ) in order to determine the turbulent eddy viscosity. Here, the original k-epsilon turbulence model by Jones and Launder [9] was applied with wall functions. This high-Reynolds-number approach was later modified to account for the blocking effects of the wall (viscous and buffer layer) by using both a low-Reynolds-number approach and a two-layer approach. The latter approach, first suggested by Rodi [10], divides the computation into two layers. In the layer next to the wall, the turbulent dissipation rate (ϵ) and turbulent viscosity (μ_t) are specified as functions of wall distance. The values of (ϵ) specified in the near-wall layer are smoothly blended with the values computed from solving the transport equation farther from the wall. Additionally, a realizable k-ϵ was developed from the original model. This model includes a variable damping function applied to critical coefficients within the model. This approach allows the turbulence model to satisfy certain mathematical constraints consistent with the physics of turbulence, often referred to as "realizability" [11].

Turbulent eddy viscosity is calculated as:

$$\mu_t = \rho C_\mu f_\mu k T \tag{13}$$

where C_μ is the model coefficient (i.e., changes based on the model, such as the standard k-ϵ, realizable k-ϵ, and standard k-ϵ low Reynolds), f_μ is the damping function, and T is the turbulence time scale. The transport equations for the turbulent kinetic energy and turbulent dissipation rates are:

$$\frac{\partial \rho k}{\partial t} + \nabla \cdot (\rho k \langle \mathbf{u} \rangle) = \nabla \cdot \left(\mu + \frac{\mu_t}{\sigma_k} \nabla k \right) + P_k - \rho(\epsilon - \epsilon_0) + S_k \tag{14}$$

$$\frac{\partial \rho \epsilon}{\partial t} + \nabla \cdot (\rho \epsilon \langle \mathbf{u} \rangle) = \nabla \cdot \left(\mu + \frac{\mu_t}{\sigma_\epsilon} \nabla \epsilon \right) + \frac{1}{T_e} C_{\epsilon 1} P_\epsilon - C_{\epsilon 2} f_2 \rho \left(\frac{\epsilon}{T_e} - \frac{\epsilon_0}{T_0} \right) + S_\epsilon \tag{15}$$

where $\sigma_\epsilon, \sigma_k, C_{\epsilon 1}, C_{\epsilon 2}, C_t$ are model coefficients, P_k and P_ϵ are production terms, f_2 is a damping function, and S_k and S_ϵ are the source terms. More detailed information can be obtained from [8].

2.3.3. k-ω turbulence model

The k-ω turbulence model is another widely used two-equation model. Like the k-ϵ model, it solves for two transport equations: turbulence kinetic energy k and specific dissipation rate ω. The original k-ω equations were proposed by D.C. Wilcox, and information on their origin and justifications can be obtained from [12, 13]. One advantage of the k-ω model is that it performs better in boundary layers under adverse pressure gradients. However, the boundary layer is more sensitive to the free stream values of ω [8]. To overcome this drawback, a k-ω model different from the standard model has been proposed. This new model, named the k-ω SST model, can be derived from the k-ϵ model by applying variable substitution. The transformed equations are similar to those of the k-ϵ model, but an additional term is included to account for cross-diffusion: $\nabla k \cdot \nabla \omega$ [14]. The eddy viscosity is calculated as:

$$\mu_t = \rho k T \tag{16}$$

where T is the turbulence time scale. The transport equations for the turbulent kinetic energy (k) and specific dissipation rate (ω) are:

$$\frac{\partial \rho k}{\partial t} + \nabla \cdot (\rho k \langle \mathbf{u} \rangle) = \nabla \cdot (\mu + \sigma_k \mu_t \nabla k) + P_k - \rho \beta^* f_{\beta^*} (\omega k - \omega_0 k_0) + S_k \tag{17}$$

$$\frac{\partial \rho \omega}{\partial t} + \nabla \cdot (\rho \omega \langle \mathbf{u} \rangle) = \nabla \cdot (\mu + \sigma_\omega \mu_t \nabla \omega) + P_\omega - \rho \beta f_\beta (\omega^2 - \omega_0^2) + S_\omega \tag{18}$$

where σ_ω and σ_k are model coefficients, P_k and P_ω are production terms, f_β^* is the free shear modification factor, f_β is the vortex stretching factor, S_k and S_ω are the source terms, and k_0 and ω_0 are the ambient turbulence values that counteract turbulence decay [15]. More detailed information on this can be obtained from [8].

2.3.4. Reynolds Stress Transport model

Reynolds stress transport (RST) models, also known as second-moment closure models, directly calculate the components of the Reynolds stress tensor by solving their governing transport equations. RST models approximate the stress tensor as:

$$\mathbf{T_{RANS}} = -\rho\mathbf{R} + \frac{2}{3}\mathrm{tr}(\mathbf{R})\mathbf{I} \tag{19}$$

where ρ is the density, **I** is the identity tensor, and **R** is the Reynolds stress tensor.

$$\mathbf{R} = \begin{bmatrix} \overline{u'u'} & \overline{u'v'} & \overline{u'w'} \\ \overline{u'v'} & \overline{v'v'} & \overline{v'w'} \\ \overline{u'w'} & \overline{v'w'} & \overline{w'w'} \end{bmatrix} \tag{20}$$

RST models solve transport equations for each component of **R**. These models can predict complex flows more accurately than eddy viscosity models, because they naturally account for turbulence anisotropy, streamline curvature, swirl rotation, and high strain rates.

The starting point for developing an RST model is the exact differential transport equation for the Reynolds stresses, derived by multiplying the instantaneous Navier-Stokes equations by a fluctuating property and then Reynolds-averaging their product (see [16]).

In the resulting equations, the transient, convective, and molecular diffusion terms do not require modeling [8]. The terms that must be modeled include a turbulent diffusion term, dissipation term, and pressure-strain term. Appropriate modeling of these terms is crucial for RST model accuracy [17]. The transport equation for the Reynolds stress tensor **R** is:

$$\frac{\partial}{\partial t}(\rho\mathbf{R}) + \nabla\cdot(\rho\mathbf{R}\langle\mathbf{u}\rangle) = \nabla\cdot\mathbf{D} + \mathbf{P} + \mathbf{G} - \frac{2}{3}\mathbf{I}\gamma_M + \underline{\boldsymbol{\phi}} - \rho\underline{\boldsymbol{\varepsilon}} + \mathbf{S}_R \tag{21}$$

where **v** is the mean velocity, **D** is the Reynolds stress diffusion, **P** is the turbulent production, and **G** accounts for buoyancy production. The term γ_M corresponds to the dilatation dissipation, $\boldsymbol{\phi}$ is the pressure-strain tensor, $\boldsymbol{\varepsilon}$ is the turbulent dissipation rate tensor, and $\mathbf{S}_R$ is a user-specified source term.

For the linear and quadratic pressure-strain models, dissipation is modeled as:

$$\boldsymbol{\varepsilon} = \frac{2}{3}\varepsilon\mathbf{I} \tag{22}$$

In total, seven equations are solved: six for the symmetric Reynolds stress tensor components and one for the isotropic turbulent dissipation ε.

2.4. STAR-CCM+

The STAR-CCM+ numerical tool was used to perform the RANS simulations. STAR-CCM+, a CFD and multiphysics simulation tool developed by Siemens Digital Industries Software [8], features cell-centered finite volume capabilities. It also offers comprehensive heat transfer capabilities, including conjugate heat transfer, radiative heat exchange, and phase change phenomena such as boiling and condensation. Its scalable parallel computing architecture ensures efficient simulation of large-scale models, making it a powerful tool for analyzing complex thermal-hydraulic systems. This code is NQA-1 qualified and is routinely used to predict thermo-fluid behavior in nuclear reactor core geometries [18]. In the present work, STAR-CCM+ was used to perform RANS-based CFD modeling.

3. AIR-COOLED REACTOR CAVITY COOLING SYSTEM VALIDATION

The following publications have been produced as a result of this year's progress:

Okyay, S., Reger D., Coppo Leite, V., Merzari E., Balestra P., Strydom G. "High-Fidelity Forced Convection Simulations of the University of Wisconsin-Madison Air-Cooled Reactor Cavity Cooling System", Nuclear Engineering and Design (Accepted)

Okyay, S., Reger D., Coppo Leite, V., Merzari E., Balestra P., Strydom G. "Numerical Simulation of a Natural Convection Driven Air-Cooled Reactor Cavity Cooling System Experiment", Nuclear Technology (submitted)

Advanced nuclear reactors play a key role in energy independence by serving as reliable sources of baseload power. In addition to providing dependable baseload power, these reactors incorporate advanced safety features. Effective removal of decay heat from the reactor pressure vessel (RPV) is a key safety aspect in the development of advanced reactor technologies. Several proposed Generation IV concepts, such as HTGRs, sodium-cooled fast reactors (SFRs), and lead-cooled fast reactors (LFRs), include different variations of RPVcooling systems [19]. HTGRs employ a RCCS, which is a passive exo-vessel cooling system that can mitigate accident consequences by using radiative and convective heat transfer. In December 2021, a High Temperature Reactor - Pebble Bed Module (HTR-PM) nuclear power plant (NPP) was integrated into the grid, and it commenced commercial operation on December 6, 2023 [20]. The exceptional passive safety of HTGRs has been demonstrated via the HTR-PM demonstration NPP. Loss-of-cooling tests validated that these reactors can be cooled down by simply relying on natural convection, without needing to depend on the emergency core cooling system during accident conditions [21]. The RCCS includes vertical rectangular ducts called "risers" (or riser ducts) around the RPV. These risers receive heat from the RPV through convection and radiative heat transfer [22]. The heat received by the RCCS is released into the atmosphere (ultimate heat sink) through natural convection of air inside the riser ducts.

In RCCS designs, radiative and convective heat transfer strongly influence each other. This interaction becomes even more pronounced due to the system's reliance on natural convection. Thermal-hydraulic experiments and simulations are essential for characterizing the complex thermal-hydraulic behavior of the RCCS. Vendors must thoroughly understand and characterize these systems in order to demonstrate their effectiveness and optimize them to reduce overall costs. Recent advancements in the thermal-hydraulic characterization of RCCS have been driven by numerous experimental and numerical studies.

Most of the experiments that focused on the air-cooled RCCS were conducted for General Atomics' Modular High-Temperature Gas Reactor (GA-MHTGR) [23–25]. The scale of these experiments is shown in Figure 2. An essential contribution to this field was made by Argonne National Laboratory (ANL) through their Natural Convection Shutdown Heat Removal Test Facility (NSTF), which has been conducted at half the scale of the original design [23, 26–28]. The outcomes based on the NSTF data indicate that the overall heat removal performance remained effective despite various disruptions and challenging conditions, such as blocked riser channels, strong asymmetries from the heated source, and moderate weather shifts. The air-cooled RCCS test facility at the University of Wisconsin-Madison (UW-Madison) represents a quarter-scale model of the original design. The data from this facility are especially important for CFD modeling. Being a smaller domain than NSTF, it is more computationally efficient to run with numerical tools. Asymmetric heating cases tested in this experimental facility, as well as instabilities similar to those observed in NSTF, were reported [25]. Additional experiments were conducted at Texas A&M University by employing a one-eighth-scale model (i.e., half the scale of the UW-Madison facility) of the air-cooled RCCS [29]. For these experiments, only the risers and upper plenum portion were constructed. The results highlight changes in the turbulent characteristics and mixing phenomena in the upper plenum.

Several studies have focused on numerical modeling of the air-cooled RCCS. Among the primary studies are ANL's air-cooled NSTF computational modeling efforts [23, 28, 30, 31]. The ANL report [30] presents

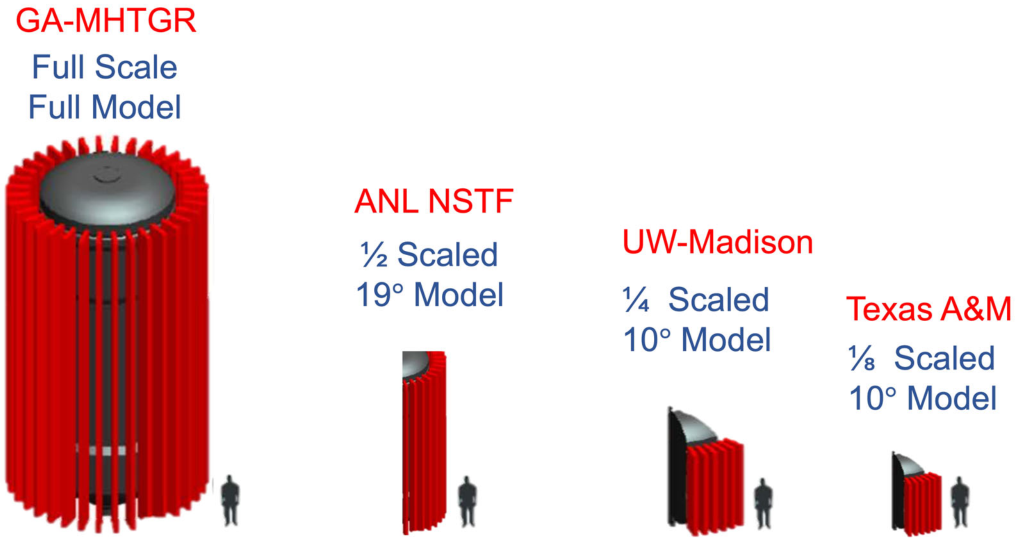

Figure 2. Scaled representations of GA-MHTGR's RCCS.

thermal-hydraulic modeling of NSTF by using the codes RELAP5-3D and STAR-CCM+. The results, obtained via different numerical modeling methods, complement the experimental results. Additionally, the results generated via different turbulence modeling techniques demonstrate sensitivity to turbulence modeling strategies. Moreover, the study by Hu et al. [31] highlights the importance of ambient effects on the air-cooled NSTF system, and proposes a numerical technique to incorporate them. The study by Frisani et al. [32] conveys a CFD analysis performed on an RCCS that featured circular channels instead of rectangular ones. Experimental and simulation results were produced for both the water- and air-cooled versions of the same RCCS, highlighting the differences between each version's heat removal capabilities [32]. The study from Koekemoer et al. [33] investigated coupling the CFD codes with system-level thermal-hydraulic codes in order to improve simulation accuracy. Moreover, that study presents four different coupling approaches and compares their performance with each other. In addition, coarse mesh thermal-hydraulic tools have been employed to enhance the performance of system-level thermal-hydraulic analysis codes, as documented in [34]. The work by Freile et al. [34] considers local heat transfer effects when calculating the Nusselt number, and includes a factor that accounts for the effects of non-uniform temperatures on the RPV. The convective heat transfer is not the dominant heat transfer mode in the reactor cavity; however, it has a significant effect on the surface temperature of the RPV. Therefore, accurate modeling of the natural circulation is crucial for the radiative heat transfer inside the reactor cavity. Porous media or CFD tools can be utilized to develop accurate heat transfer coefficients for the convective heat transfer inside the reactor cavity.

This study presents a comprehensive validation of the modeling of the UW-Madison experimental air-cooled RCCS facility. The modeling efforts began with a forced convection analysis of the RCCS, using both the LES and RANS methodologies. A RANS-based numerical model of the experimental facility was then developed, which included the addition of a heated cavity to the RCCS. The forced convection results were compared with available experimental data for both high- and low-power cases. A sensitivity study was also conducted on the forced convection results.

Subsequently, the RANS numerical model was extended to simulate natural convection cases. The model results were compared with experimental data for both low- and high-power conditions. Heat transfer modes from the heaters to the risers were then analyzed for both forced and natural convection scenarios. Finally, an evaluation of different RANS turbulence models was performed for the natural convection cases.

3.1. UW-Madison Air-cooled RCCS Experimental Facility Design

The experimental facility, which was constructed at UW-Madison, is a one-quarter-scale, 10° representation of the GA-MHTGR RCCS. Information on the methodology used for scaling it down from the original design is given in [23, 25, 35]. The experimental facility consists of two main components: the RCCS and the heated cavity. The RCCS removes heat from the system, while the heated cavity is a thermal enclosure that mimics the reactor cavity in the original GA-MHTGR design. A technical drawing of the experimental facility is shown on the left in Figure 3, and pictures of the main components are given on the right. The orange arrows in Figure 3 indicate the airflow direction inside the RCCS. The inlet plenum serves as the entry point for air drawn from the environment by the heated air in the RCCS. Within the heated cavity, electrical resistance heaters simulate the RPV and emit heat to the six riser ducts. Finally, the outlet plenum serves as a mixing space before the heated air is released back into the environment via a pair of exhaust ducts.

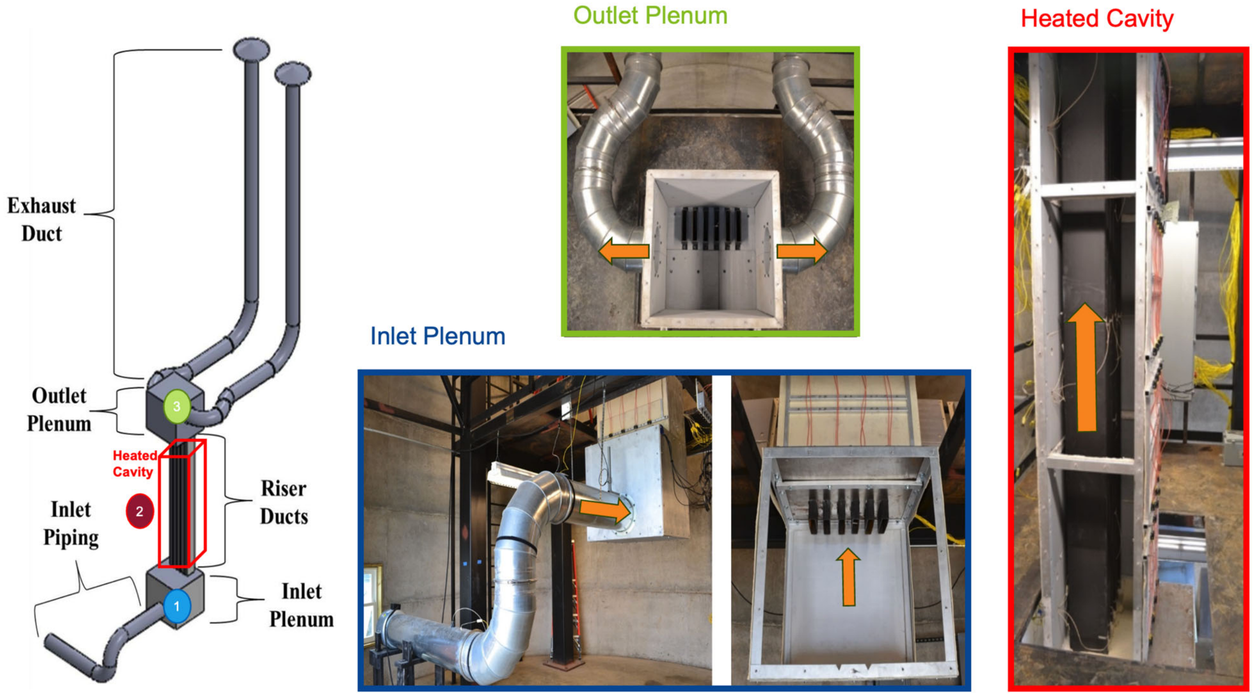

Figure 3. Experimental facility in UW-Madison.

Two types of heat transfer regimes were experimentally tested in this facility: forced and natural convection. Natural convection tests were conducted with both uniform and asymmetric flux in order to investigate the effect of power shape, whereas the forced convection tests were conducted using a uniform flux profile only. Only one of the four tests conducted under the uniform flux scenario (a low-power case) showed unstable behavior (i.e., flow reversal in the exhaust ducts) in the experiments. Flow reversal in an exhaust duct in one of these systems could significantly impact the heat removal characteristics of the RCCS. For example, it could elevate the wall temperature of the riser ducts, which serve as a heat sink to the RPV. Higher temperatures at the riser duct walls will result in less effective heat transfer from the reactor cavity. Natural convection experiments often showed unstable behavior, particularly when low power levels and/or asymmetric heat profiles were applied. Table 1 summarizes the experiments performed in the UW-Madison RCCS facility.

Instrumentation was installed throughout the facility to control the power and measure the temperature and velocity at specified locations. Electrical heaters mounted on the walls of the heated cavity supplied heat to the system. To ensure characterization of the heat removal from the RCCS, temperature measurements

Table 1. Summary of experiments performed in the UW-Madison RCCS facility.

Type	Case	Number of Experiments	Instability
Forced Convection	Forced Flow	4 (2 Power Levels, 2 Repeat)	No (All experiments)
Natural Convection	Uniform Flux	4 (2 Power Levels, 2 Repeat)	Yes (1 of 4 experiments)
	Asymmetric Flux	4 (2 Power Levels, 2 Repeat)	Yes (All experiments)

were taken at various different points. Velocity measurements were obtained from the system entrance, due to temperature restrictions on the velocity sensors. A velocity transducer (TSI 8455) was used to measure the velocity at the inlet pipe [25]. A schematic of the locations of the instrumentation is given in Figure 4.

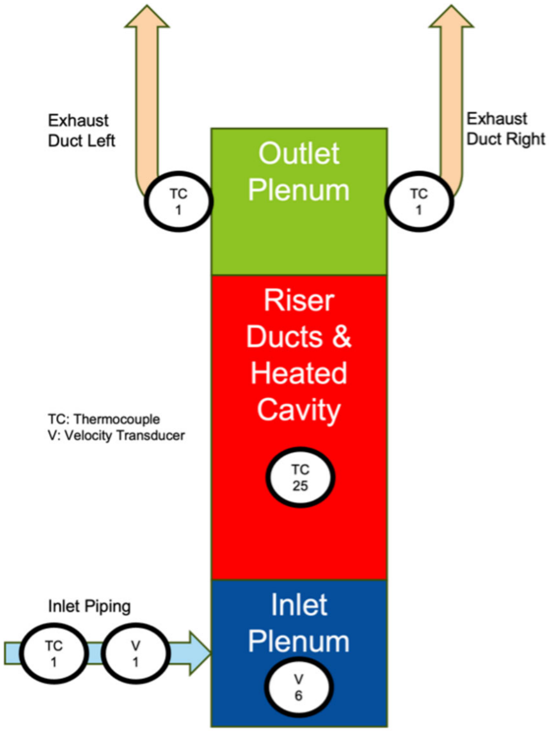

Figure 4. Experimental facility instrumentation. (The numbers represent the number of measurement devices located in that given section.)

3.1.1. Heated cavity

The heated cavity is a critical component of the experimental facility, as this is where the majority of the heat transfer occurs. Heat is transferred from the electrical heaters (RPV) to the riser ducts via both radiative and convective mechanisms. Conduction occurs between the heaters and the frame of the heated cavity, as the heaters are mounted within the cavity frame. A simplified representation of the heat transfer diagram is provided on the right in Figure 5.

Temperature measurements were primarily centered on the heated cavity, including the riser ducts where the majority of the heat transfer occurs. Both the wall and air temperatures were measured to provide detailed information on the heat transfer characteristics. One of the risers (the 4th riser) was more heavily instrumented than the others. For this riser, wall temperatures for each side are provided. Figure 6 summarizes the temperature measurement instrumentation inside the heated cavity.

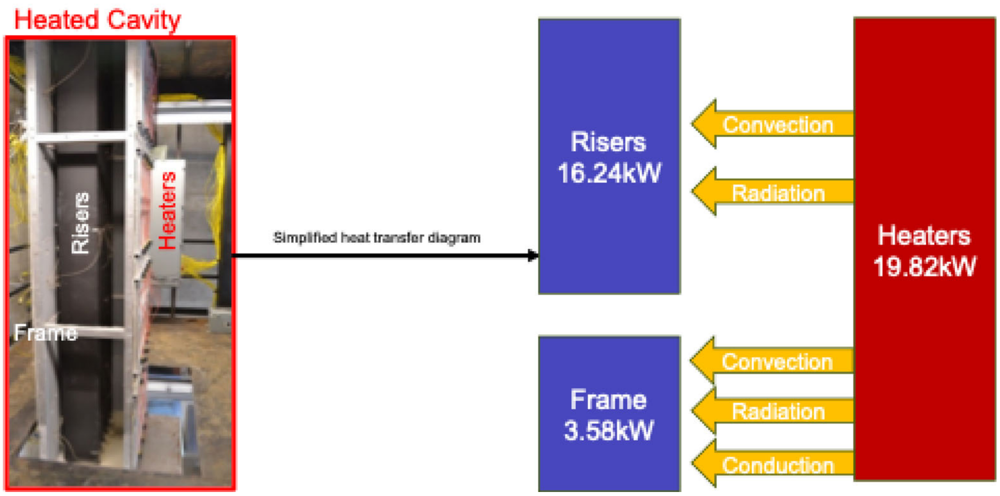

Figure 5. Heat diagram for the heated cavity.

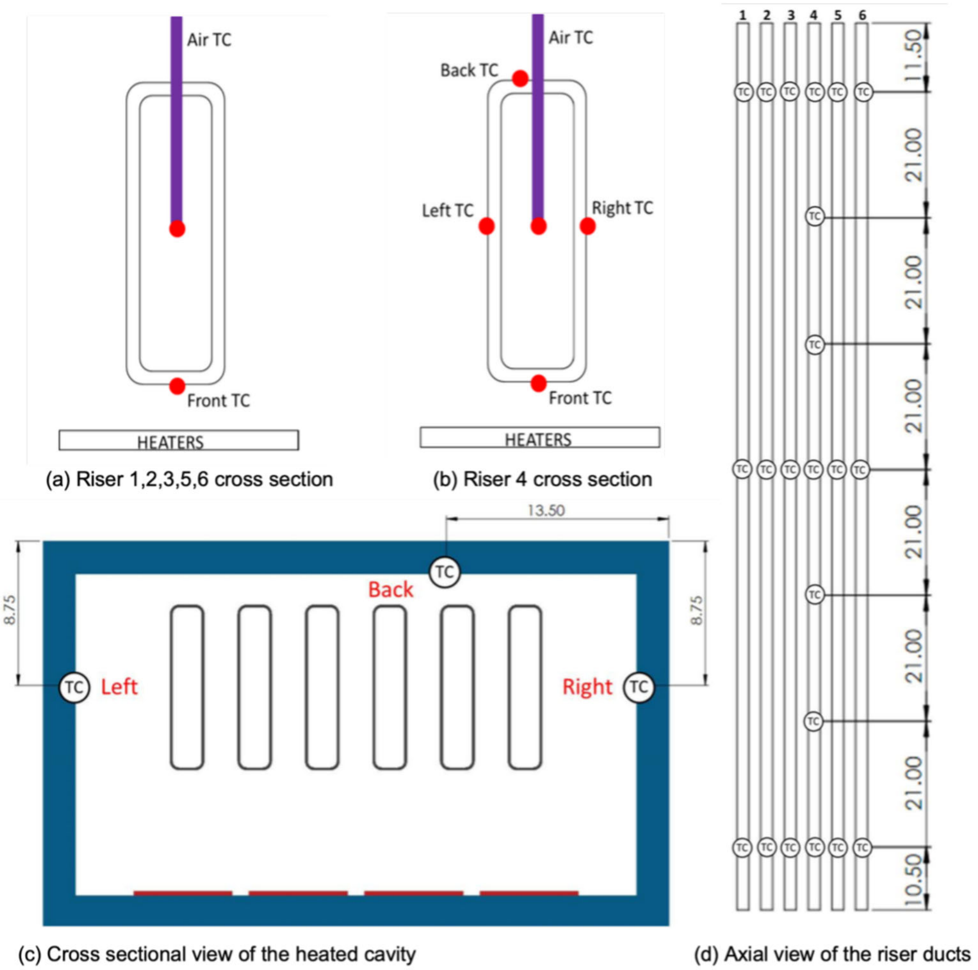

(a) Riser 1,2,3,5,6 cross section

(b) Riser 4 cross section

(c) Cross sectional view of the heated cavity

(d) Axial view of the riser ducts

Figure 6. Heated cavity instrumentation.

3.2. Forced Convection Modeling

3.2.1. High-Fidelity RCCS modeling with LES and RANS

The high-fidelity section will focus on the RCCS, which consists of the inlet plenum, riser ducts, outlet plenum, and exhaust duct entrances. The heated cavity is not modeled in this case. The focus of the high-fidelity modeling was to compare the LES and RANS methods in terms of the forced convection scenario in the RCCS. The geometry is presented in Figure 7. Since the focus is on forced convection, only a portion of the exhaust ducts and inlet piping was modeled.

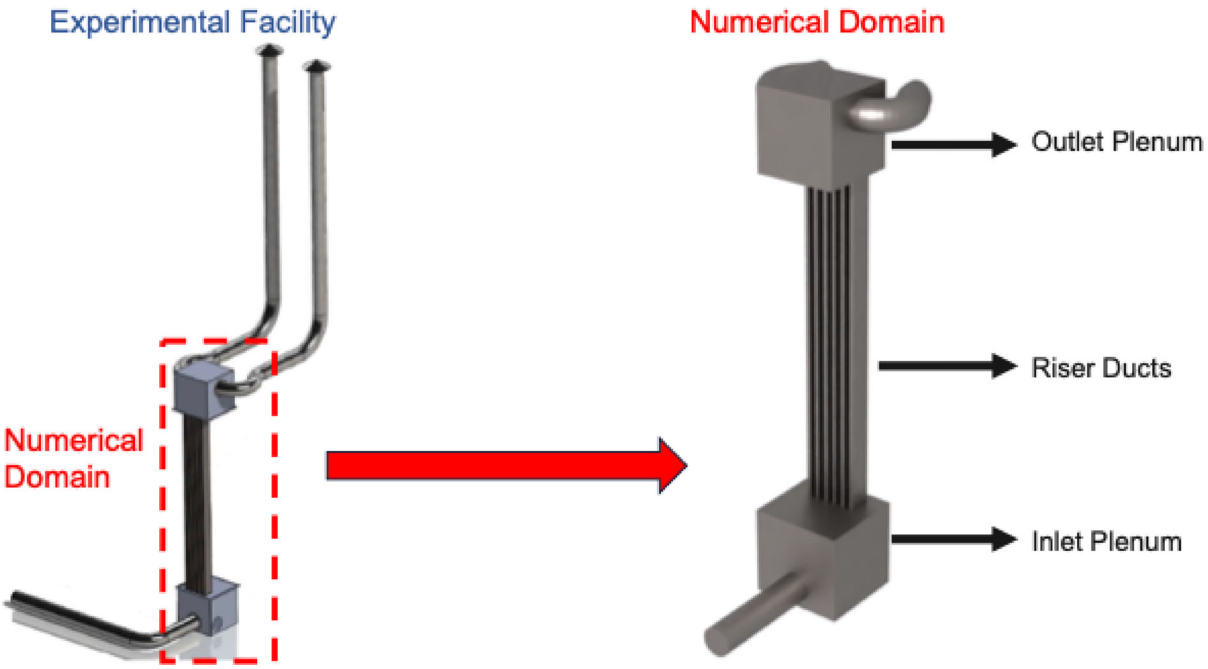

Figure 7. Numerical domain for high-fidelity simulations.

NekRS (version 23.0) was employed for the high-fidelity LES RCCS simulations. The geometry and mesh were prepared using the CUBIT (version 16.14) software [36]. As NekRS requires fully hexahedral mesh, a blocked (or mapped) meshing strategy was employed. Since it was a wall-resolved simulation, the finer elements were preferred near wall in order to resolve the boundary layer. The mesh contained approximately 5.5 million elements. NekRS uses GLL points in each spectral element, and the mesh was equivalent to 1.19 billion grid points, with the 5th polynomial order representation compared to a finite element code.

The boundary conditions of the model are presented in Figure 8. A velocity inlet with recycling provided fully developed turbulent flow to the system. Pressure outlet boundary conditions were used in the exhaust ducts. To prevent backflow, Dong outflow treatment was employed [37]. All the walls had no-slip boundary conditions. The temperature and velocity boundary conditions for the inlet were taken from the experimental report. The temperature at the inlet was 297 K and the velocity was 4.359 m/s. The walls of the inlet and outlet plenum were assumed to be adiabatic.

The temperatures at the riser duct walls were imposed as Dirichlet boundary conditions derived from experiments [25], as shown in Figure 9. Only one data fitting was applied to the side walls (left and right walls) since the temperature profiles were similar. All the riser ducts have the same thermal boundary condition in the high-fidelity model, which is an adequate assumption given the purpose of the model. The high-fidelity model aims to compare the turbulence modeling strategies between the LES and RANS methodologies.

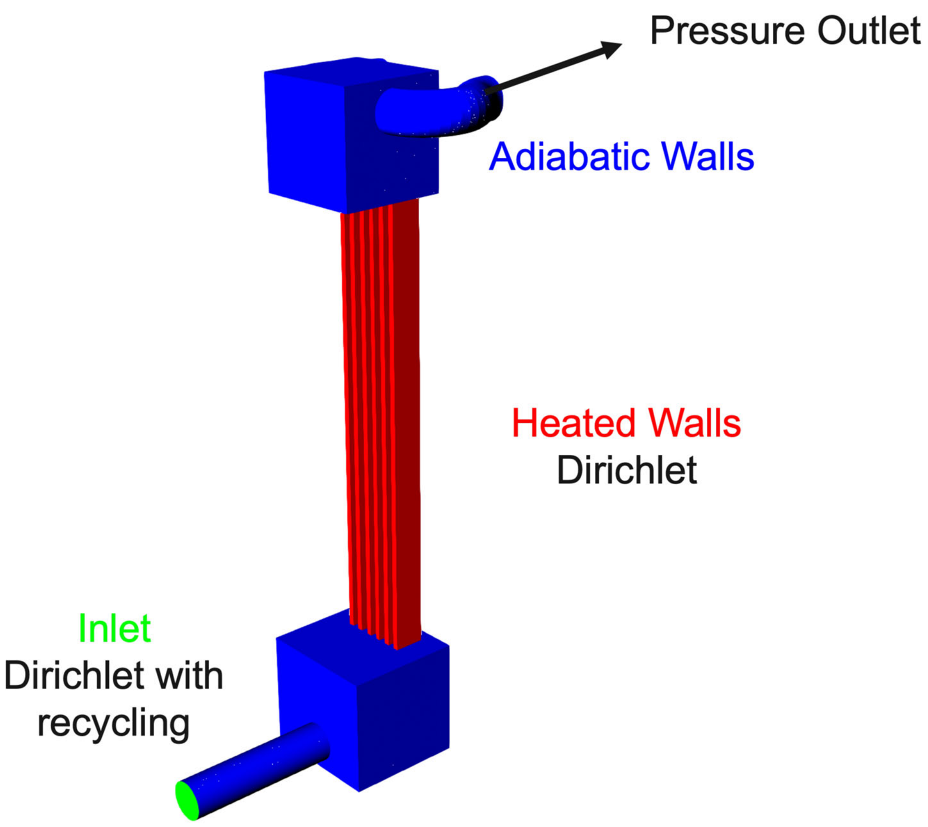

Figure 8. NekRS LES boundary conditions.

The temperature values for the validation model will be obtained from the heated cavity simulations for the validation of the experimental facility.

The RCCS setup for both the RANS and LES methodologies is summarized in Table 2. The boundary conditions of this model are shared in Figure 8. The velocity at the inlet is 4.359 m/s and the temperature is 297 K. Since only the RCCS portion of the experimental facility is modeled, the power is 15.76 kW.

Table 2. Setup parameters for the LES and RANS configurations.

Parameter	**LES**	**RANS**
Methodology	Spectral Element Method (SEM)	Finite Volume Method (FVM)
# of Elements	5.5 Million (1.19 B grid points)	50 Million
Turbulence Modeling	Explicit Filtering	$k-\epsilon$ (R), $k-\omega$ SST, Reynolds Stress
Radiation Modeling	Not Modeled	
Wall Modeling	Resolved ($y^+ < 1$)	All y+ treatment ($30 < y^+ < 200$)
Outflow Treatment	Dong Outflow	—
Fluid Properties	Air (constant)	
	Density	1.184 $\mathrm{kg/m^3}$
	Viscosity	1.855E-05 $\mathrm{kg/(m \cdot s)}$
	Thermal Conductivity	0.026 $\mathrm{W/(m \cdot K)}$
	Specific Heat Capacity	1005 $\mathrm{J/(kg \cdot K)}$

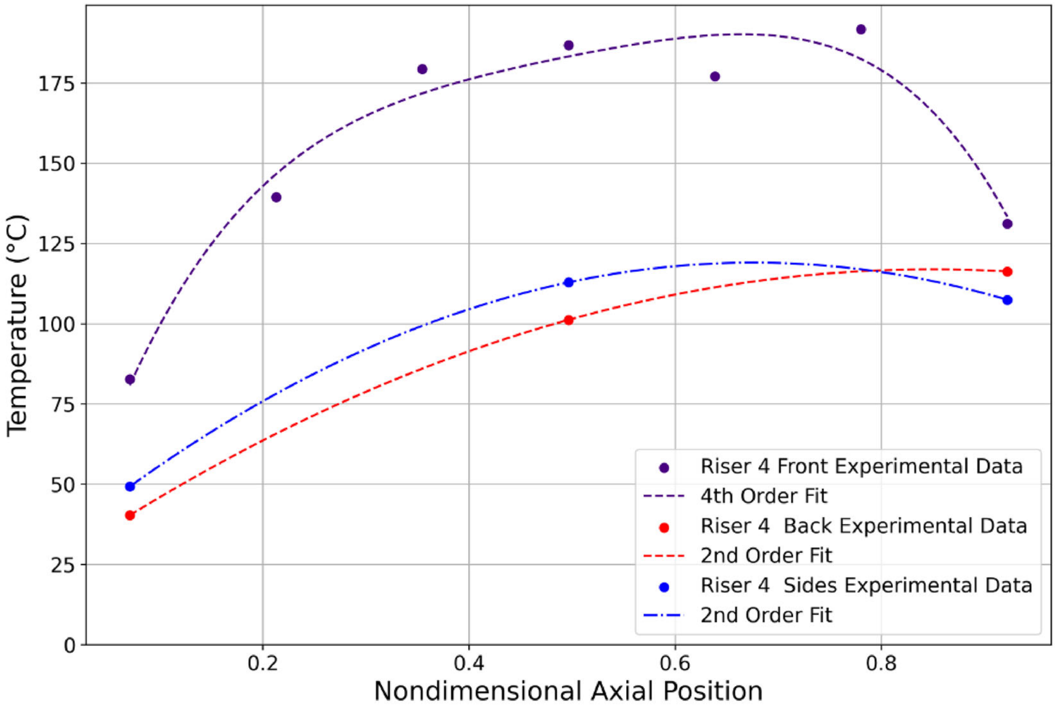

Figure 9. Temperature boundary conditions for the riser ducts walls in LES.

The Richardson number ($Ri = Gr/Re^2$) refers to the ratio of buoyancy-driven convection to forced convection. It is calculated to be less than 0.1; therefore, buoyancy is neglected in the RCCS. An adaptive time step was used, with an average time step of 1.5e-5 seconds. For time stepping in NekRS, we used BDF2 and subcycling. More information on the implementation can be obtained from Min et al. [38]. The instantaneous velocity and temperature can be seen in Figure 10. The airflow coming from the inlet pipe is redistributed in the inlet plenum to six riser ducts, based on their flow areas. Due to contraction of the flow, the velocities increase when the flow enters the riser ducts. In the riser ducts, the flow begins to heat up from the walls. It then enters the outlet plenum and starts to mix, causing the temperature of the air in the outlet plenum to decrease. Eventually, the flow exits the system through the exhaust ducts to the atmosphere.

The instantaneous velocity contour of the outlet plenum is shown in Figure 11. The results reveal turbulent jet interactions in the outlet plenum. These flow patterns can significantly impact the thermal-hydraulic performance of the RCCS. Leite et al. [39] observed that turbulent jet interactions can also impact the system and change the flow characteristics.

Multiple RANS simulations with different turbulence modeling strategies were performed. The selected models from STAR-CCM+ were (1) realizable $k - \epsilon$ with Wolfstein derivation [40], (2) $k - \omega$ SST [14], and (3) the RSM with elliptic blending [41]. In all the models, the same near-wall resolution was applied to ensure the same y^+, resulting in the same wall treatment. The all y^+ treatment was used in STAR-CCM+, with the average y^+ being between 30 and 200. Steady-state equations were solved with the segregated flow algorithm in STAR-CCM+.

A mesh convergence study was performed. The outlet bulk temperature and 4_{th} riser outlet bulk temperature were calculated using various mesh resolutions. The STAR-CCM+ results, shown in Table 3,

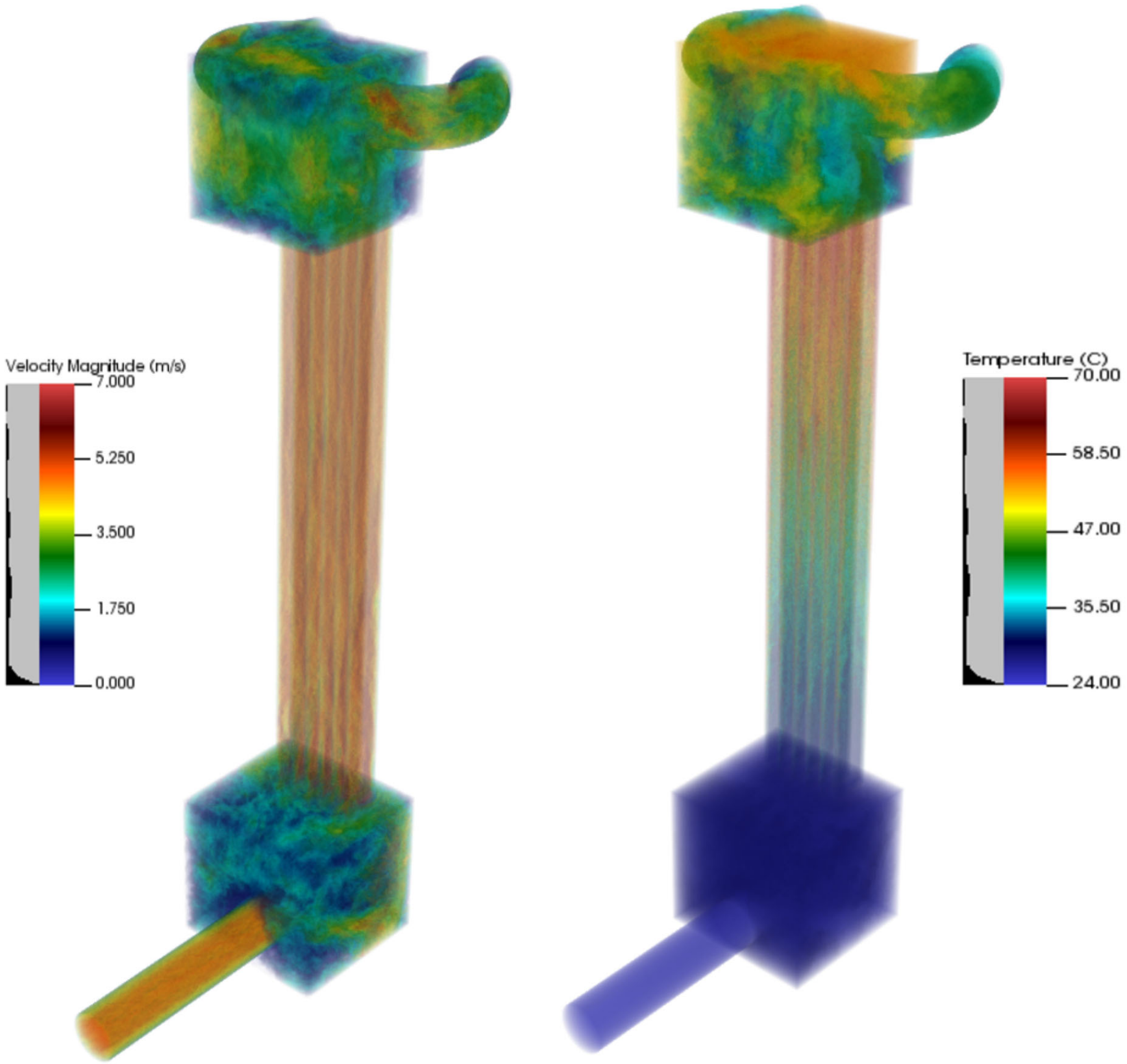

Figure 10. (Left) NekRS LES instantaneous velocity (m/s). (Right) Instantaneous temperature (K).

are mesh converged after 50 million elements.

Table 3. STAR-CCM+ mesh convergence results.

Mesh Size (Million Cells)	**Bulk Temperatures (°C)**	
	T_{out} **(°C)**	T_4 **(°C)**
0.197	64.01	67.16
13.9	65.64	68.26
61.4	66.15	69.03
104.6	66.51	68.94

Mesh convergence in NekRS was achieved by leveraging SEM. The same parameters were calculated, and the results are presented in Table 4. The polynomial order of the solution in the simulation was increased to ensure grid convergence. As the results show a less than 1% change between the 5th and 7th polynomial

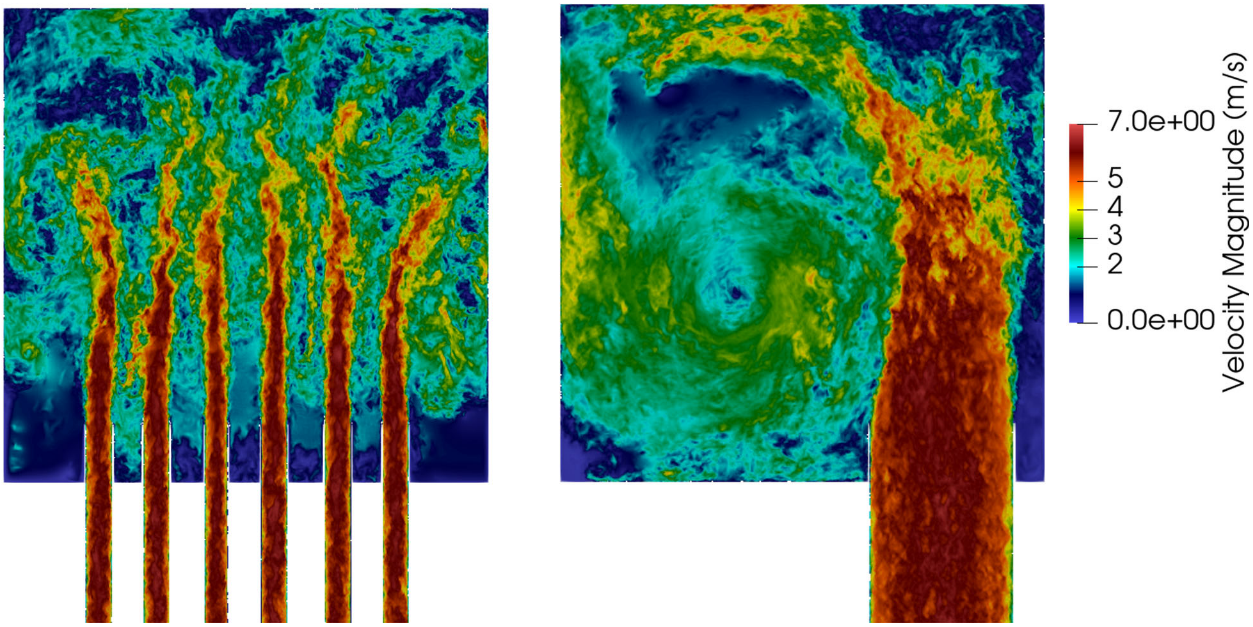

Figure 11. NekRS LES instantaneous velocity (m/s) contour in the outlet plenum. (Left) Side view. (Right) Front view.

orders, grid convergence is assumed to be achieved at the 5th polynomial order.

Table 4. NekRS mesh convergence results.

Polynomial Order	**Number of Grid Points**	**Bulk Temperatures** (°C)	
		T_{out} **(°C)**	T_4 (°C)
3	355 Million	61.73	66.13
5	1198 Million	60.01	67.46
7	2842 Million	60.30	67.67

The LES and RANS results are compared in Figure 12. The LES results were time-averaged at approximately six flow-throughs to obtain results for the riser ducts. The time-averaged temperature profiles in the center of the 4th riser duct for the LES and RANS simulations were compared. The RSM with elliptic blending matches well with the LES results, as was expected. As one of the more advanced turbulence models, the RSM incorporates seven transport equations for the Reynolds stresses, enabling it to represent anisotropic turbulence and swirling flows [42]. However, the RSM entails significant computational time as compared to the realizable $k-\epsilon$ and $k-\omega$ SST models. The two-equation models add two extra coupled partial differential equations to the RANS equations in order to include the effect of turbulent fluctuations on the average flow field. Therefore, compared to RSMs, they are more computationally efficient. The $k-\omega$ SST model more closely aligns with the LES results than does the realizable $k-\epsilon$ model. The two-equation models start showing differences after the mid-height of the riser duct, and the differences become significant when it is closer to the outlet plenum. The riser duct flow closer to the outlet plenum is more likely to be affected by jet interactions, as can be seen in Figure 14. This effect causes greater deviation for the realizable $k-\epsilon$ than for the $k-\omega$ SST model. Considering its computational cost and accuracy, the $k-\omega$ SST model will be used to perform simulations of the experimental facility at UW-Madison.

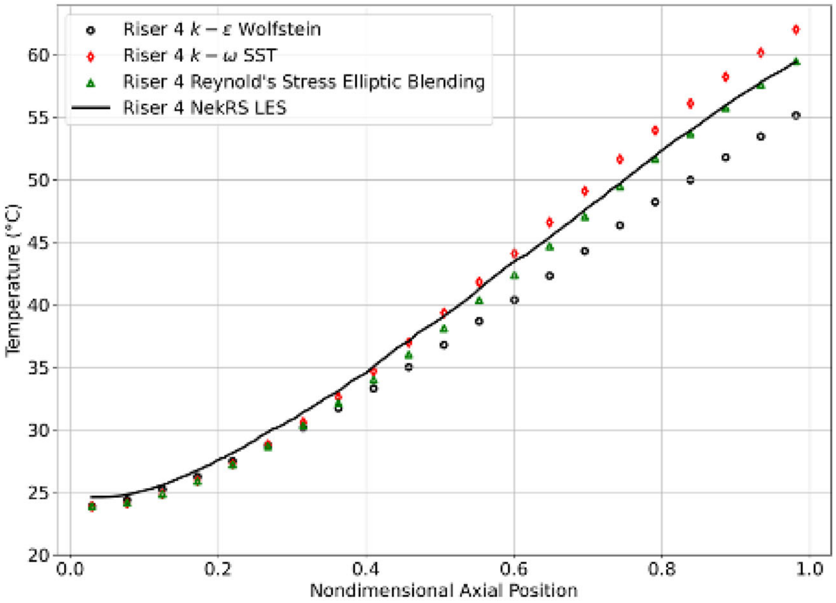

Figure 12. Forced convection comparison of LES and RANS temperatures at the center of the 4th riser duct in RCCS.

3.2.2. UW-Madison Experimental Facility (RCCS and Heated Cavity) RANS Modeling

Numerical modeling of the experimental facility is more complex than the RCCS modeling covered in the previous section. The heated cavity should be included in the numerical modeling in order to obtain a complete description of the system. The numerical model of the experimental facility is shown in Figure 13. The left-hand side shows the RCCS part of the experimental facility; the right-hand side shows the numerical model, which includes the RCCS and heated cavity from the experimental facility.

Similar boundary conditions were used for the RCCS; however, the boundary conditions of the riser ducts were changed from Dirichlet to interface boundary conditions. The boundary conditions on the axial cut of the domain are presented in Figure 14. The heaters were modeled as a volumetric heat source. Natural circulation of the air inside the heated cavity was modeled, since it significantly contributes to the heat transfer from the heaters to the riser ducts. The heat conduction equations were solved in the cavity frame, heaters, and solid walls of the riser ducts. The thermal conductivity values were taken from the experimental report [25]. The interface between the solid and the fluid domains was modeled as conjugate heat transfer. Convective cooling was applied to the outer walls of the cavity frame, under the assumption that the heat transfer coefficient was equal to 6 W/m^2K and that the ambient temperature was 297 K.

This subsection focuses on the simulation results for the experimental facility in UW-Madison. The experimental facility includes the RCCS and heated cavity, both of which were modeled using the RANS methodology in tandem with STAR-CCM+. The main parameters are presented in Table 5.

Forced convection high-power scenario (37.97 kW)

The experimental test number for this case is 18, and the experimental results are presented in [25]. Table 6 shows the energy balance comparison between the experimental and numerical results. The energy balance is reported as the power removed through the RCCS and the total power losses (mainly via the heated cavity)

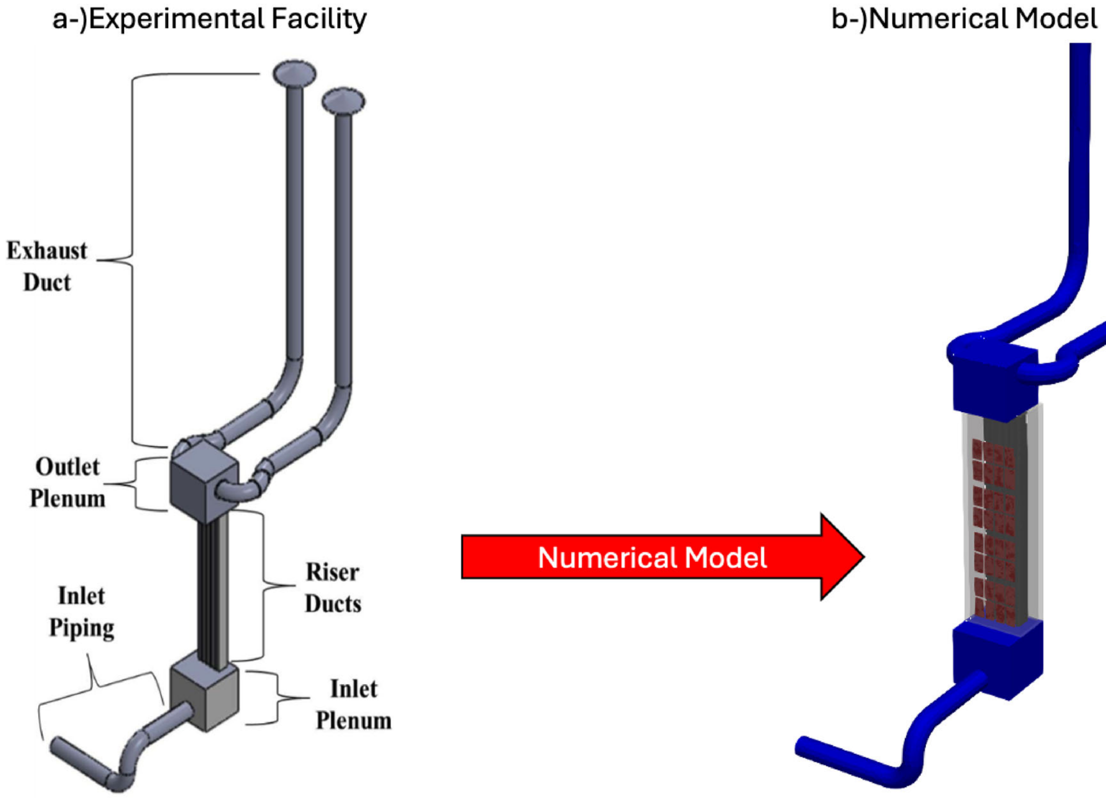

Figure 13. Numerical model of the UW-Madison experimental facility.

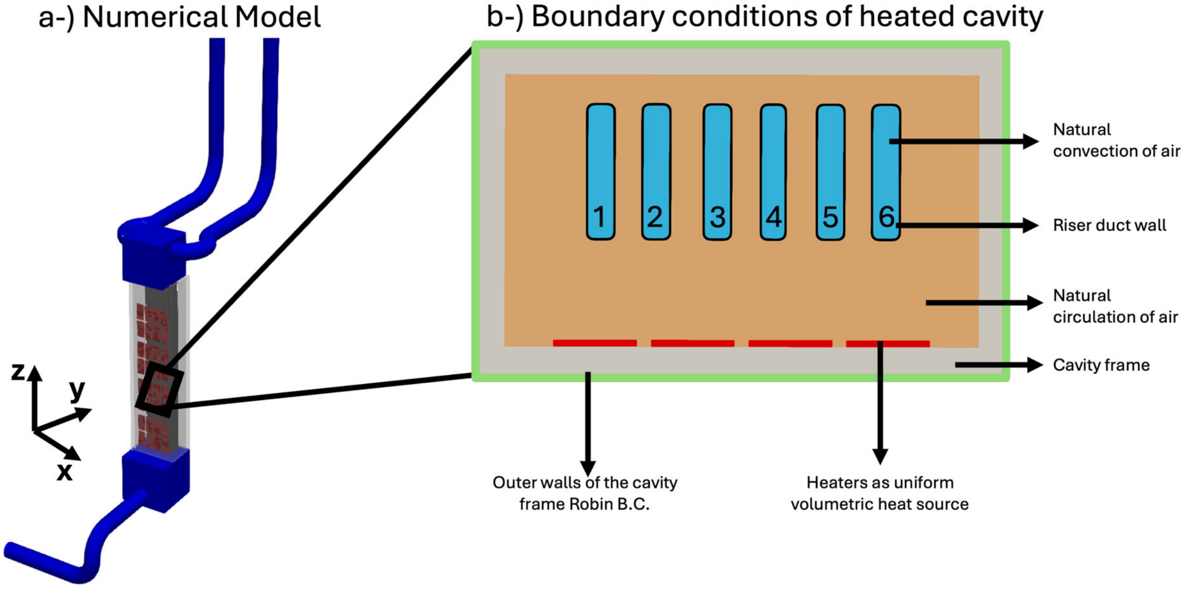

Figure 14. Boundary conditions for the numerical model of the UW-Madison experimental facility.

in the system. The simulation results overestimate the total heat removed by the RCCS. The main difference

Table 5. Setup parameters for the numerical model of UW-Madison's air-cooled RCCS.

Parameter		
Modeling Strategy	RANS	
Solver	Segregated-Steady	
Methodology	Finite Volume Method (FVM)	
Number of Elements	125.3 Million	
Turbulence Modeling	$k-\omega$ SST	
Radiation Modeling	Net Radiation Method (only in the heated cavity	
Buoyancy Modeling	Low Mach Approximation (only in the heated cavity)	
Wall Modeling	All y+ treatment	
Experimental Test Number	14	18
Power Levels	Low Power	High Power
Power	19.82 kW	37.97 kW
Inlet Velocity	4.245 m/s	4.274 m/s
Inlet Temperature	297 K	296.94 K
Fluid Properties	Air	
	Density	Ideal Gas Law
	Viscosity	Sutherland's Law
	Thermal Conductivity	Sutherland's Law
	Specific Heat Capacity	Constant
	Pr_t	0.85

could be caused by the method of calculating the power; the instantaneous values are used to calculate the power removed by the RCCS. The difference between the experiment and simulation is less when it comes to the power losses. The power losses are calculated through the solid insulation material, which is less sensitive to changes caused by fluid velocity.

Table 6. High-power-case energy balance comparison.

Name	STAR-CCM+	Experiment	Error (%)
Power Removed by RCCS	31.55 kW	29.34 kW	+7.09%
Power Losses	6.36 kW	6.39 kW	-0.47%
Total	37.91 kW	35.73 kW	+6.10%

The comparison of results focuses on the 4_{th} riser duct, since that is the riser duct that is heavily instrumented. Figure 15 shows the wall temperatures for the 4_{th} riser duct when comparing the experiment and the simulation. The filled markers represent the experimental data points, and the empty ones indicate the STAR-CCM+ results. The colors (black, blue, red, and purple) represent the riser's side walls, which are also marked with a cross on the left side of the figure, showing the 4_{th} riser duct. The temperatures along the wall are compared between the experiment and the simulation. The STAR-CCM+ results successfully capture the same trends reflected in the experimental measurements. The front wall (purple) temperature is more than 100°C higher than the other wall temperatures. Since this is the side of the riser duct that directly faces the heaters, it is expected to show higher temperatures than the other sides. Some differences are observed regarding the front wall when comparing the experiment and the simulation. These differences can be attributed to several parameters, such as the emissivity and thermal conductivity of the riser duct walls. Some of these values had to be estimated based on the literature, since they went unreported in the experiments. The emissivity values were estimated at 0.8. As the heat was mainly transferred by radiation from the heaters to the riser ducts walls, the estimated parameters (e.g., emissivity) may be the source of this difference. The error bars were added for the wall temperatures to show the 10% range for the experimental values.

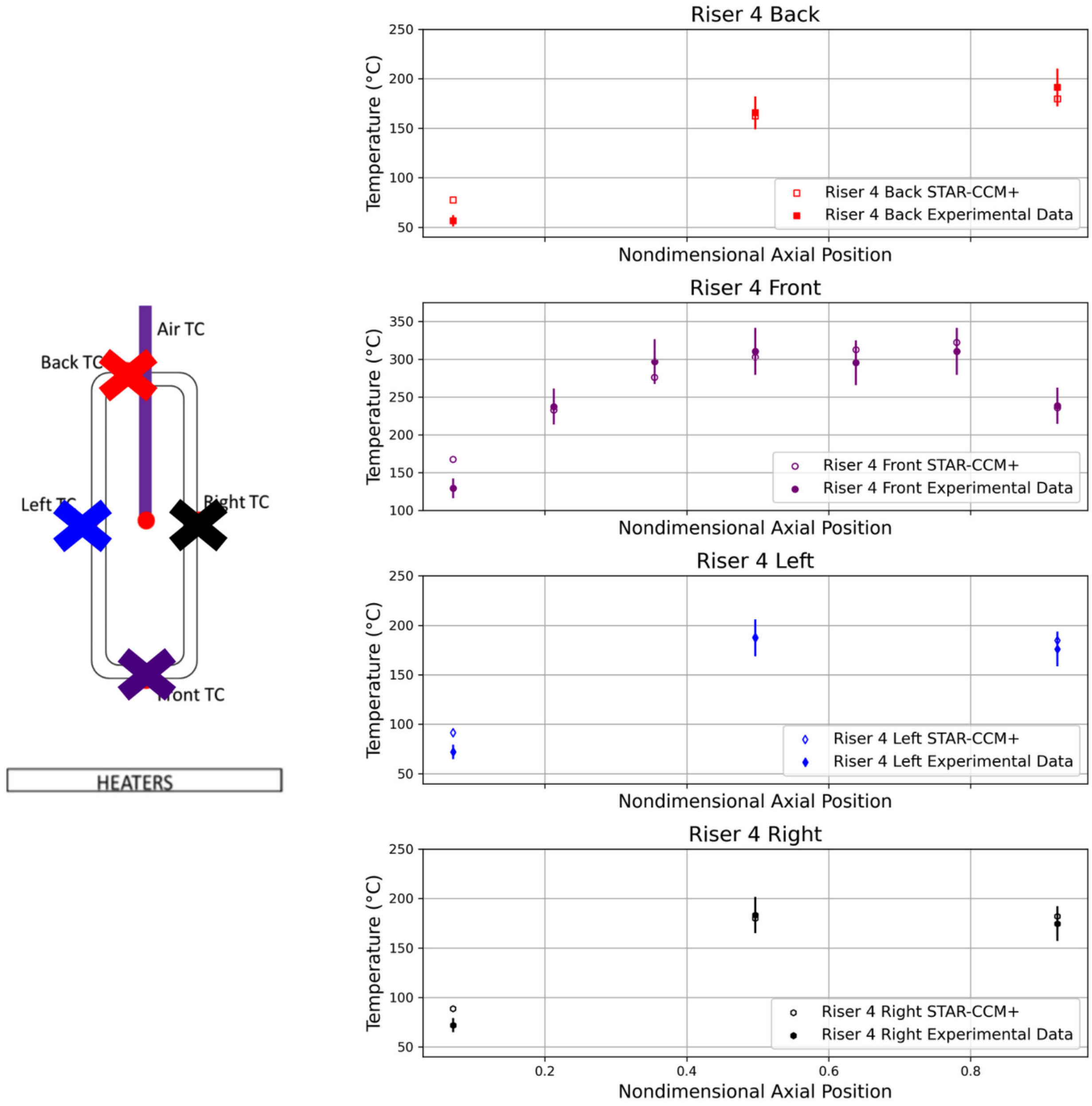

Figure 15. Forced convection high-power-case temperature comparison between RANS and the experiment in regard to the walls of the 4_{th} riser duct.

Figure 16 compares the temperatures of the air at the center of the 4_{th} riser ducts. The filled squares represent the experimental data, the empty ones represent the STAR-CCM+ results, the darker area represents the 5% error band (around 4°C), and the lighter area represents the 10% error band (approximately 8°C). The center temperature matches the experimental results at roughly 5% uncertainty. The STAR-CCM+ results underestimate the experimental results at the center of the channel. Since the wall temperatures match, this difference could be caused by the temperature profile predicted by the RANS model. The simple gradient diffusion hypothesis is used for the turbulent heat flux modeling and may be the reason for the underestimation at the center location.

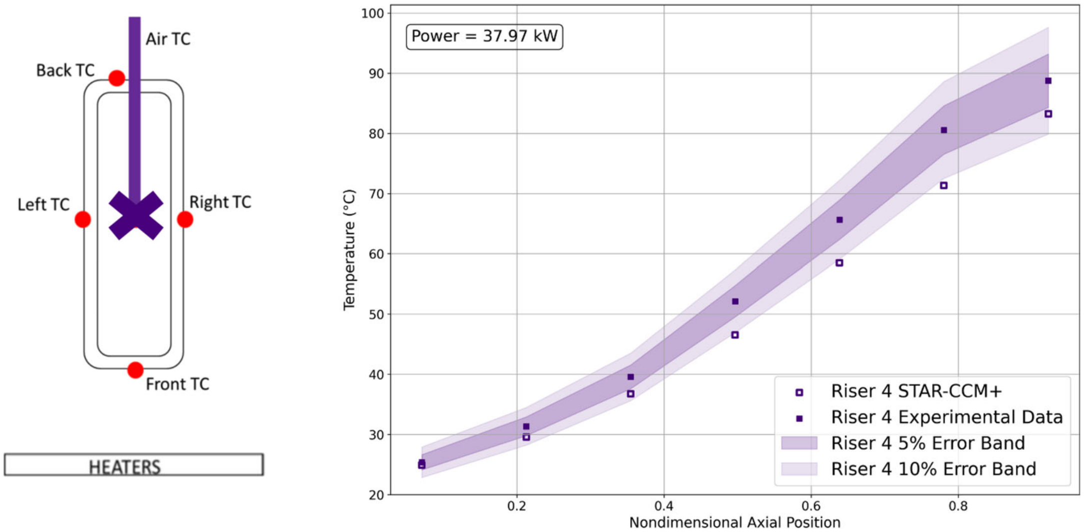

Figure 16. Forced convection high-power-case comparison of the RANS and experiment temperatures at the center of the 4_{th} riser duct.

Figure 17 compares the air temperatures measured at the center of all the riser ducts. Each color represents a different riser duct from the experiment. From left to right within the same color, the axial location of the thermocouple increases. The first bar shows the temperature for the bottom thermocouple, which is closer to the inlet plenum, while the last bar shows the temperature deviation for the top thermocouple. The exact location of the thermocouples can be obtained from Figure 6. The 4th riser duct (purple in the figure) has more thermocouples than the other riser ducts. In general, the temperature deviation is approximately 6°C, which is sufficient for the RANS modeling. More deviation is observed with increasing axial position.

The wall temperatures for the heated cavity were compared to those of the experiment. The results, presented in Table 7, show an adequate match between the two. Here, an additional source of uncertainty can arise from the thermal conductivity and thickness of the insulation material in the cavity frame.

Forced convection low-power scenario (19.82 kW)

The same model was used to simulate the low-power conditions. The experimental test number for this case is 14 [25]. The energy balance comparison between the experiment and simulation is presented in Table 8. The energy balance differs by less than 5% when comparing the experiment against the simulations.

Table 8. Forced convection low-power-case energy balance comparison.

Name	STAR-CCM+	Experiment	Error (%)
Power Removed by RCCS	16.04 kW	15.76 kW	+1.75%
Power Losses	3.74 kW	3.53kW	+5.61%
Total	19.78 kW	19.29 kW	+2.50%

The results of comparing the wall temperatures for the 4_{th} riser duct successfully capture the trends shown in the experiment. However, some deviation begins at around the middle of the system, where the temperature values start to show differences exceeding 15°C. The difference between the simulation and

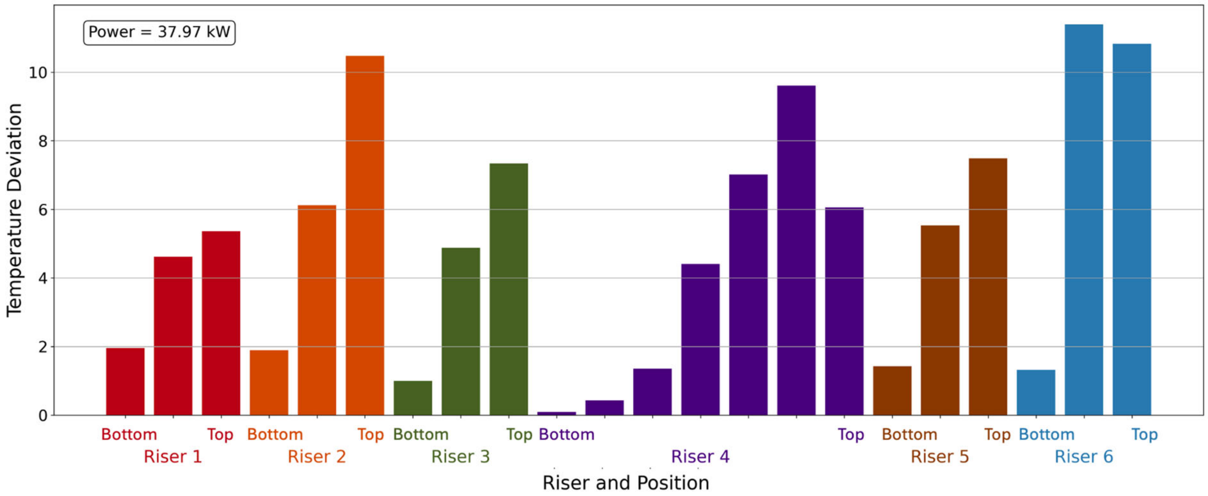

Figure 17. Forced convection high-power-case riser air temperature difference between RANS and the experiment.

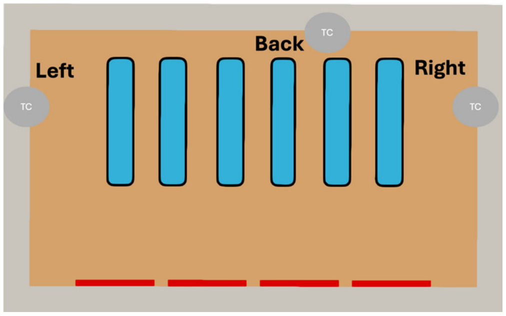

Table 7. Test 18 Heated Cavity Wall Temperature Comparison

Name	STAR-CCM+ (°C)	Experiment (°C)
Left	308.42	291.52
Back	215.43	243.04
Right	302.63	283.50

Figure 18. Forced convection high-power comparison of heated cavity wall temperatures.

experiment is generally less than 15°C. There are multiple possible reasons for this mismatch. For example, since the heat is mainly transferred via radiative heat transfer, parameters such as emissivity could be the reason behind this deviation.

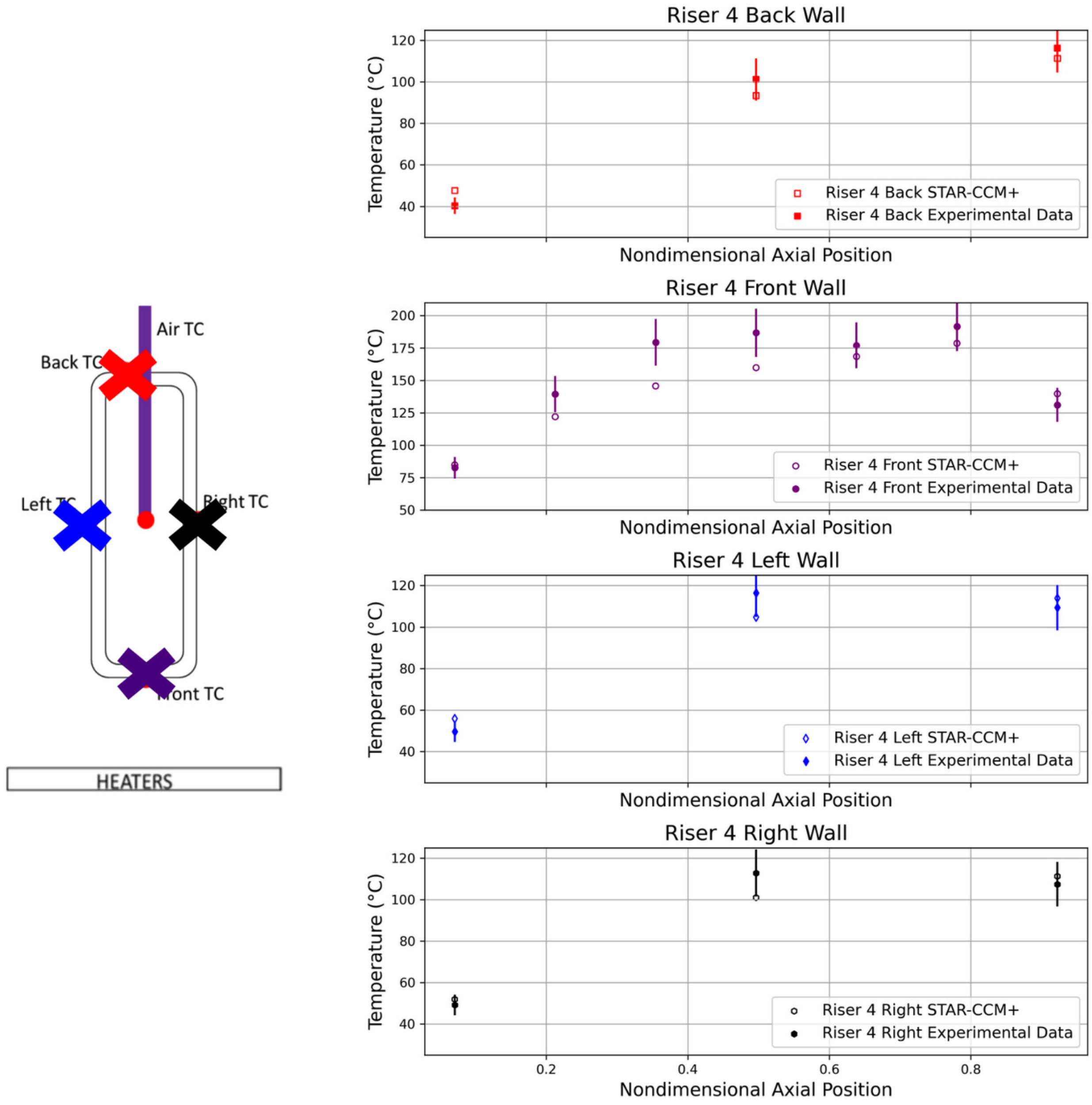

Figure 19. Forced convection low-power comparison between RANS and the experiment in regard to the wall temperatures for the 4_{th} riser duct.

Figure 20 compares the air temperatures at the center of the riser duct. The results from STAR-CCM+ match those of the experiment, within a 10% range (roughly 6°C). However, the temperature values from STAR-CCM+ underestimate the temperature profile in the center of the channel. This difference is caused by the wall temperature profile, which shows lower temperatures than are reflected in the experiment. The temperature distribution in the riser duct is mainly dictated by the temperature distribution of the walls.

Figure 21 reports the air temperature difference between the experimental and simulation results for all the riser ducts. The plot shows the difference in centerline air temperature for each riser duct. The temperature deviation increases with the axial position when more heat is removed by the air. A possible reason for the difference could be the parameters used in the RANS modeling strategy, such as the turbulent heat flux

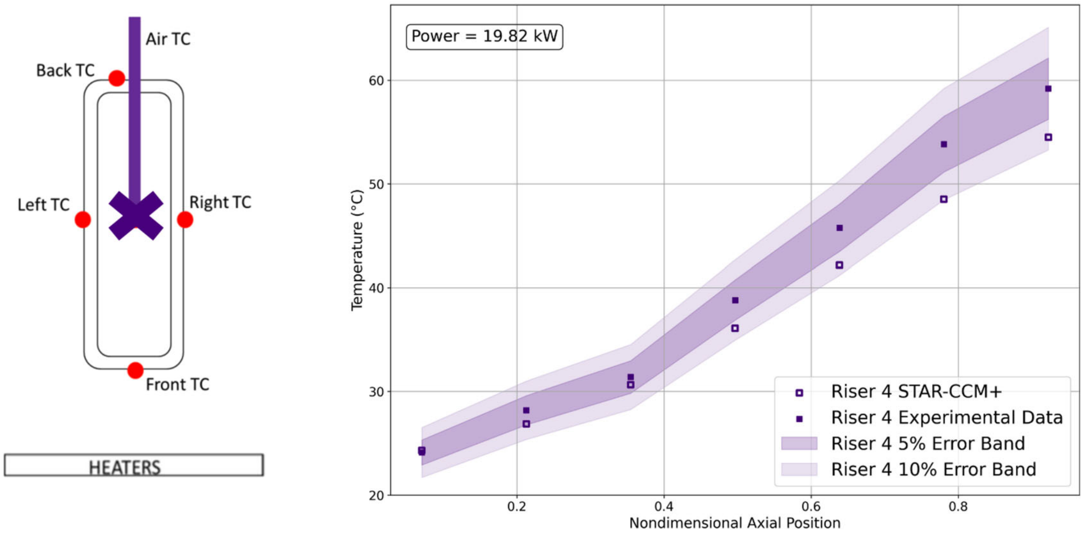

Figure 20. Forced convection low-power comparison between RANS and the experiment in regard to the temperature at the center of the 4_{th} riser duct.

modeling approach and the turbulent Prandtl number.

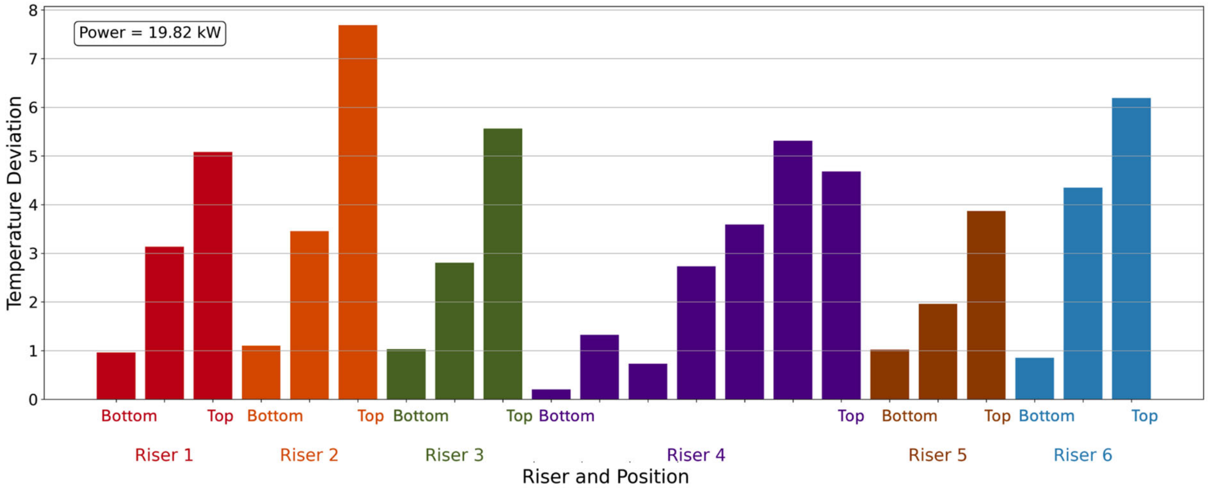

Figure 21. Forced convection low-power riser air temperature difference between RANS and the experiment.

The wall temperatures for the heated cavity were compared with the experiment, at around the middle of the domain. The results are presented in Table 9. The simulation values are in agreement with the experimental values. The back wall shows more deviation from the experimental results, perhaps due to the calculation of view factors in the net radiation method of STAR-CCM+.

3.3. Forced Convection Low-Power-Scenario Sensitivity Study

This section introduces a parametric study designed to explain some of the possible error sources, thus helping to identify possible reasons for the deviation from experimental measurements.

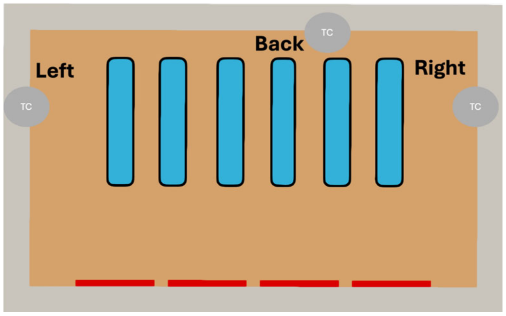

Figure 22. Forced convection low-power comparison of heated cavity wall temperatures.

Table 9. Test 14 heated cavity wall temperature comparison.

Name	STAR-CCM+ (°C)	Experiment (°C)
Left	194.30	190.67
Back	138.83	157.66
Right	191.50	182.82

3.3.1. Air thermocouple position

The experimental report states that the thermocouple used to measure air temperature is located at the center of each channel. Therefore, the center location is used to measure the centerline temperature along the riser height. To perform the sensitivity study, the thermocouple location was shifted both vertically and planarly. Figure 23 shows the vertical and planar direction definitions used for this study. The change in the vertical location was 0.1 cm, whereas the change in the planar location was 0.05 cm. These changes were made according to the elongated duct geometry, which is why the vertical location is shifted to a greater extent than the planar location.

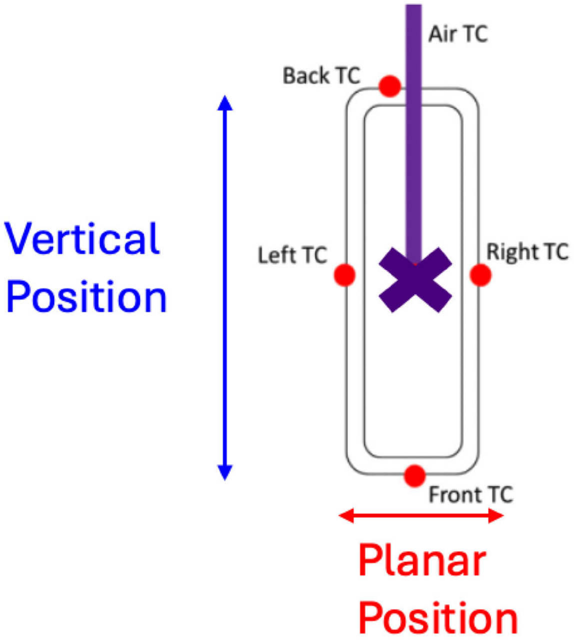

Figure 23. Air thermocouple planar and axial position.

The results of the sensitivity study are shared in Figure 24. The plot on the left shows the thermocouple measurements with changes in the vertical position; the plot on the right shows changes with the planar position. The results demonstrate consistent changes in the asymmetric temperature distribution in the riser ducts. Since the front wall is significantly hotter, the temperature slightly increases as the position moves closer to the front wall. Although the back wall is hotter than the center, its location is farther from the center, resulting in either no change at all or a small decrease in temperature. Both the left and right walls are hotter than the center. They are also closer to the center, causing any change in the planar direction to result in a temperature increase.

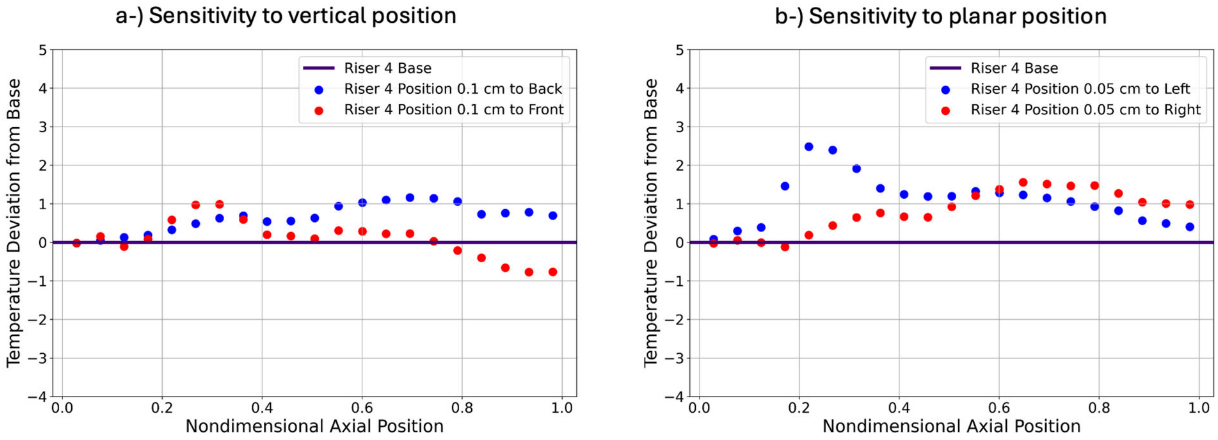

Figure 24. The air thermocouple's sensitivity to planar and axial location for the 4_{th} riser duct.

3.3.2. Heater power distribution

An energy balance comparison between the experiment and simulation was presented in the previous sections. The power distribution in the heaters is assumed to be uniform; however, this assumption may not be valid, as the experimental study does not report measurements on the power distribution of the heaters. The high temperatures make it challenging to perform this study experimentally. Therefore, a sensitivity study was performed on the power distribution in the heaters. The heater sections were divided into two regions—namely, the inner and outer regions, as shown in Figure 25. A power ratio (χ) was defined to show the power differences between these two regions. The ratio shows that the inner region gets more power than the outer one, with "1.5" meaning that the inner region has 50% more power than the outer region.

The results of the sensitivity study are shared in Figure 26. The plot on the left shows the temperature deviation from the base results in the center; the one on the right shows the deviation from the base on the front wall thermocouple, which shows a significant change in power distribution.

3.3.3. Riser duct emissivity

The final sensitivity study examined the emissivity value of the riser ducts. For this study, the emissivity values were adjusted from 0.8 to 0.7 and 0.9. The results are presented in Figure 27, with the wall temperature results on the right and the air thermocouple results on the left. The temperature of the front wall of the 4th riser ducts shows a slight change with varying emissivity. The wall temperature increased slightly with an emissivity of 0.9, while displaying a very similar trend with the lower emissivity value of 0.7. The air temperature slightly increased with higher emissivity and did not show any significant change with decreased emissivity. Since the change in wall temperatures is slight, a significant change in air temperatures is not expected.

3.4. Forced Convection Modeling Conclusion

This study aims to present validated numerical data by employing high-fidelity methods in modeling the RCCS. It is in this regard that the modeling efforts for the experiments conducted at UW-Madison are

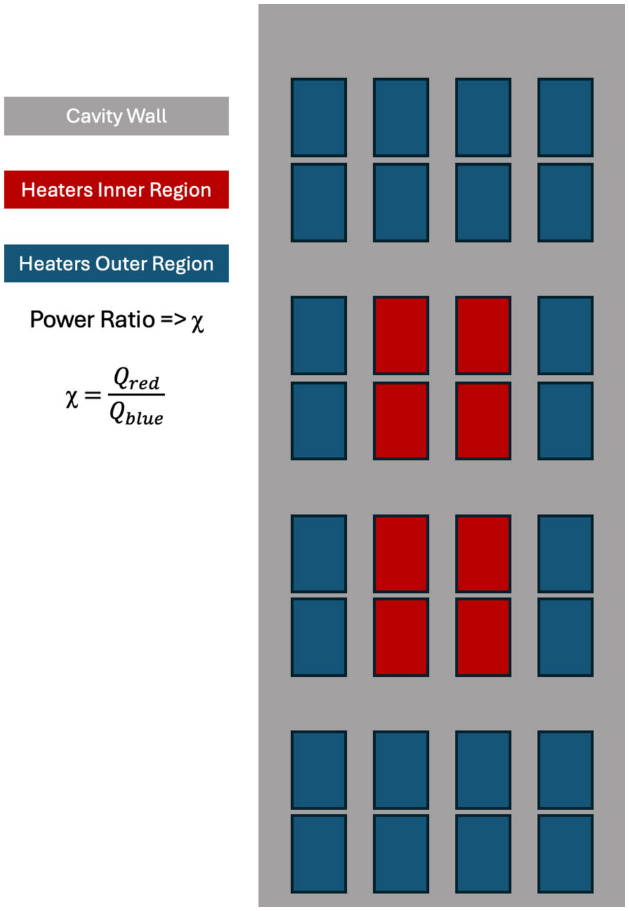

Figure 25. Heater power distribution, where red represents the inner region of the heaters, blue represents the outer region, and gray is the cavity walls.

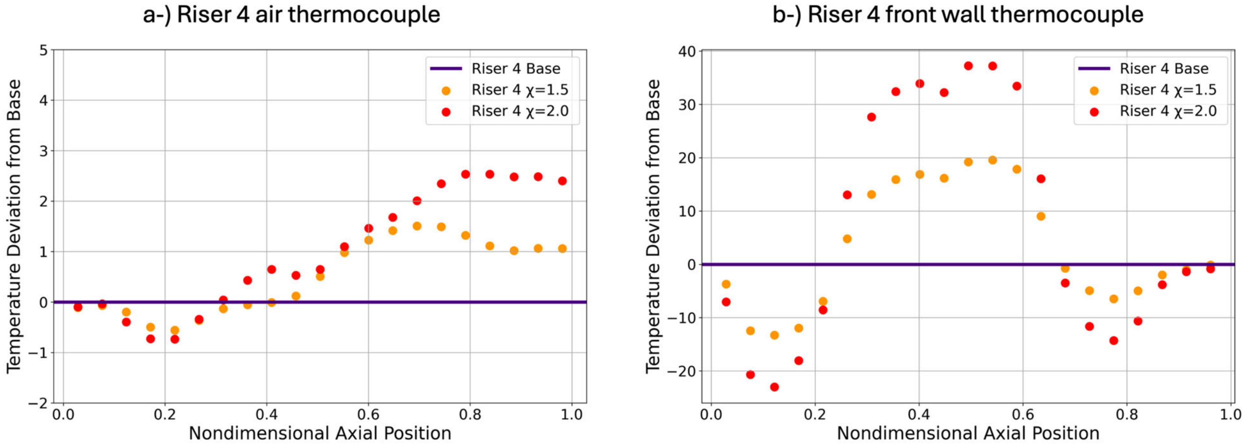

Figure 26. Riser 4's front and center thermocouple temperature measurement sensitivity to heater power distribution.

presented. An LES model of the RCCS was developed using the NekRS spectral element code, representing one of the largest-scale calculations ever performed for the RCCS. The results of this simulation were

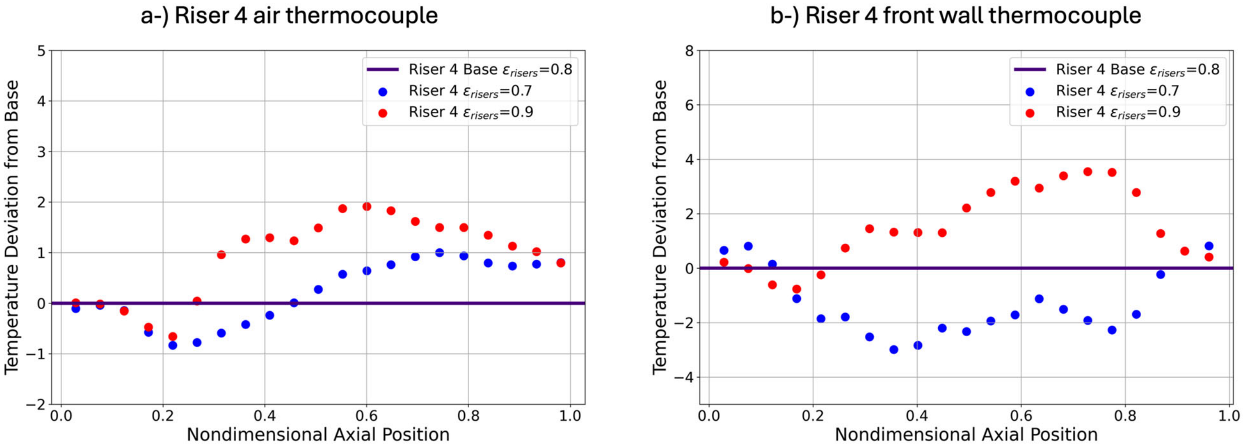

Figure 27. Riser 4's front and center thermocouple temperature measurement sensitivity to riser duct emissivity.

compared to those of an equivalent RANS model of the RCCS, developed using STAR-CCM+. The objective of this comparison was to evaluate turbulence modeling strategies for the RANS model and to determine the most suitable one. Three turbulence modeling strategies were employed for this comparison: realizable k-ϵ, k-ω SST, and Reynolds stress model with elliptic blending. The RSM closely matched the LES model but doubles the computational cost in comparison to the k-ϵ or k-ω models. Thus, the second-best match (i.e., the k-ω model) is preferred for modeling the experimental facility, which includes the RCCS and the heated cavity (mimicking the reactor cavity in the original design).

The last part of the Results section focused on validation of the numerical model for the UW-Madison experimental facility. For two power scenarios, the results obtained from STAR-CCM+ were compared with the experimental measurements at various locations. The wall temperatures of the risers and cavity, in addition to the centerline temperatures of the riser ducts along the height, were compared between the experiment and the simulations, along with the heat balance. The trends in the results agree with those observed in the experimental measurements. The numerical model performed better for the high-power scenario than for the low-power one. The high-power case showed less deviation from the experimental measurements, mainly because the high-power case was able to better match the wall temperatures of the riser ducts. The centerline temperature results also improved with a better match in wall temperatures.

The heat transfer mechanism within the heated cavity was compared for the high- and low-power cases. The results were consistent with the literature. Approximately 80% of the heat was transferred by radiative heat transfer and 20% by convective heat transfer. Additionally, a parametric study was performed on the location of the air thermocouple, the heater power distribution, and the riser duct emissivity. The air thermocouple and heater power distribution seem to have a couple degree effect on the air thermocouple. The heater power distribution has a significant effect on the front wall thermocouple. The effect of emissivity is less significant compared to other parameters in the sensitivity study. The temperature of the front wall of the riser duct increased with higher emissivity and decreased with lower emissivity. The air thermocouple did not show a significant change in response to variations in emissivity.

3.5. Natural Convection RANS Modeling

3.5.1. Natural Convection RANS Numerical Model

The boundary conditions of the RCCS are presented in Figure 28. The shaded parts represent the wall boundary condition for the temperature. The walls in the inlet pipe and plenum are adiabatic, as the heating has not started. For the riser ducts, we have an interface boundary condition between the solid walls of the riser ducts and the fluid. The conjugate heat transfer methodology is applied at the interface, where heat is transferred between the solid and fluid. The outlet plenum has Robin boundary conditions to simulate the convective cooling done by air. The outlet plenum and the exhaust ducts are insulated. However, an unexplained heat loss exists in the system (see Table 10), so that heat is assumed to be lost to the environment via the outlet plenum and exhaust ducts. It is also assumed that the heat transfer coefficient was equal to 2 W/m^2K, and that the ambient temperature was 300 K.

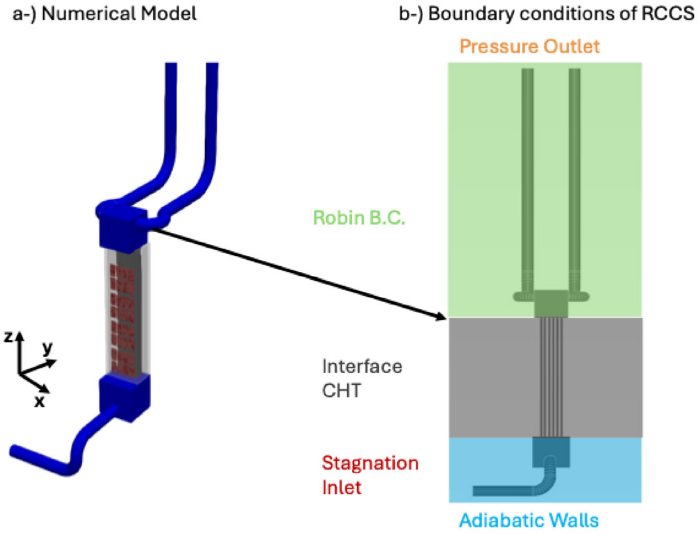

Figure 28. Natural convection boundary conditions for the RCCS.

Fluid property changes are crucial in natural convection cases. The temperature differences were around 100°C in the riser duct during the experiments, meaning that the density differences were significantly large in the system. The density was modeled using the low-Mach approximation based on the ideal gas law (pressure independent). The Boussinesq model was invalid for this case, since the density differences exceeded 10%. The viscosity and thermal conductivity of air were modeled using Sutherland's law. The specific heat capacity was assumed to be a constant 1005 J/kg°C for the air. The turbulent Prandtl number was assumed to be 0.85 for air.

This unexplained heat loss is around 15% of the total power, as seen in Table 10. The first column in the table represents the power supplied to the heaters, while the second column shows the "heat out." The heat can be removed by the system, either through the RCCS or via parasitic heat losses. Heat loss can occur in the heated cavity or in the upper region of the RCCS, through the insulation material. The last column shows the difference between the heat in and the heat out. Since it is a natural convection case, the mass flow rate is a function of power, and the 15% difference in power significantly affects the mass flow rate and therefore the temperature distribution.

Table 10. Experimental data energy balance.

Name	Heat In	Heat Out		Difference
	Heaters In	Heat Removed by RCCS	Total Loss	(Heat In - Heat Out)
High Power	37.97 kW	23.10 kW	8.15 kW	6.72 kW
Low Power	19.82 kW	12.63 kW	4.66 kW	2.53 kW

The boundary conditions of the heated cavity on the axial cut of the domain are presented in Figure 14. The heaters were modeled as a volumetric heat source as in forced convection case. Natural circulation of the air inside the heated cavity was modeled, as it contributes to the heat transfer from the heaters to the riser ducts. The heat conduction equations were solved in the cavity frame, heaters, and solid walls of the riser ducts. The thermal conductivity values were taken from the experimental report [25]. Convective cooling was applied to the outer walls of the cavity frame, under the assumption that the heat transfer coefficient was equal to 15 W/m^2K and that the ambient temperature was 300 K. The heat transfer coefficient was higher for the cavity frame because in the heated cavity model the insulation material is modeled as solid, while for the outlet plenum and exhaust ducts an equivalent heat transfer coefficient is used to make the model more computationally efficient. The reason the solid is modeled in the heated cavity is to enable comparison with experimental temperatures at various locations on the solid walls.

Mesh

The model geometry was prepared using the CUBIT software [36]. The internal meshing tools were employed to create the mesh in STAR-CCM+. The mesh is presented in Figure 29. The polyhedral mesher is preferred. A conformal meshing strategy was employed at the interface to improve the stability for conjugate heat transfer. The mesh near the wall was created by using the prism layer meshing to resolve the fine boundary layer. The average thickness of the fluid elements was 4 mm. The mesh size of the solid was 1 mm in the riser ducts and heater, and 4 mm in the cavity frame. For the boundary layer, three prism layers were employed, for a total thickness of 1 mm. The total number of elements was around 148.31 million cells. A mesh convergence study had already been performed in [43].

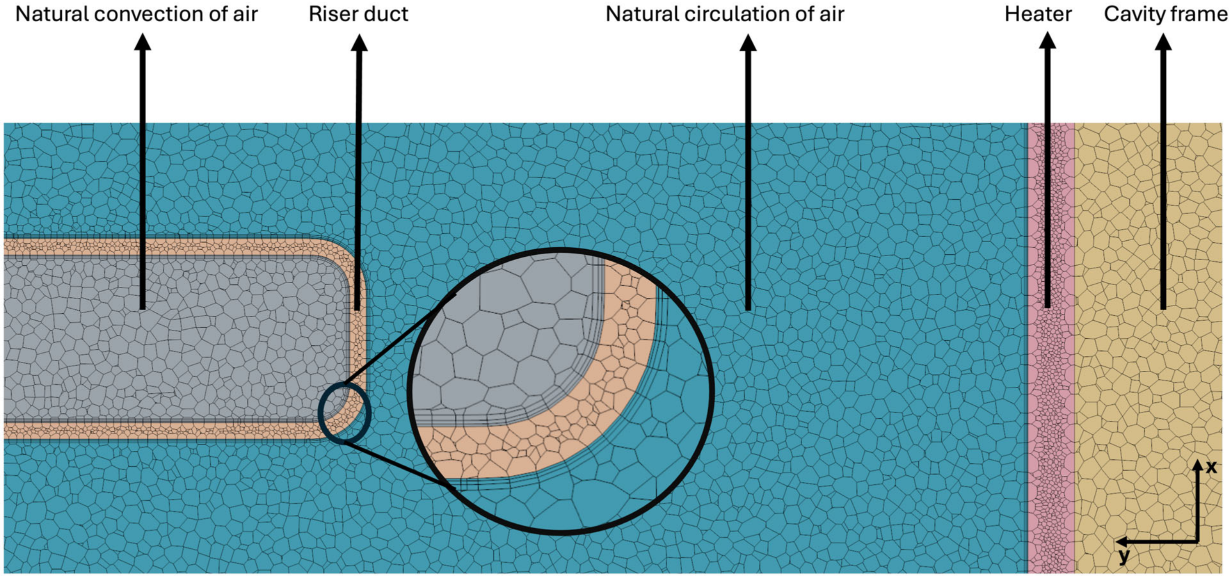

Figure 29. Natural convection STARCCM+ mesh.

To decide the mesh resolution near the wall, a y^+ study was performed. The mesh shown in Figure 29 was run with y^+ values of 0.5 and 25, using the same simulation setup. The wall temperatures showed differences of more than 60°C when comparing the two cases, as shown in Figure 30. In natural convection cases, the buoyancy pressure drop is balanced by the frictional pressure drop. This balance dictates the mass flow rate in the system. The majority of the frictional pressure drop stems from the viscous forces due to the wall effect. Therefore, accurate resolution near the wall is especially important in natural convection cases so as to achieve accurate mass flow rate in the system.

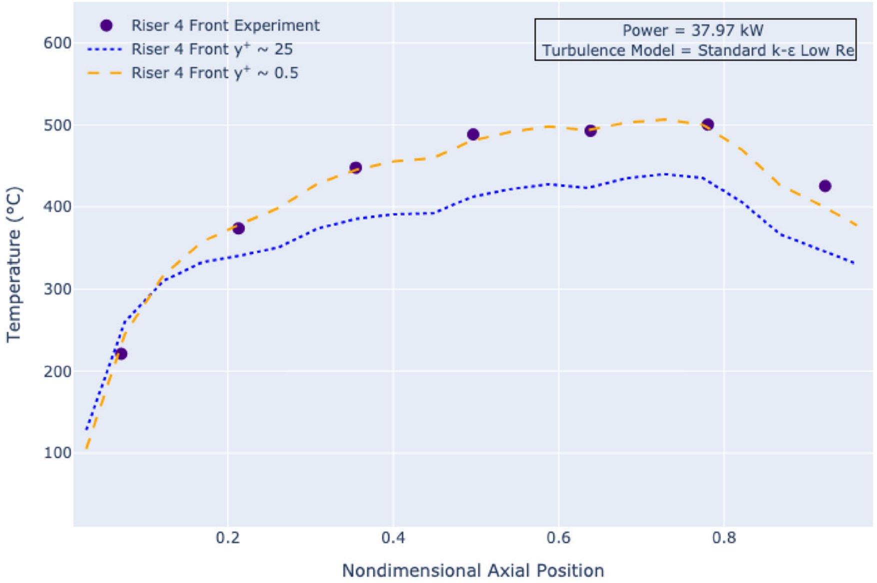

Figure 30. Natural convection y^+ study of the RCCS for the numerical model of the UW-Madison experimental facility.

3.5.2. Validation of RANS Numerical Model

In this section, the numerical model from the RANS model is validated against the available experimental data. The first part focuses on validation of the numerical model. Then heat transfer characteristics are compared between the natural convection and forced convection cases. Lastly, a comparative sensitivity analysis is performed on the turbulence models.

This section compares the high- and low-power experimental measurements against the numerical calculations as model parameters set up in Table 11. Each subsection begins by presenting the energy balance, including a mass flow rate comparison between the experiment and the simulation. The wall temperature profile for the 4th riser, as measured by the experiment, is compared to the numerical calculation. Next, the front wall temperature differences between the experiment and the simulation for all risers are presented in a bar plot. The air centerline temperature profile for the 4th riser is then examined. Subsequently, the centerline temperature differences for all risers are compared in a bar plot. Finally, the temperatures of the walls of the heated cavity are compared between the experimental data and the numerical model.

Natural Convection High-Power Case (37.97 kW)

The energy balance results are shown in Table 12. The second column shows the results from the STAR-CCM+ simulation, while the third column shows the experimental measurements. The first line after the header shows the provided heat inputted to the system, as calculated by the power controller measuring the current. The power removed by the RCCS is calculated using the temperature difference (between the inlet and outlet) and mass flow rate of the system. The results for the experiment and simulations both match.

The total heat losses in the system were calculated in the various parts of the system, primarily centering around the heated cavity. The results are consistent with the experimental results. As seen in the appendix of the experimental report, the heat loss calculations can show significant changes based on the calculation

Table 11. Setup parameters for the numerical model of UW-Madison's air-cooled RCCS for natural convection tests.

Setup Parameters

Modeling Strategy	RANS	
Solver	Segregated-Steady	
Methodology	Finite Volume Method	
# of Elements	148.31 Million	
Turbulence Modeling	$k - \epsilon$ Low Reynolds	
Radiation Modeling	Net Radiation Method	
Buoyancy Modeling	Low-Mach Approximation	
Wall Modeling	Wall Resolved	
Experimental Test #	15	23
Power Levels	Low Power	High Power
Power	19.82 kW	37.97 kW
Inlet Temperature	301.6 K	300.2 K
Fluid Properties	Air	
	Density	Ideal Gas Law
	Viscosity	Sutherland's Law
	Thermal Conductivity	Sutherland's Law
	Specific Heat Capacity	Constant
	Pr_t	0.85

method employed [25]. Thus, an additional heat sink was implemented in the system to account for the further heat losses to the environment that occur on the outlet plenum and exhaust ducts. The additional heat sink is implemented for the unaccounted heat loss in the system, making the energy balance consistent between the experiment and the simulations. Compared to the experimental results, the mass flow rate is slightly underestimated.

Table 12. Natural convection high-power-case energy balance comparison.

Name	*STAR-CCM+*	*Experiment*
Heat In	37.97 kW	
Power Removed by RCCS	23.03 kW	23.10 kW
Total Heat Losses	7.94 kW	8.15 kW
Additional Heat Losses to Environment	7.00 kW	Not measured
Heat Out	37.97 kW	31.25 kW
Mass Flow Rate	0.1450 kg/s	0.1600 kg/s

In Figure 31, the wall temperature distributions for riser duct 4 are compared between the simulation and the experiment. The markers represent the experimental measurements taken by thermocouples on the solid wall. The figure on the right shows the location of the thermocouples. The dashed line represents the simulation results. Since the 4th riser duct is heavily instrumented, the left, right, and back temperatures are also provided. The first subplot shows the front temperatures (i.e., the face that looks toward the heaters, making it more than 100°C hotter than the other walls). Since the view factor is high between the front surface of the riser and the heater, it is expected to show significant temperature differences when compared to the other faces. The simulation temperatures closely match the experimental measurements.

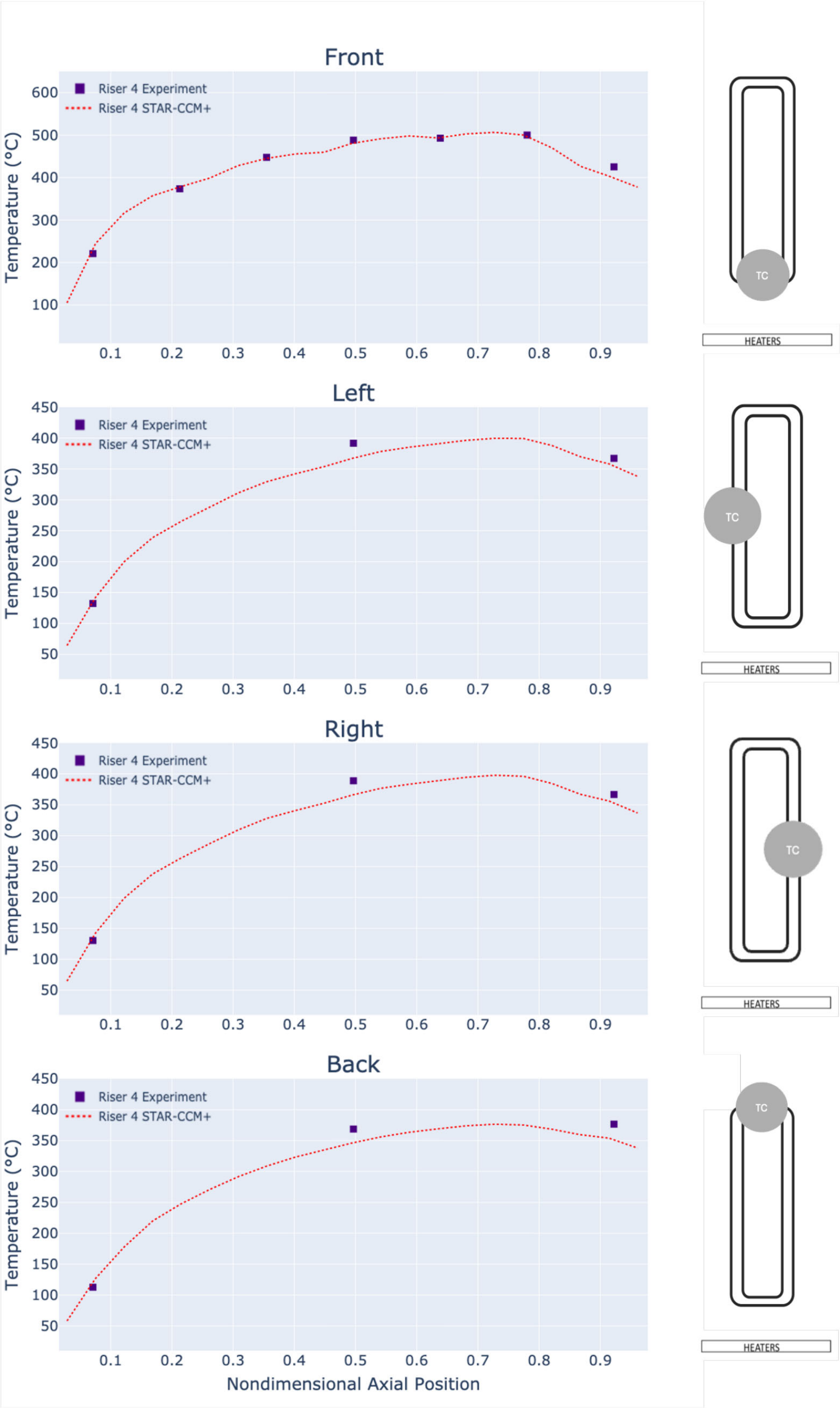

Figure 31. Natural convection high-power comparison of the 4_{th} riser wall temperatures.

A small decrease is shown in the temperature profiles at around the 0.8 non-dimensional axial position. The reason for this decrease is that the heater zone stops at that height. The consistent matching with the experiment shows that the heat transfer within the heated cavity is accurately captured. The radiative heat transfer was modeled using the net radiation methods, which have been demonstrated to be adequate for this system.

The bar plot in Figure 32 shows the front wall temperature comparisons, with each bar color representing a different riser duct, starting with the bottom marker and ending with the top one. The 4th riser has more thermocouples than do the other riser ducts. The numbers of the thermocouples are shown in the right-hand figure. The bars show the temperature difference between the experimental and the simulation results. A positive difference represents overestimation; a negative one represents underestimation by the simulation temperatures. The middle heights match well with the experiments, though some deviation is shown in the bottom and top parts.

There could be multiple reasons for the difference. Overestimation in the bottom part may be caused by the sharp temperature gradient in the temperature profile, where the temperature increases from 200°C to 400°C within the first 0.2 non-dimensional axial position. The RANS models might be unable to capture this sharp temperature change. Additionally, the flow patterns in the top and bottom sections of the heated cavity may contribute to the deviation. Since the flow changes direction in those parts, the RANS models might be unable to accurately capture the changes in flow. Furthermore, experimental results could face the same uncertainty in the flow directions, making it hard to obtain representative data for those locations.

Figure 32. Natural convection high-power front wall comparison of all riser ducts.

The air centerline temperatures for the 4th riser are presented in Figure 33. The results match the experimental results. The trend is underestimation at the bottom and middle sections, and overestimation at the end of the channel.

Figure 34 compares the air centerline temperatures of all the risers. The results are similar to those observed for the 4th riser. There is a slight underestimation at the entrance of the channel, whereas the simulation overpredicts the centerline temperature at the end of the channel. One reason for this is the mismatch in mass flow rate. The mass flow rate is lower than the experimental measurements, thus causing the elevated temperatures at the end of the riser ducts. Additionally, a simple turbulent heat flux model was adopted for this analysis, and can contribute to the error in the natural convection setups.

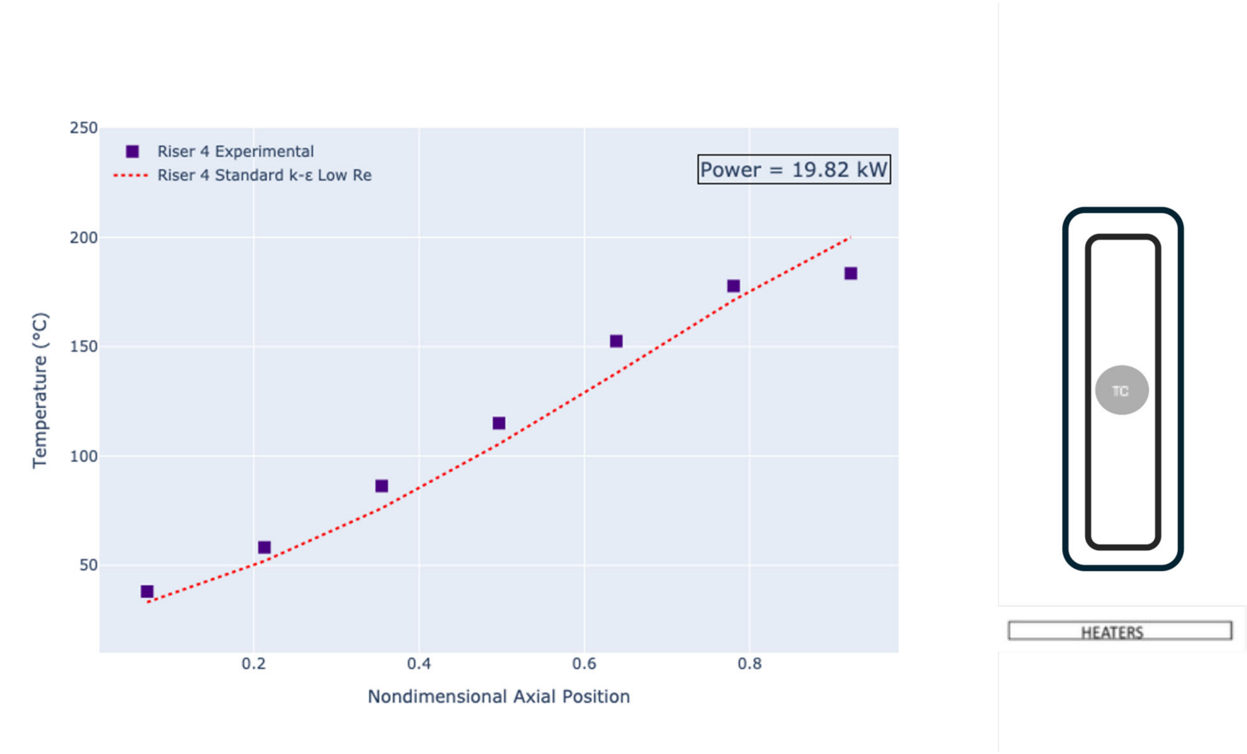

Figure 33. Natural convection high-power comparison of the 4_{th} riser centerline temperatures.

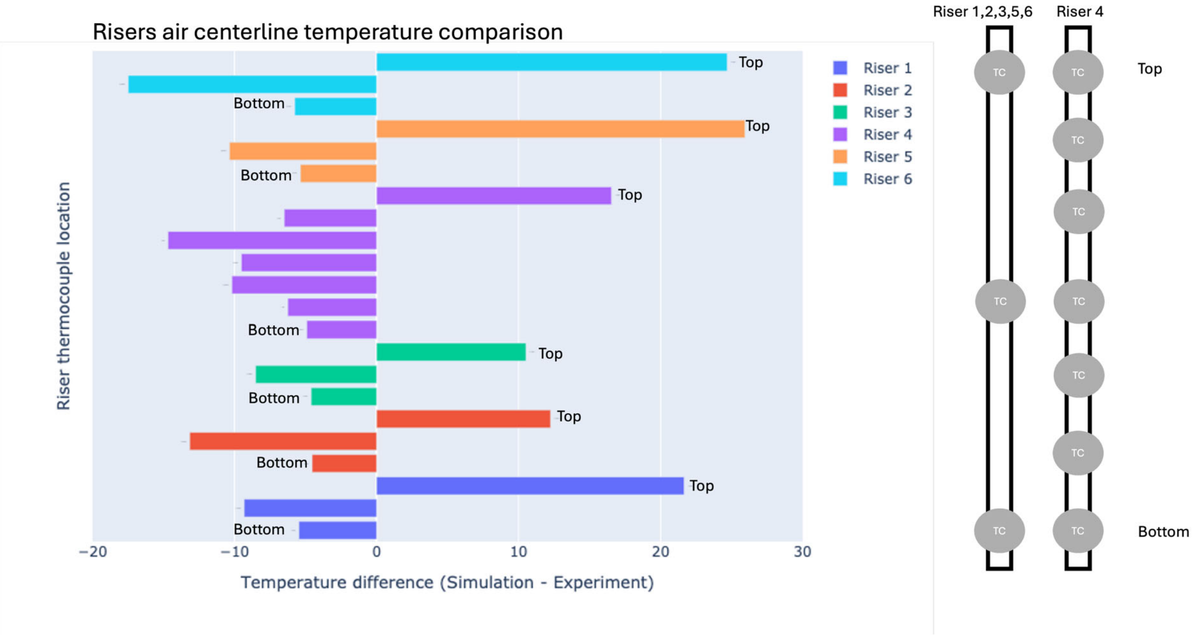

Figure 34. Natural convection high-power comparison of the air centerline temperatures of all the riser ducts.

The final part of this section compares the wall temperatures in the heated cavity. The temperatures of the left, right, and back walls at the middle of the domain were all calculated. The thermocouple positions can be obtained from the experimental report [25]. Table 13 shows the wall temperature difference between the heated cavity and the experiment. The simulation overestimates the left and right wall temperatures but underestimates the back wall temperature. The dominant heat transfer mechanism in the heated cavity is radiative heat transfer. Since the wall temperatures match, the radiative heat transfer is expected to be accurate. The slight difference could be due to uncertainty in the insulation material thickness or in the heat transfer coefficient used for the outside of the heated cavity.

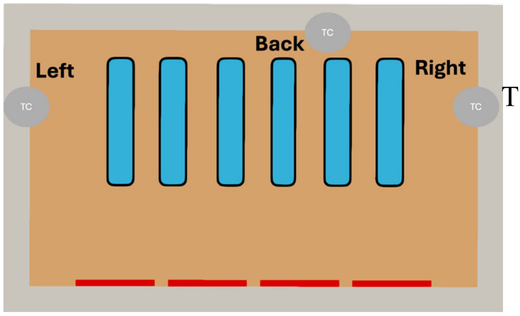

Table 13. Test 23 Wall temperature comparison

Name	STAR-CCM+ (°C)	Experiment (°C)
Left	461	431
Right	457	429
Back	378	387

Figure 35. Natural convection high-power heated cavity wall comparison.

Natural Convection Low-Power Case (19.82 kW)

The same model was run for the low-power scenario. The power in this case was 19.82 kW. The energy balance results are shown in Table 14. The power removed by the RCCS is slightly underestimated in this case, and thus so is the mass flow rate. Considering the complexity of the case, the model performs adequately. The numerical model may overestimate the heat going to the additional heat sink, which covers the heat losses to the environment via the outlet plenum and exhaust ducts.

Table 14. Natural convection low-power-case energy balance comparison.

Name	*STAR-CCM+*	*Experiment*
Heat In	19.82 kW	
Power Removed by RCCS	10.33 kW	12.63 kW
Total Heat Losses	4.87 kW	4.66 kW
Additional Heat Losses to Environment	4.62 kW	Not measured
Heat Out	19.82 kW	17.29 kW
Mass Flow Rate	0.1033 kg/s	0.1389 kg/s

In Figure 36, the wall temperature profiles for riser duct 4 are compared between the simulation and the experiment. The numerical model is able to capture the same trends observed in the experiments. A slight underestimation of temperature is caused by underestimation of the mass flow rate. Since less power is going to the RCCS, this slight underestimation of the temperature values is expected. In general, the simulation successfully reflects the same behavior as the experimental measurements.

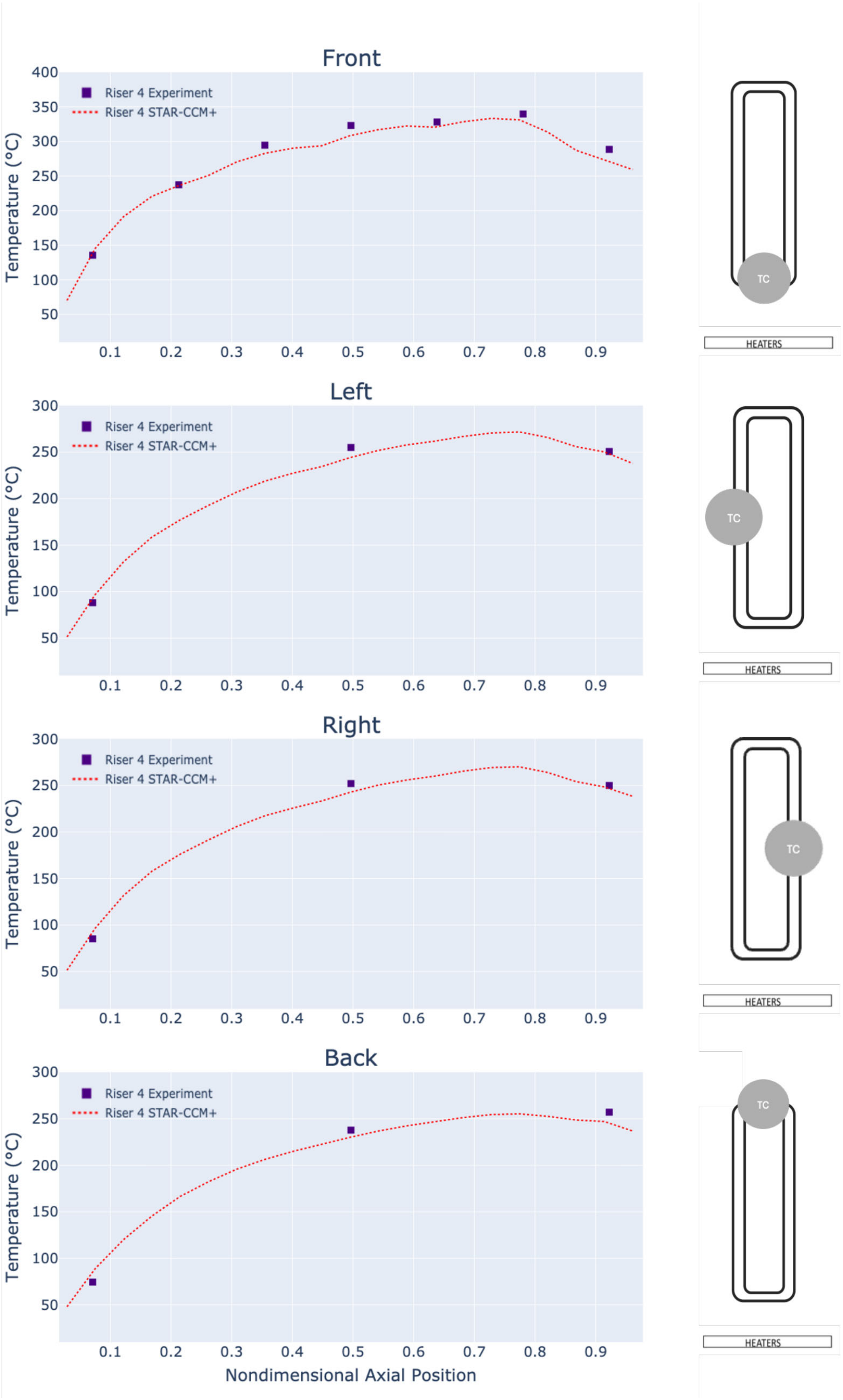

Figure 36. Natural convection low-power comparison of the 4_{th} riser wall temperatures.

The wall temperature profiles for all the riser ducts are compared in Figure 37 via a bar graph. Each bar shows the temperature difference between the experiment and the simulation. The temperature values are overestimated in the first point, where the sharp gradient occurs. A slightly lower temperature value is then observed in comparison to the experiment.

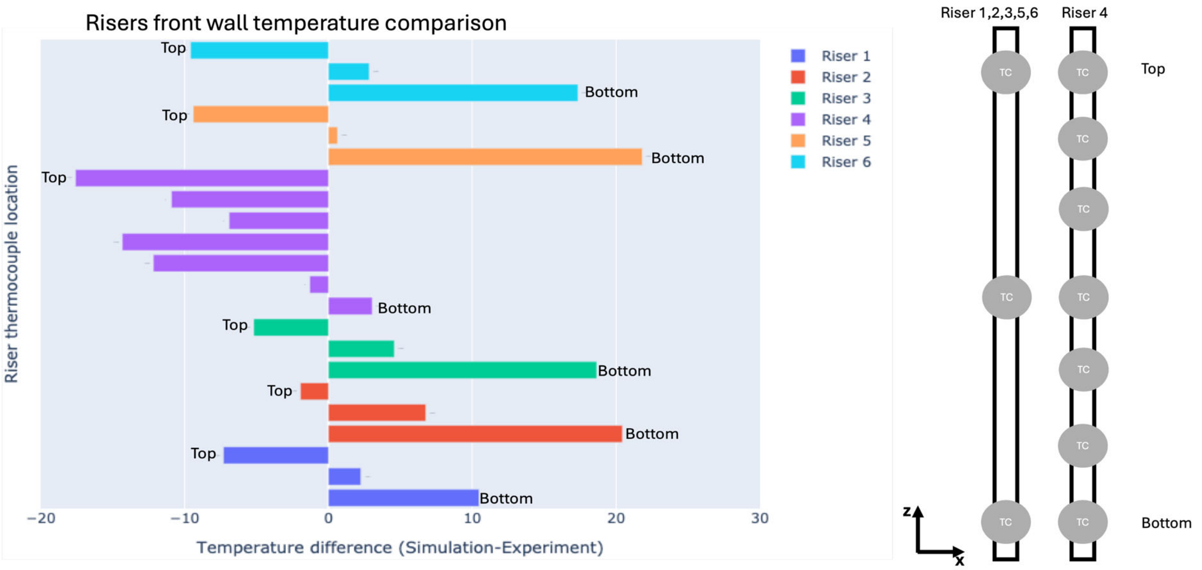

Figure 37. Natural convection low-power front wall comparison of all the riser ducts.

The air centerline temperatures for the 4_{th} riser are compared in 38. The temperature values match the experimental results for the lower half of the channel, but the upper half shows some deviation. The deviation increases at the end of the channel with more heating. A primary reason for this could be the lower mass flow rate. In addition, a very simple turbulent heat flux model was used in this numerical model. Furthermore, the simple gradient hypothesis could be contributing to the deviation.

The air centerline temperatures for all the riser ducts are compared in Figure 39. All riser ducts show the same behavior as previously observed in the 4_{th} riser duct. In all the riser ducts, there is a trend in which the deviation from the experimental results increases with heating. The maximum deviation is reached at the end of the channel. In addition to the lower total mass flow rate, mixing in the outlet plenum of the riser ducts can also contribute to this deviation.

The heated cavity wall temperatures are compared in Table 15. The wall temperatures on the heated cavity are slightly overestimated, but generally match the experimental measurements. At both power levels, the heated cavity and riser duct wall temperature predictions are consistent with the experimental measurements. Based on these results, the RANS model is able to predict the correct temperature distribution within the heated cavity.

3.5.3. Heat Transfer Modes in the Heated Cavity

This section presents the heat transfer mechanism between the heaters and the riser ducts in the heated cavity. The figure below compares the convective and radiative heat transfer for the low- and high-power scenarios in both forced and natural convection setups.

The forced convection results have already been presented in [43]. The figure shows the dominant heat transfer mechanism to be radiative heat transfer in the heated cavity. Radiation is more pronounced in the natural convection cases than in the forced convection cases. The contribution of the radiative heat transfer is around 88% in the natural convection cases, but around 78% in the forced convection cases. The

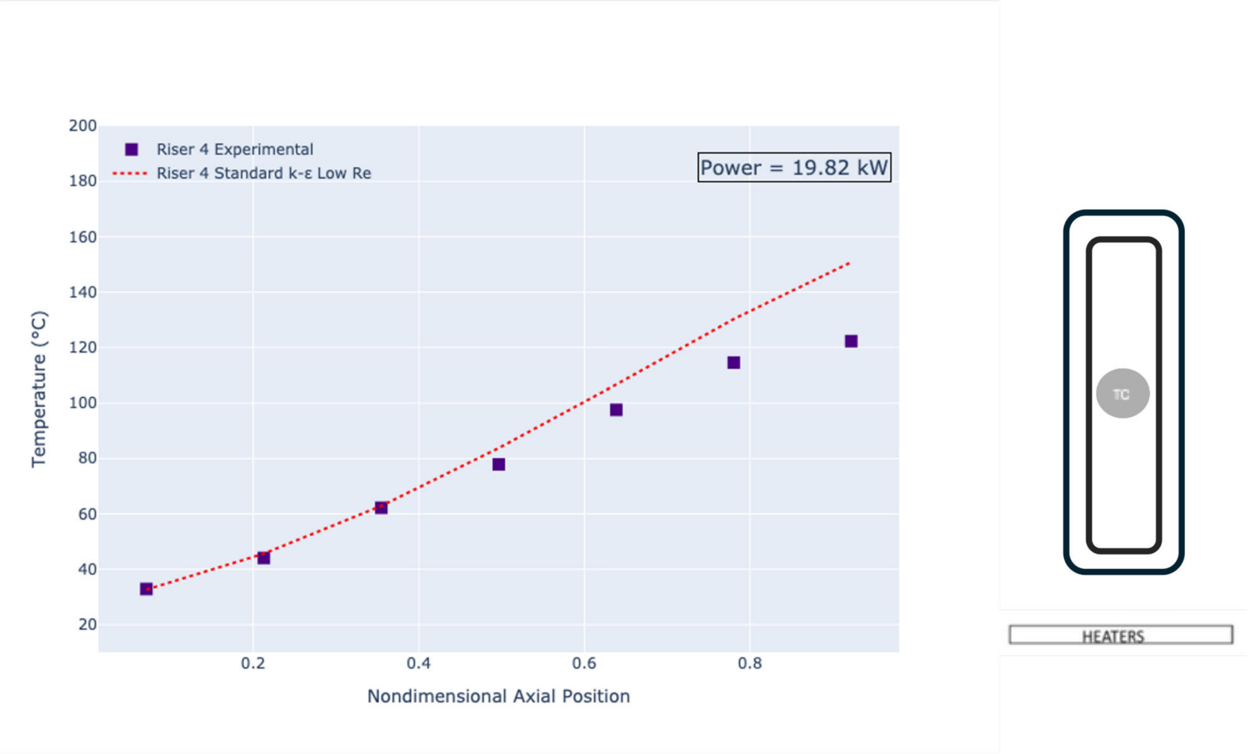

Figure 38. Natural convection low-power comparison of the 4_{th} riser centerline temperatures.

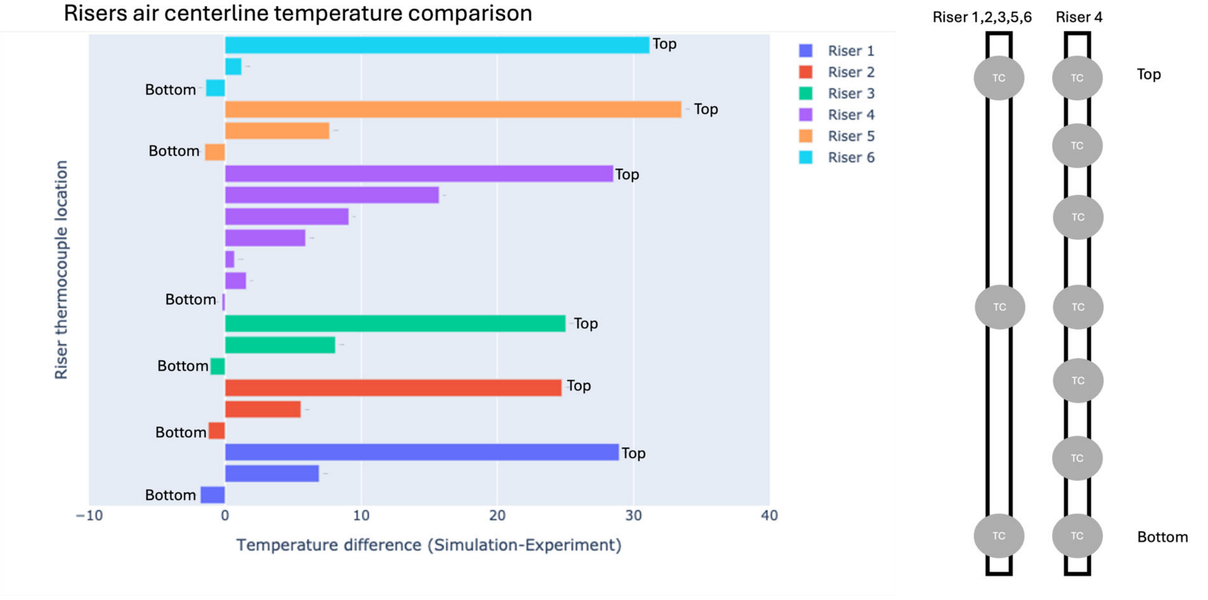

Figure 39. Natural convection low-power comparison of the air centerline temperatures of all the riser ducts.

natural and forced convection cases exhibit identical behavior as the power increases. In both setups, the contribution from radiation increases, mainly because radiative heat transfer changes with the fourth power of the temperature.

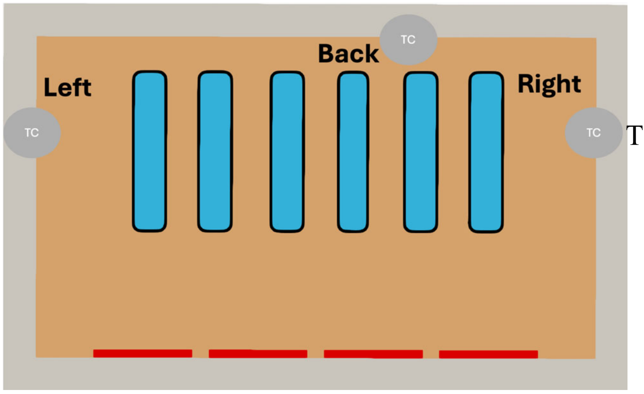

Figure 40. Natural convection low-power heated cavity wall comparison.

Table 15. Test 15 Wall temperature comparison

Name	STAR-CCM+ (°C)	Experiment (°C)
Left	305	290
Right	302	285
Back	251	256

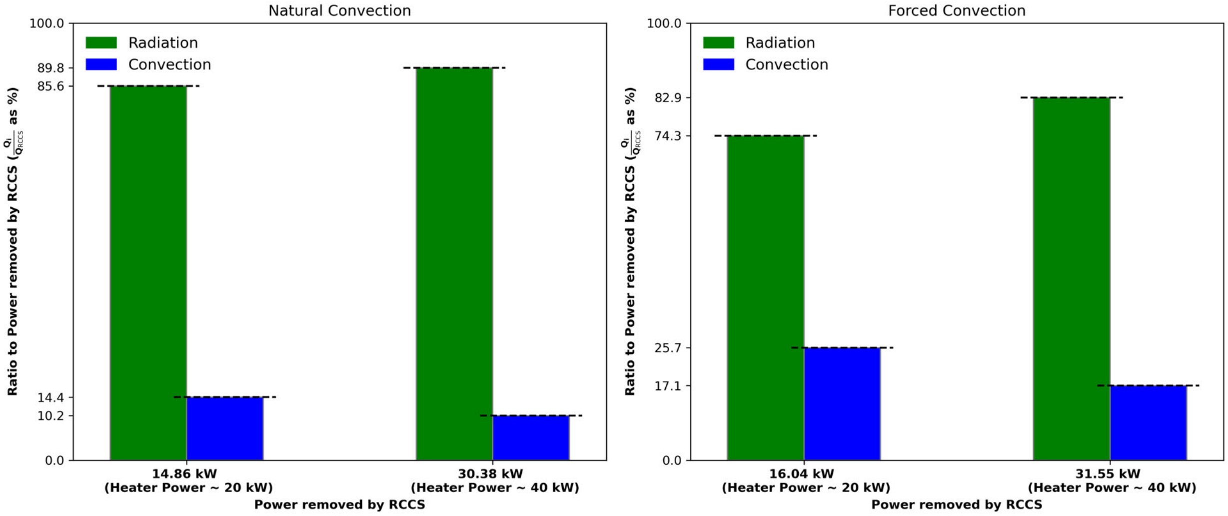

Figure 41. Modes of heat transfer between the heaters and RCCS for forced and natural convection.

3.5.4. Natural Convection RANS Turbulence Modeling Strategy

This section presents the sensitivity of the RANS turbulence models. Multiple modeling strategies have been implemented: standard k-ϵ low Reynolds, realizable k-ϵ (two layer), k-ω SST, and Spalart-Allmaras. These turbulence models entail different levels of complexity and assumptions for modeling the effect of the fluctuating components on averaged fields. The calculations used were on the front wall and air centerline temperatures for the 4th riser. Figure 42 shows the effect on the front wall temperatures. Most of the models are able to predict temperature values close to the experimental measurements. The best-matching model is the standard k-ϵ low Reynolds model. The main difference between the models is seen in the sharp temperature gradient before the 0.2 non-dimensional axial position. Some models predict high temperatures in this region.

Figure 43 compares the air centerline temperatures for all the turbulence models. All RANS models were able to predict the same trend as observed in the experimental outcomes. Most models tended to underpredict the temperature profile up until the last measurement point. At the last measurement point, all models overpredicted the temperature. The k-ω SST model best matched the experimental temperature distribution. (It should be noted that this is not the bulk temperature, but rather the centerline temperature. Therefore, differences in this distribution do not indicate that less energy is going into the riser duct.) Since we have

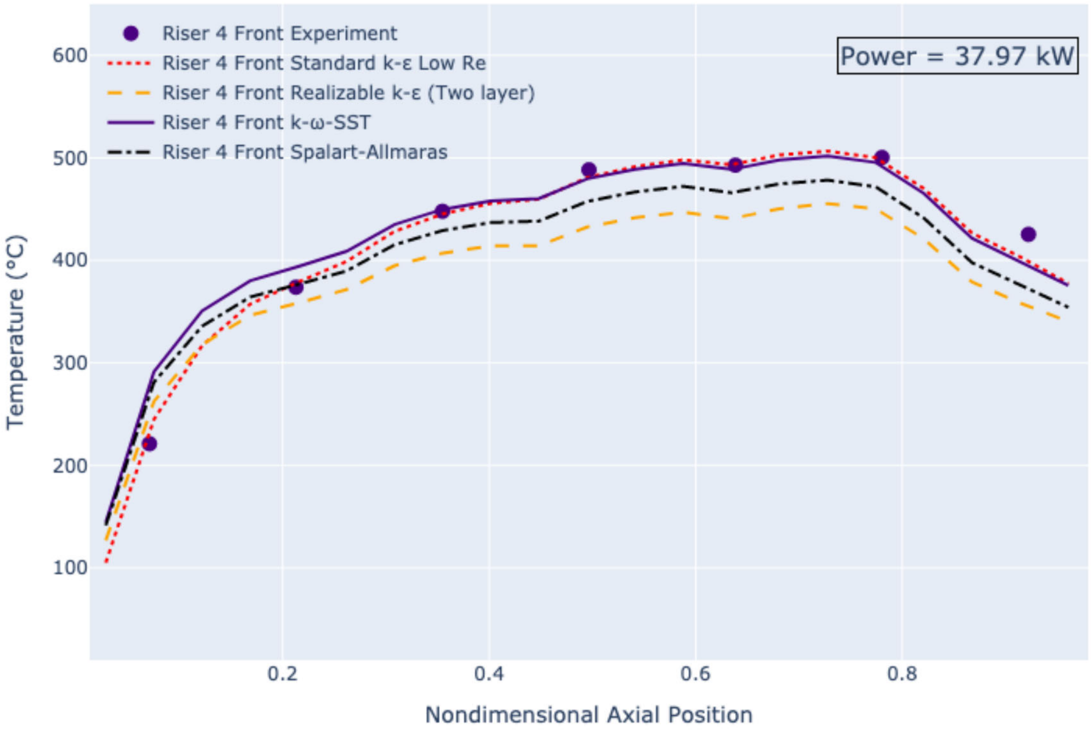

Figure 42. Natural convection effect of RANS turbulence models on the front wall temperatures of the 4_{th} riser duct.

highly asymmetrically heated riser duct walls, the RANS turbulence models were expected to show some differences in regard to their temperature distributions.

3.6. Natural Convection Modeling Conclusion

The numerical model was validated against the available experimental data from the air-cooled RCCS experimental facility in UW-Madison. The first part of the results focused on validation of natural convection tests for high- and low-power cases under a uniform power profile. For each power level, the comparison began by showing the energy balance, including a mass flow rate comparison between the experiment and the simulation. Next, the wall temperature profiles for the 4_{th} riser were compared. Following this, the front wall temperature differences between the experiment and the simulation, for all risers, were shown in a bar plot. The air centerline temperature profiles for the 4th riser were then compared. The centerline temperature differences for all risers were compared in a bar plot as well. Finally, the wall temperatures of the heated cavity were compared.

Steady-state analysis was performed using the segregated solver approach on STAR-CCM+. The standard $k-\epsilon$ low Reynolds turbulence model was used. Radiation was modeled via the net radiation method, and buoyancy was modeled with the low-Mach approximation. The fluid properties were modeled as being temperature-dependent, except for the specific heat capacity, which was assumed constant for the temperature

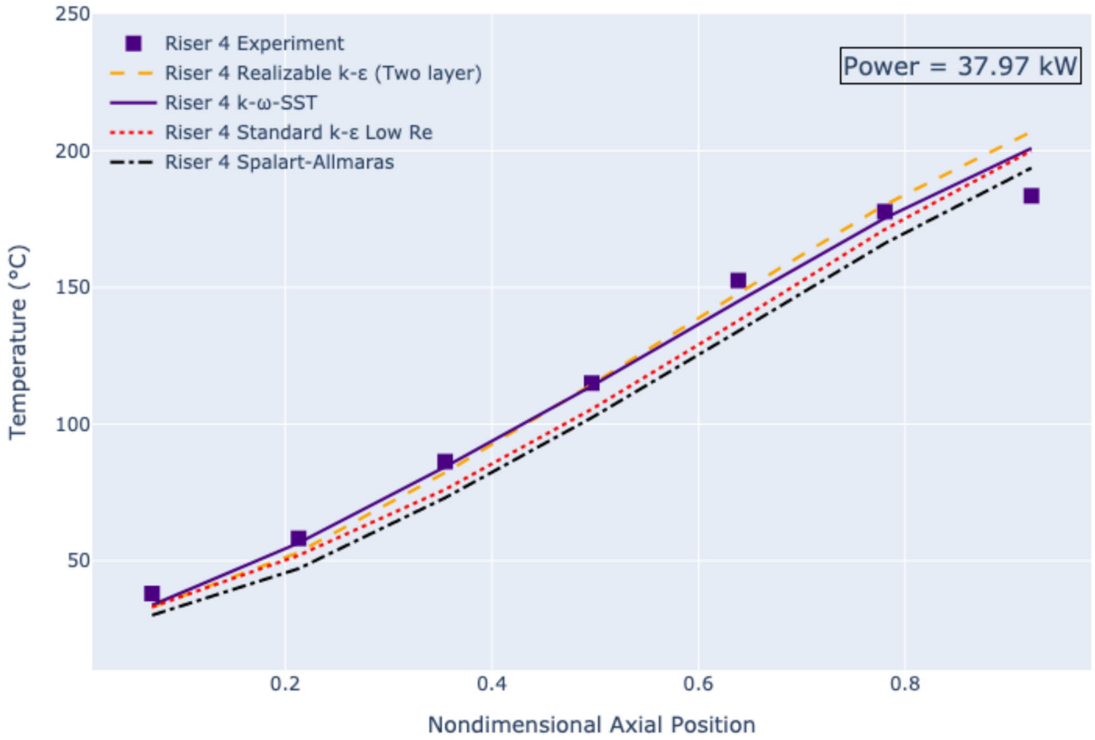

Figure 43. Natural convection effect of the RANS turbulence models on the air centerline temperatures of the 4_{th} riser duct.

range of interest in this study. Wall-resolved simulations were performed to ensure that the wall friction was accurately captured.

The results show that the $k - \epsilon$ low Reynolds RANS numerical model was able to successfully predict the correct temperature trends and values measured in the experiment. Each part of the Results section began with an energy and mass balance comparison between the experiment and the simulation. The energy balances from the experiment and the simulation matched in all cases; however, the standard $k - \epsilon$ low Reynolds RANS models predicted a lower mass flow rate for both power levels. The mass flow rate was better captured at high power levels than at lower ones. This deviation might be caused by implementation of the additional sink included to model the missing 20% of the energy reported in the experiments. This energy imbalance became crucial for the natural convection simulations, in which the mass flow rate was a function of power. We assumed the missing 20% energy to have leaked to the environment through the exhaust ducts and outlet plenum.

The riser duct wall temperatures matched well when comparing the experiment and simulation results. The trends and values observed in the experiments were captured in the numerical model. Most of the deviation occurred between the first and second axial positions, where a sharp temperature gradient was observed. For the low-power case, the wall temperatures were slightly underestimated, whereas the high-power case better matched the experimental measurements. Next, the air centerline temperatures were compared for all the riser ducts. The high-power case showed a better match in air centerline temperatures than did the low-power case. On the other hand, in comparison to the experiment, the low-power case showed a higher temperature in the center of the riser duct. The most probable reason for this is underestimation of the flow rate. Using a simple gradient diffusion hypothesis for the turbulent heat flux also contributed to the deviation. In the last part of each section, heated cavity wall temperatures were compared between the experiment and the simulation. These temperatures matched well overall, with the left and right wall temperatures being overestimated but the back wall temperature being slightly underestimated. Based on comparison of the wall temperatures of the riser ducts and the heated cavity, the numerical model is able to accurately capture the temperature distribution within the heated cavity.

Additional analyses were performed using the validated numerical RCCS model of the experimental facility at UW-Madison. The heat removal characteristics of the heated cavity were produced. The heat was expected to be transferred from the heaters to the risers, predominantly via radiation. The results for the natural convection cases show that 85% of the total heat removed by the RCCS was received from the heaters through radiative heat transfer, while the other 15% was received through convective heat transfer. The heat transfer characteristics of the heated cavity were compared with the forced convection tests, demonstrating convective heat transfer to be less effective in the heat removal by the RCCS in the natural convection setup as compared to the forced convection tests. In both setups, the percentage of radiative heat transfer increased in direct proportion to the power, most likely due to the T^4 dependence of radiative heat transfer.

The last analysis in the Results section demonstrated the importance of the selected RANS turbulence model in simulating natural convection. To this end, the natural convection case was modeled by using four different RANS turbulence models, and the simulation results were then compared against each other. The wall temperatures and air centerline temperatures in the 4th riser duct were compared. All the models were able to successfully reproduce the correct trends observed in the experiments. Comparison of the wall temperatures showed that, depending on the turbulence model, wall temperatures can change by up to 50°C for the RCCS natural convection setup. For the wall temperatures, the standard $k-\epsilon$ low Reynolds model performed better than the other three models. Next, the air centerline temperatures were compared for all the models. The selected models underestimated the air centerline temperature, though the k-ω SST model performed better than the other three. (It should be noted that the compared values were the time-averaged temperatures in the air centerline and not the bulk values; therefore, the energy balance was consistent between the models.)

4. BYPASS FLOW VALIDATION

Although HTGRs present a number of advantages over the United States' existing LWR fleet, they still face a number of challenges relevant to design, licensing, and deployment. One HTGR phenomenon that requires additional analysis is core bypass flow. The arrangement of the graphite blocks that compose the reflector and main structure of an HTGR is imperfect, and small gaps often exist between blocks. These gaps provide additional flow paths for coolant gas, and the gas can flow around the reactor core instead of through it, effectively bypassing the core. This reduces the amount of coolant flowing through the heat core region, and can impact the core outlet temperature as well as maximum fuel temperatures. Bypass flow can account for over 10% of the total system flow rate, highlighting the necessity of accurately accounting for bypass flow in HTGR analysis calculations. This phenomenon is relevant for the reflector blocks in PBRs, and for both the reflector and core blocks in prismatic HTGRs.

Numerous studies have been conducted to obtain an improved understanding of bypass flow in HTGRs. Viljoen et. al [44] performed a coupled CFD and porous media simulation of the German Arbeitsgemeinschat Versuchsreaktor (AVR) to analyze the effect that bypass flow may have had on maximum fuel temperatures. Their results indicated that inclusion of bypass flow in predictive AVR models can influence maximum coolant temperature predictions by roughly 100°C. The authors remarked that this bypass flow may have been a large contributor to the higher-than-expected temperatures measured in the AVR melt wire experiments [45]. As a result of the identified importance of correctly predicting core bypass flow, the pebble-bed modular reactor (PBMR) program in South Africa performed analysis of core bypass flow [46]. They identified that changes in pebble bed pressure drop does not constitute a proportional change in bypass flow. They also found that inclusion of bypass flow influenced maximum temperature predictions for the PBMR by more than 10%. More recently, the development of the HTR-PM reactor in China also made use of CFD to investigate bypass flow [47]. They performed CFD and porous media simulation of a slice of the HTR-PM. Their investigation revealed a smaller influence of bypass flow than previous studies, with the bypass flow only increasing the maximum fuel temperature by about 10°C. In addition to the effect of bypass flow on fuel temperatures, researchers in the HTR-PM project have also investigated the effect of bypass flow on mixing in the lower plenum of the HTR-PM [48]. They performed CFD simulation of the HTR-PM lower plenum to quantify the effects of mixing cold bypass flow with hot reactor outlet gas. They found that bypass flow significantly increased the heterogeneity of the helium at the outlet of the lower plenum—with a temperature difference of roughly 18°C between the maximum and minimum values. They note, however, that this temperature difference is still within the operating conditions for the steam generator.

Several experimental investigations have also been performed to analyze bypass flow in HTGRs. Due to the complex geometries associated with HTGRs, experiments are typically limited in both size and the amount of data that can be extracted. Nonetheless, they are vital for validation of numerical models for predicting bypass flow. A series of bypass flow experiments was performed at Seoul National University (SNU) and the Korean Atomic Energy Research Institute (KAERI) [49]. They performed experiments with three different test sections, each increasing in complexity from a simple unit cell to a multi-assembly representation. Flow meters were used to assess the percentage of bypass flow in each test section for several different configurations. These configurations provided representations of the bypass flow in various regions of the core by varying the use of fuel blocks and reflector blocks. Researchers at Texas A&M University performed a study similar to the experiments performed at SNU [50]. Their experiments featured three hexagonal fuel blocks, with a variable bypass gap between them. Experiments were performed at multiple bypass gas sizes and flow rates to quantify the effects of these parameters on the bypass flow ratio. The matched index of refraction (MIR) facility at Idaho National Laboratory (INL) has also been used to study core bypass flow [50–52]. This facility utilized a test section representing a unit-cell geometry in a prismatic HTGR, and this geometry consisted of nine coolant channels, a vertical gap, and a horizontal gap. Particle image velocimetry (PIV) was used to measure bypass flow data at multiple flow rates and gap sizes. Use of PIV allowed for the extraction of velocity measurements within the domain, providing a wealth of data for validation purposes. Pressure drop measurements were also taken.

The present work will utilize the INL MIR and the SNU/KAERI facility to validate CFD tools for predicting core bypass flow in prismatic HTGRs. LES and RANS simulations will be performed and compared with each other and with experimental measurements from the INL MIR and SNU experiments.

4.1. INL MIR Facility

The MIR bypass flow experiments at INL were used to gain additional insight into bypass flow in HTGRs [51]. The facility consisted of a prismatic unit-cell geometry featuring nine coolant channels, a vertical gap, and a horizontal gap. It was based on the GA-MHTGR design, and scaled by a factor of 2.016 to align with the availability of construction components. The test section was constructed out of quartz, with mineral oil being used as the working fluid so as to provide a matched index of refraction. An overview of the test section is shown in Figure 44.

The sizes of the two gaps were controlled using spacer blocks. The experiments used in this work were designed with a vertical gap width of 6.05 mm and a horizontal gap width of 2.02 mm. The experimentalists note that the actual vertical gap width was not perfectly aligned with the target gap width. They measured

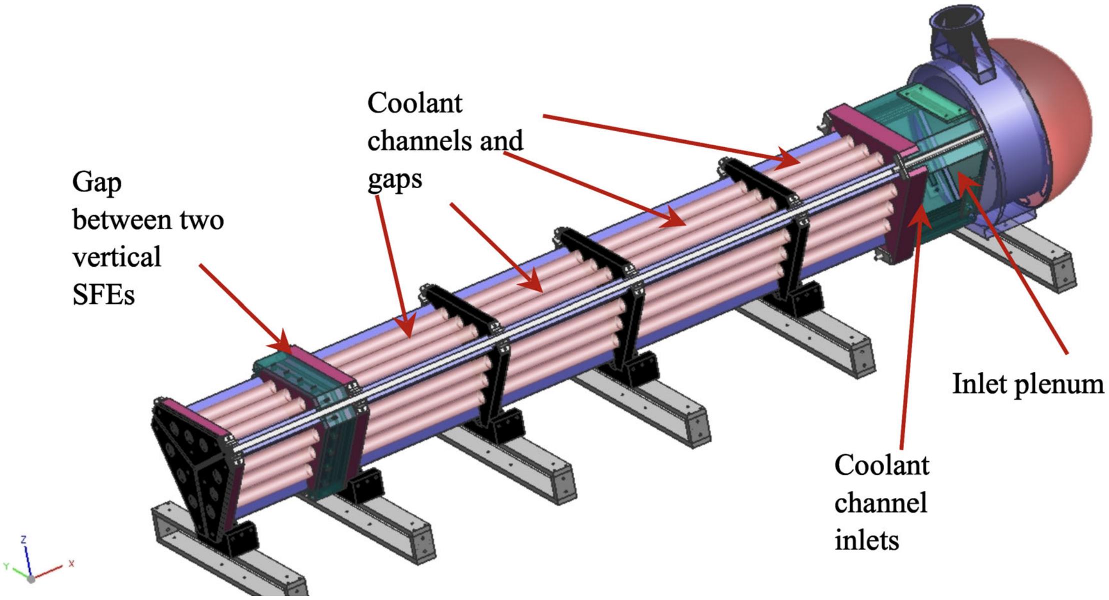

Figure 44. Experimental geometry for the INL MIR bypass flow experiment.

and reported the as-built gap widths, shown in Figure 45. These non-uniform gap sizes are considered in the CFD model.

Experiments were performed at three different flow rates to provide flow conditions that are laminar, transitional, and turbulent in the nine channels. The flow rates used in the experiment were 351.1, 579.9, and 1004.1 gal/min, corresponding to Reynolds numbers of roughly 1,700, 2,800, and 4,600 in the coolant channels. PIV was used to measure the flow field at several locations within the test section. The primary locations that will be considered in this work are roughly halfway between the inlet plenum and horizontal gap, and roughly halfway between the horizontal gap and the end of the test section. These two measurement planes will be referred to as the upper and lower measurement planes, respectively. PIV data was used to determine and report the percentage of flow that passes through the bypass gap and coolant channels. Additionally, line samples of the flow velocity were provided at several locations (see) Figure 46).

In addition to PIV measurements, pressure measurements were also taken via four pressure transducers. Three of these probes were placed in the inlet plenum; the fourth was located in the horizontal gap. These provided pressure drop measurements during the experiments.

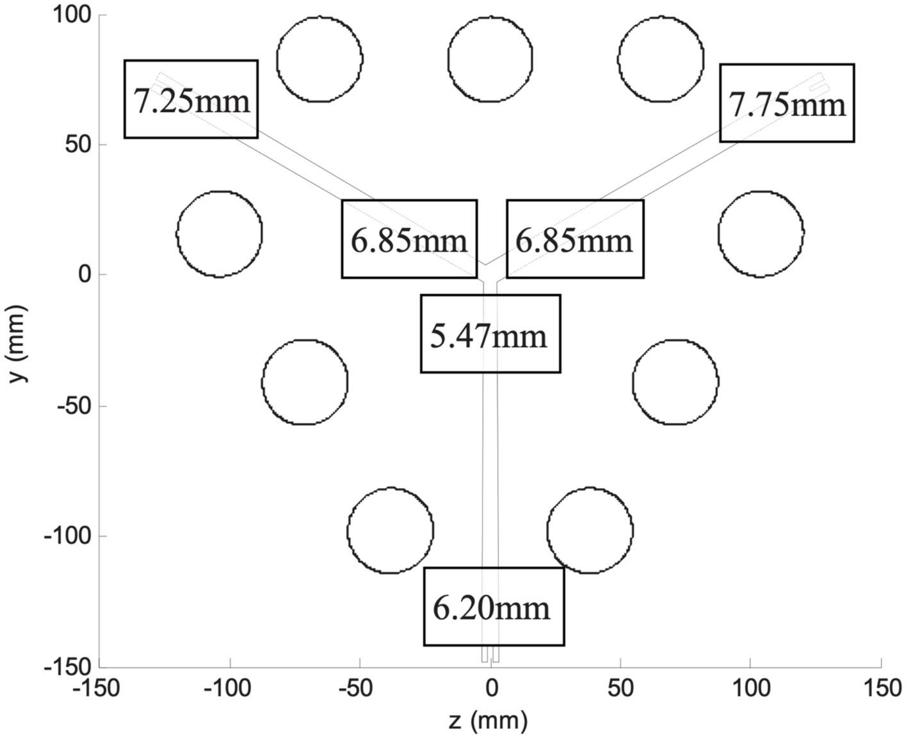

Figure 45. Experimentally determined gap sizes for the INL MIR bypass flow experiments.

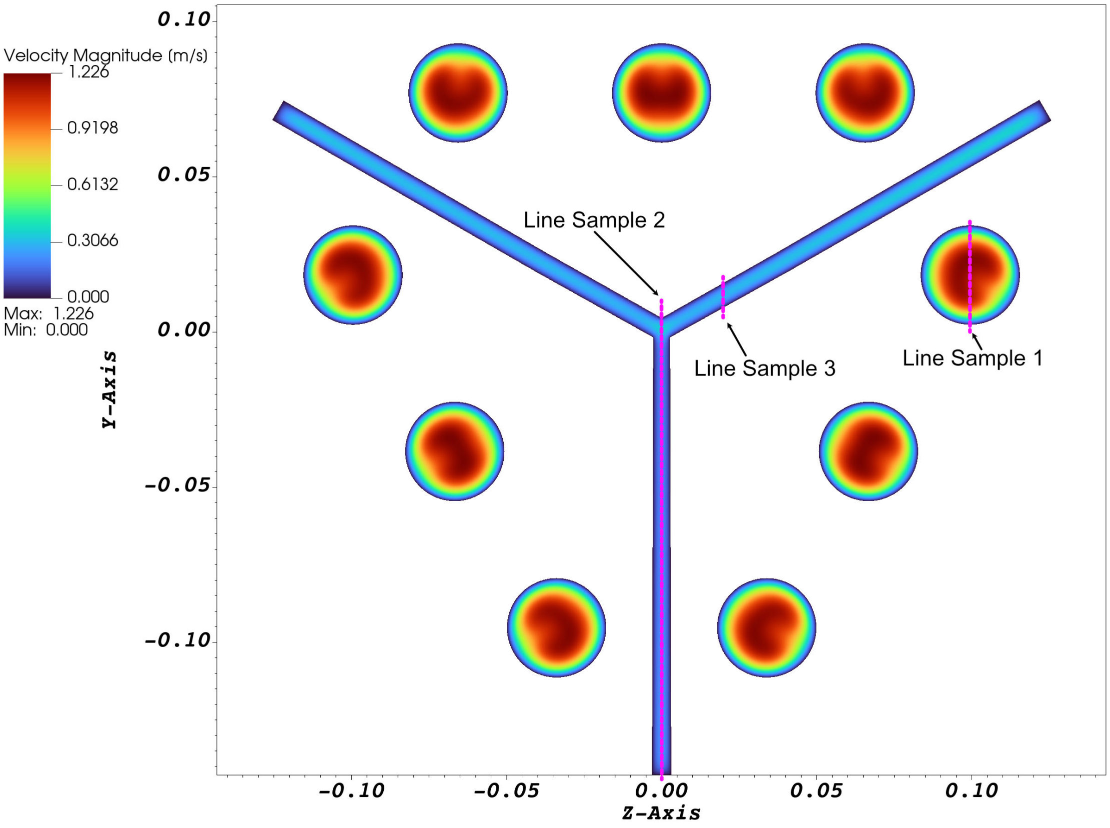

Figure 46. Visualization of the flow velocity in the upper sampling plane from NekRS at the lowest mass flow rate of the INL MIR facility. PIV line sampling locations are shown in pink.

4.2. INL MIR Results

Simulations were performed on the Windriver high-performance computing cluster at INL. NekRS simulations were performed on roughly 11,000 CPU cores. Time averaging of the LES results occurred for roughly three flow-throughs in order to ensure a statistically converged solution. It should be noted that the following results are preliminary, and may be subject to change after analyzing mesh convergence or other sensitivities.

The LES instantaneous flow field for the three flow rates is visualized in Figure 47. Several observations can be made from this figure. Firstly, the three flow regimes align with the observations made in the experiment; in other words, the flow should be laminar, transitional, and turbulent in the coolant channels for each of the three flow regimes, respectively. It should be noted that these flow regimes in the LES are sensitive to the inclusion of a small fillet at the entrance of the coolant channels. If no fillet is included, it was observed that the flow in the lower flow rate exhibited unsteadiness for roughly the first third of the coolant channel length. Including a small fillet with a radius of only 0.5 mm removed this unsteadiness. This is a classic problem in CFD, where the assumption of a perfectly sharp corner can largely influence recirculation and pressure changes near the flow contraction. This is particularly impactful for the INL MIR facility, as the flow rates are near the transitional regime and are extremely sensitive to any small differences in recirculation and turbulent production. The actual roundness of the corners at the entrances of the coolant channels is unknown, and the 0.5 mm fillet radius is an assumption for this work.

4.2.1. Bypass Flow Comparison

The percentage of bypass flow was determined from the LES and RANS models by determining the mass flow rate through each of the nine channels and through the bypass gap. The ratio between the gap mass flow rate and the total mass flow rate was then calculated. The resulting bypass ratios from LES, RANS, and the experiment are shown in Figure 48. LES achieves better agreement with the experimental data than the RANS does, falling within 1% of the experimental bypass ratio at all three flow rates. Additionally, LES appears to follow the trend of the bypass flow as a function of the total flow rate more closely than RANS does. RANS overpredicts the bypass ratio at the lowest flow rate, but underpredicts at the highest flow rate. LES, on the other hand, more consistently tended to overpredict the bypass flow in both the upper and lower regions. A summary of the bypass flow ratio error is given in Table 16. The error in the LES-predicted bypass flow is roughly half that in the RANS predictions. Both simulations saw higher maximum and average errors in the lower region after the redistribution in the horizontal gap. The horizontal gap had a designed width of 2.02 mm. As-built measurements were not provided for this gap width, and it is possible that the as-built width slightly differs from the designed width, as was observed with the vertical gap. Regardless, both the LES and RANS simulations predicted the bypass flow ratio to within 2% of the experimental measurement.

4.2.2. Flow Field Comparison

In addition to measurements of the bypass flow, several line samples of the fluid velocity were measured in the experiment. The locations of these line samples were shown in Figure 46. One line sample was taken through the midpoint of a cylindrical coolant channel, and two line samples were taken within the bypass gap.

Table 16. Summary of LES and RANS bypass flow ratio error $\gamma_{sim} - \gamma_{exp}$ in the INL MIR facility.

	LES			RANS		
	Min	Max	Avg	Min	Max	Avg
Upper	-0.19	0.78	0.56	0.36	2.1	1.16
Lower	0.80	0.93	0.88	1.11	2.55	1.75

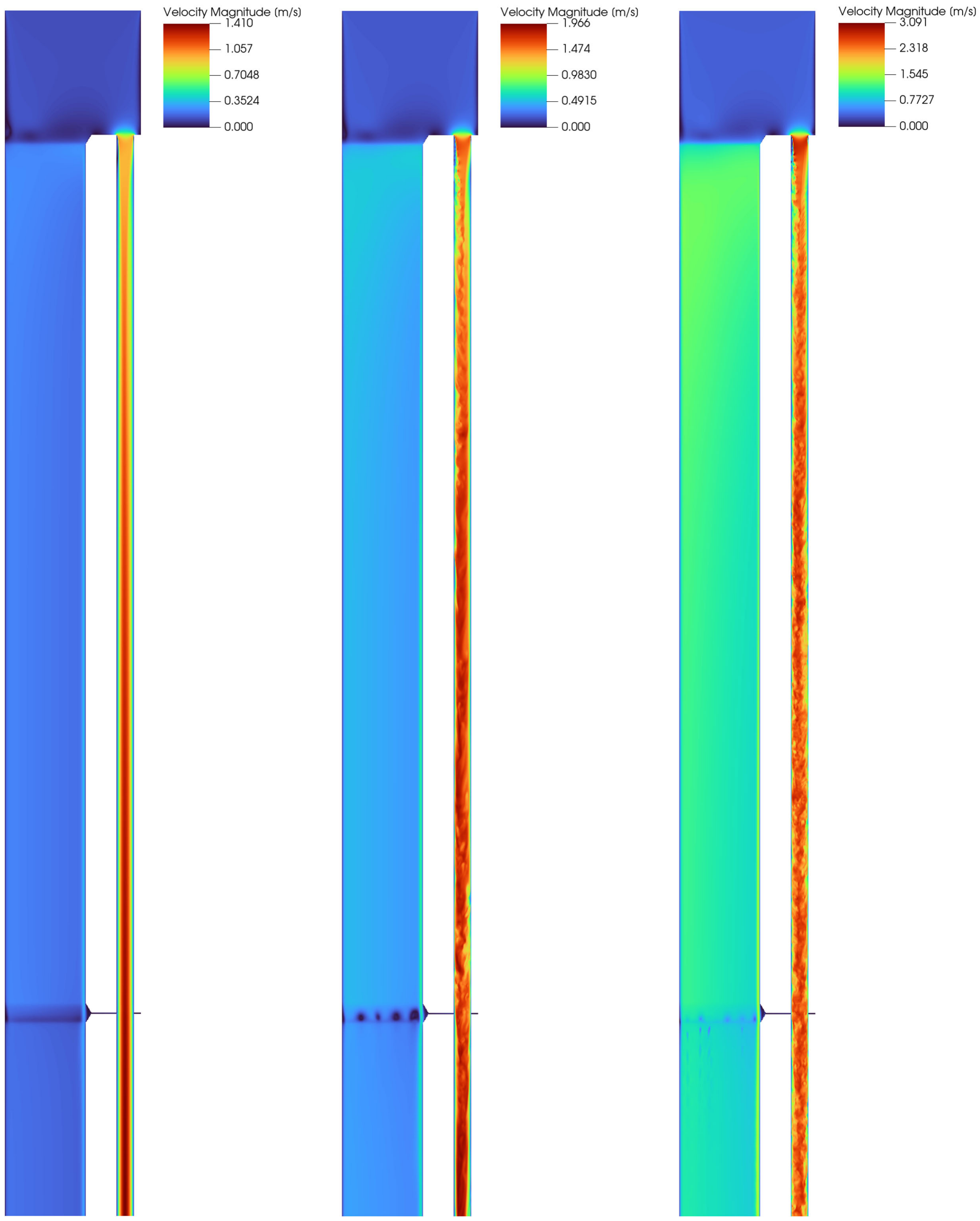

Low VFR Mid VFR High VFR

Figure 47. Instantaneous velocity fields for the LES simulation of the low, middle, and high flow rates in the INL MIR facility.

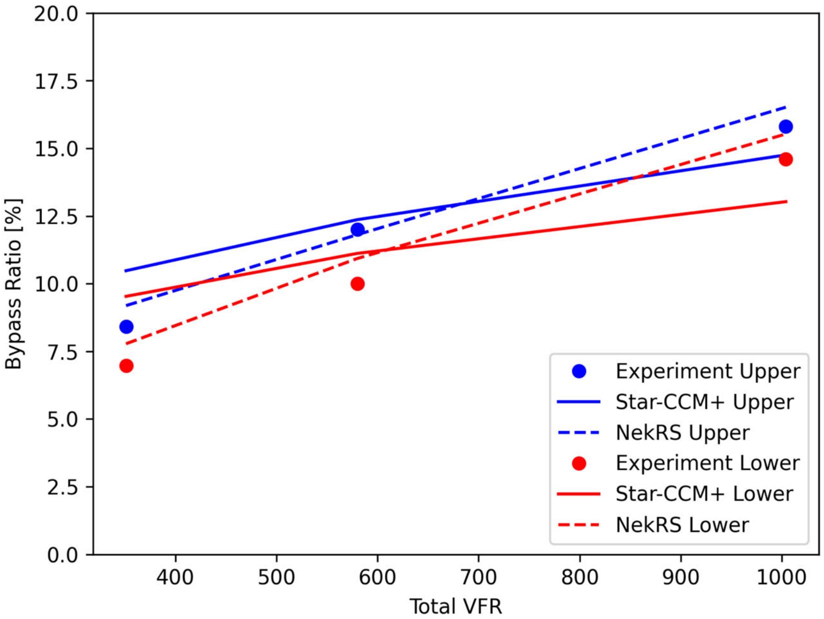

Figure 48. Bypass flow ratio (%) in the upper and lower sections of the geometry measured in the INL MIR experiment, and predicted by the LES and RANS models as a function of total flow rate.

A channel velocity comparison between the experiment, LES, and RANS is shown in Figure 49. The RANS model sees generally good agreement with the experimental data at all three flow rates. Better agreement is observed at the highest flow rate than at the middle flow rate. This is expected, as the middle flow rate falls within the transitional flow regime. In this regime, any small differences between the experiment and simulation geometry or conditions can impact the amount of turbulence, severely altering the comparison. Additionally, RANS models are typically expected to perform the best in fully turbulent flow regimes, and are not usually applied to transitional flow. Nonetheless, the agreement between the experimental data and RANS model is still acceptable at this flow rate. Also of note is the fact that the experimental velocity profile at the middle flow rate appears to be shifted slightly in the +y direction as compared to the experimental data at the other two flow rates. This is likely a result of simple measurement error, as the uncertainty associated with PIV has been observed to result in slightly shifted profiles and boundaries [53]. The LES data in Figure 49 sees even better agreement with the experimental data. Still, some oddities remain. The velocity profiles in the LES appear to be non-symmetric, with a small hump just past the middle of the channel. This appears to be caused by a non-uniformity in the recirculation at the flow contraction at the start of the coolant channels. This is visible in Figure 47, where the proximity of the wall on the right side of the channels is likely influencing the channel entrance effects, causing a noticeably smaller flow recirculation region on the side of the channel closest to the wall. Further down in the streamwise direction, this asymmetry goes away as the flow redistributes in the LES. The RANS model appears to redistribute the asymmetry much faster, as a small asymmetry exists at the entrance of the channel but is no longer observed in the sampling lines in Figure 49. This asymmetry does appear to exist in the experimental data at the highest flow rate, as the geometric center of the channel is around y = 14 mm, but the peak in the velocity occurs at around y = 16 mm. This is in good agreement with the LES data, where the peak is near y = 17 mm. However, the asymmetric velocity profile does not appear in experimental measurements at the middle and low flow rates.

Second-order statistics were also measured for the flow in the coolant channels at the fully turbulent flow

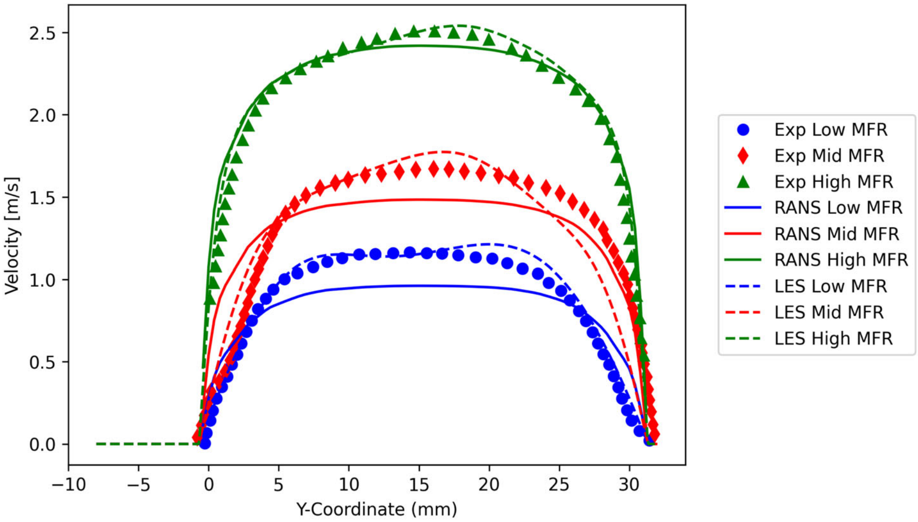

Figure 49. Velocity profile through channel F (line sample 1) in the INL MIR experiment, RANS, and LES.

rate of 1004.1 gal/min. The experimental data reported the turbulent intensity in each of the nine channels. For the sake of brevity, only channel F is shown, as all nine channels exhibit similar behavior. The turbulent intensity for channel F is shown in Figure 50. Both the LES and RANS models accurately predict the turbulent intensity. As was seen in the velocity in Figure 49, an asymmetry is present in the LES result, due to the proximity of the channel to the inlet plenum wall. This asymmetry may exist in the experimental data as well, given the measurement at around y = 21 mm, though it is hard to discern whether this dip in the experimental data is physical or rather a result of measurement noise. Nonetheless, it can be seen that both models are capable of accurately reproducing the turbulent intensity in the flow channels.

Figure 51 compares the velocity magnitude in the center of the gap, line sample 2. Several key takeaways can be made from this plot. First, it can be seen that both the RANS and LES agree well with the experimental data at the lowest flow rate, but significantly underestimate the predicted velocity magnitude at the middle and high flow rates. LES does see significantly better agreement at the highest flow rate, but the velocity underestimation is still significant. There could be a number of reasons for this discrepancy, the most likely being that the gap size may not be constant along the axial length of the domain. Measurements of the actual gap size were taken, but no information was provided on where these measurements were performed. Given that the gap wall plates in the experiment are roughly 1.5 m long and about 10 mm thick, it is reasonable to assume there may have been some bending or twisting of the plates along the axial length of the gap if everything was not perfectly aligned. Even small deviations of less than 1 mm could significantly impact the gap flow rate. The profiles for both the LES and RANS models do exhibit trends of good agreement with the experimental data, with the velocity being higher near y = -125 mm where the gap size is largest, then reducing in the +y direction as the gap size narrows. In the large opening at the center of the bypass gap, there is then a large increase in the flow velocity. These trends are reproduced well in both CFD models.

This suspicion of non-uniform gap size can be further strengthened by examining the velocity profiles across the right gap, line sample 3, in Figure 52. The LES simulation agrees very well with the experimental data for this line sample location at all three flow rates. The RANS model sees worse-but-acceptable agreement with the data. By examining the location of the line samples in Figure 44 and the measured sizes of the gaps in Figure 46, we see that the gap width in line sample 3 should be roughly 7 mm, and that the gap width in line sample 2 should vary from 6.2 to 5.47 mm. The smaller flow area of the gap in line sample 2 should make it more resistive to flow, and one would expect that the flow velocity in line sample 2 is lower than in

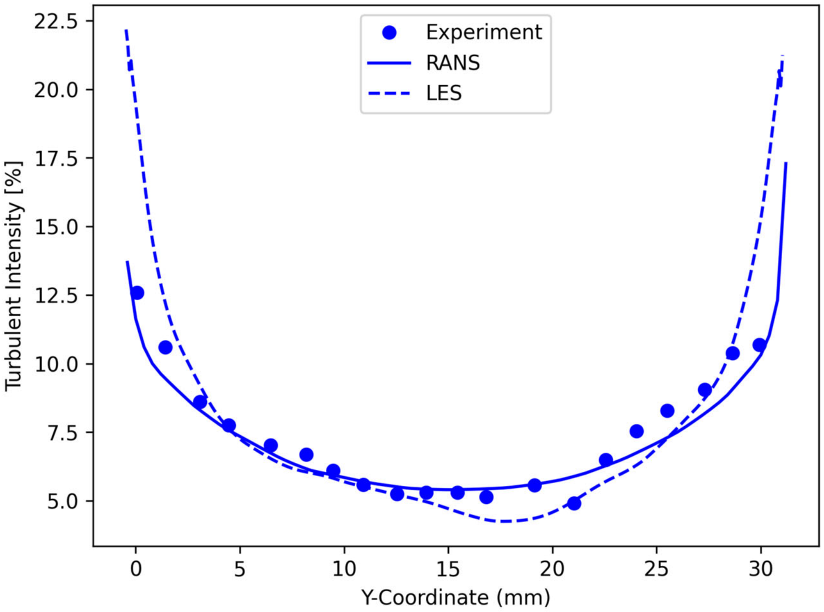

Figure 50. Turbulent intensity in Channel F (line sample 1) in the INL MIR experiment, RANS, and LES.

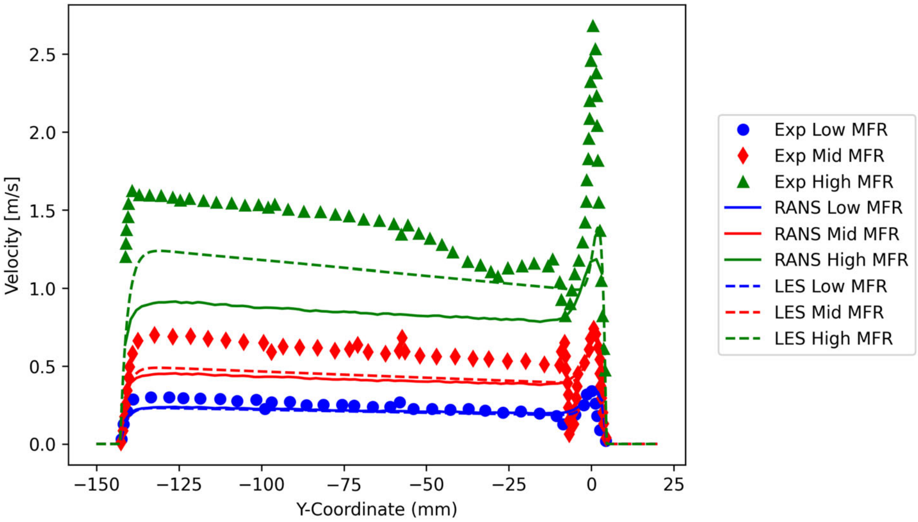

Figure 51. Velocity magnitude in the center of the middle vertical gap (line sample 2) in the INL MIR experiment, RANS, and LES.

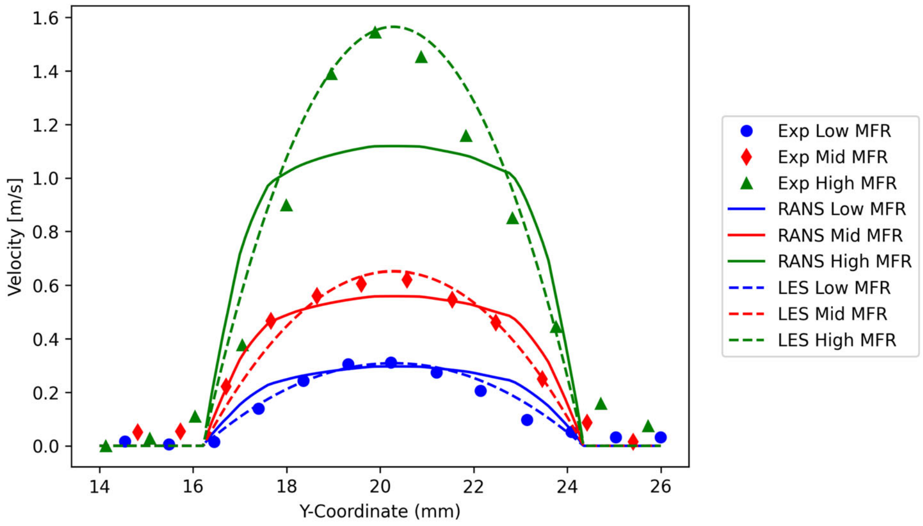

Figure 52. Velocity magnitude in the right vertical gap (line sample 3) in the INL MIR experiment, RANS, and LES.

line sample 3. This intuition aligns with the data produced by both CFD models, as the maximum velocity for the highest flow rate in line sample 3 is roughly 1.6 m/s, while the maximum velocity in line sample 2 is around 1.2 m/s. For the experimental data, however, the maximum velocity is actually higher in line sample 2 than line sample 3. This misalignment with basic intuition further reinforces the idea that there is perhaps either an error in the experimental gap size measurement of the gap in which line sample 2 is located, or that the gap size in the experiment was perhaps not axially constant along the domain.

4.2.3. Pressure Drop

A comparison of the pressure drop between the inlet plenum and horizontal gap is shown in Figure 53. LES performs better than the RANS model does at all three flow rates, and is within the experimental uncertainty band for the lowest and highest flow rates. RANS tends to overestimate the pressure drop in all three cases. Future investigation can be performed to determine the sensitivity of this result to the turbulence model applied. Neither of the two models manages to fall within the experimental uncertainty for the middle flow rate, however. This can be mainly attributed to the fact that this flow rate falls into a transitional regime in the coolant channels. Any small geometric, surface roughness, or flow rate inconsistencies between the models and the experiment can lead to significant differences in the amount of unsteadiness in the flow, potentially having a large impact on the pressure drop. It is worth noting that the turbulent kinetic energy in the transitional flow case is heavily impacted by the treatment of the corners at the inlet of the flow channels. The fact that initial efforts treated these as sharp corners significantly increased the amount of TKE production, making the middle flow rate case significantly more turbulent. This also caused significant unsteadiness in the lowest flow rate, which the experimentalists had reported to be laminar. Including a small fillet with a 0.5 mm radius on the corner between the inlet plenum and coolant channels significantly changed the resulting flow field in the LES simulation, making the lowest flow rate case laminar and significantly reducing the turbulence at the middle flow rate. This sharp-corner phenomenon is a classic issue encountered in CFD modeling, and it is important to note that it significantly impacts the resulting flow field for this geometry.

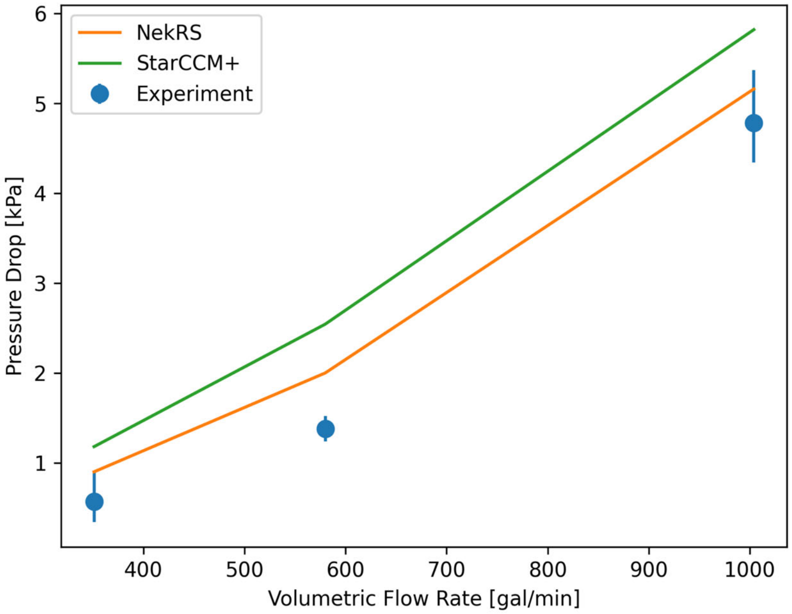

Figure 53. Pressure drop between the inlet plenum and horizontal gap, as compared between the INL MIR experiment, RANS, and LES simulations.

4.3. KAERI Facility

A series of experimental bypass studies were performed by SNU and KAERI related to prismatic HTGRs [54]. The first in this series was the unit cell experiment at SNU. The unit cell was comprised of three neighboring hexagonal fuel assemblies/moderator blocks, as shown in Figure 54. This experiment focused on the flow split between the coolant channels and the bypass between the assemblies by measuring the mass flow rate through each area. The unit cell consisted of only one layer of fuel assemblies/moderator blocks; therefore, cross flow in the interfacial gaps between stacked assemblies was not considered.

The unit cell test facility was 7.75 m long and 1.4 m wide and consisted of a flow control system, test section, data acquisition system, and measuring system, as shown in Figure 55. The flow control system used a wind tunnel to supply a uniform flow distribution to the test section, and a blower to provide the flow rate and pressure head. A bi-directional flow tube flow meter was located at the inlet of the blower to measure the inlet flow rate. The air inlet mass flow rate in the unit-cell experiment ranges from 0.0825 to $0.5802\,kg/s$, corresponding to Reynolds numbers in the coolant hole and bypass gap between 10^3 and 10^4. A full description of the test cases can be found in Reference [54].

The test section was 0.793 m long, with an equilateral triangle cross-section of side length 0.427 m. The test section consisted of three test blocks that could represent either fuel assemblies or moderator blocks. Three configurations were tested: one fuel assembly and two moderator blocks (F1), two fuel assemblies and one moderator block (F2), and three fuel assemblies (F3). The moderator blocks did not have any coolant channels, meaning no air flow passed through those regions. Each fuel assembly test block consisted of two smaller coolant channels (12.6 mm in diameter) and 21 larger coolant channels (16 mm in diameter). The geometry of a fuel assembly test block is described in Figure 54. An important note is that the whole bypass gap is shown in Figure 54. For a true one-third representation, half the bypass gap width should be considered.

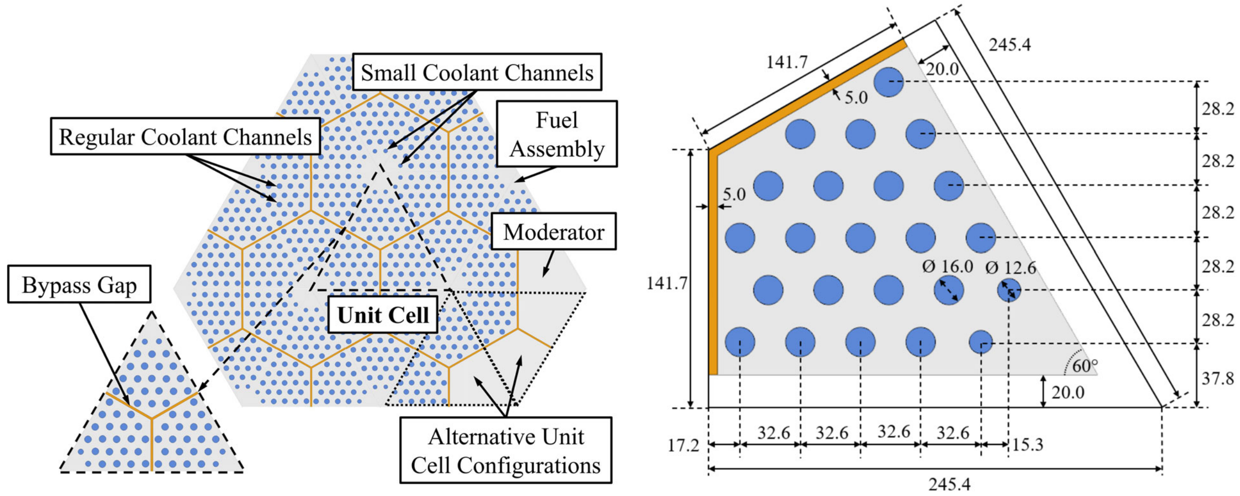

Figure 54. (Left) Example unit cell comprised of three neighboring fuel assemblies. (Right) Test block dimensions.

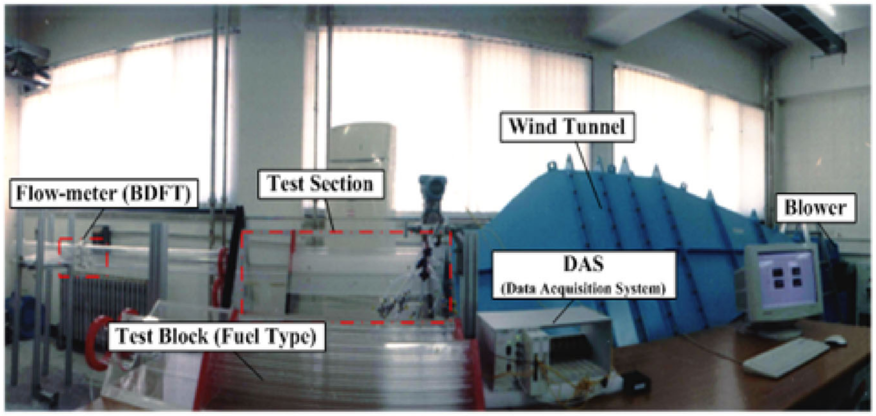

Figure 55. SNU experimental test facility.

The bypass gap is located between the test blocks and was maintained using gap control blocks. Three different bypass gap sizes were tested: 1 mm (G1), 3 mm (G3), and 5 mm (G5). Errors in maintaining the 1 mm gap size were reported by experimentalists while running the tests. Bi-directional flow tubes were located at the end of each channel’s test section to measure the mean velocity in order to obtain the mass flow rate. The bypass flow could then be determined by measuring the difference between the inlet mass flow rate and the mass flow rate in the three outlet tubes. The test section was horizontal due to negligible gravitational effects, and used air at standard atmospheric temperature and pressure. Each gap size and configuration setup were run with three varying inlet mass flow rates: a low mass flow rate (W1), an intermediate mass flow rate (W2), and a high mass flow rate (W3). A summary of the test matrix is provided in Table 17.

Table 17. SNU test matrix with varying gap size (G), configuration (F), and inlet mass flow (W). Reference [54] provides a full description of the flow conditions for this test matrix.

	Gap 1 mm (G1)	**Gap 3 mm (G3)**	**Gap 5 mm (G5)**
F1 (One fuel assembly)	G1F1W1	G3F1W1	G5F1W1
	G1F1W2	G3F1W2	G5F1W2
	G1F1W3	G3F1W3	G5F1W3
F2 (Two fuel assemblies)	G1F2W1	G3F2W1	G5F2W1
	G1F2W2	G3F2W2	G5F2W2
	G1F2W3	G3F2W3	G5F2W3
F3 (Three fuel assemblies)	G1F3W1	G3F3W1	G5F3W1
	G1F3W2	G3F3W2	G5F3W2
	G1F3W3	G3F3W3	G5F3W3

4.3.1. KAERI RANS Modeling

3D RANS simulations were conducted using the $k - \omega$ SST model in STAR-CCM+. Air flow through the domains was modeled as steady-state, isothermal, segregated flow. The thermophysical properties of the air were set to match the recorded values in the experimental tests, where $\rho = 1.18415$ kg/m^3 and $\mu = 1.85508 \times 10^{-5}$ Pa-s. The different geometry regions and boundary conditions are shown in Figure 56.

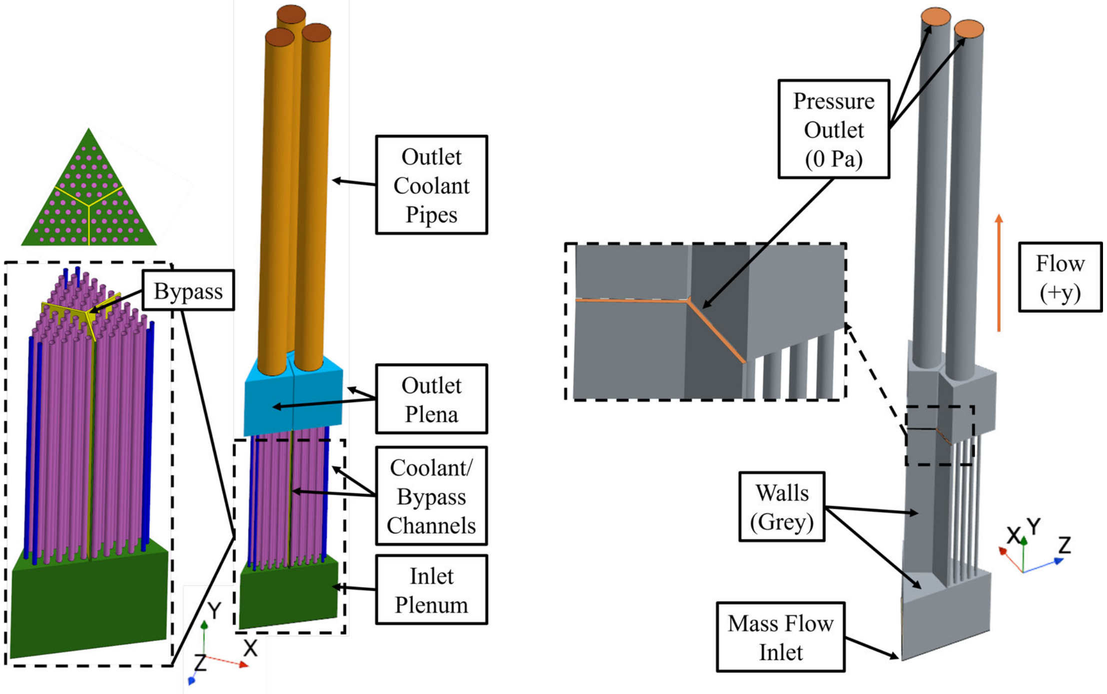

a) Various Geometry Components

b) Boundary Conditions

Figure 56. (a) Geometry components within the fluid domain, and (b) boundary conditions for the simulations of the KAERI unit cell experiment.

Flow enters a unified inlet plenum (green) where the inlet mass flow rate is set according to the experimental value. The inlet plenum is 0.3 m long and has an equilateral triangle cross-section of side length 0.416 m. The inlet plenum leads to three regions of coolant channels (dark blue/magenta) and the bypass gap (yellow). The small coolant channels (dark blue) have a diameter of 12.6 mm and the regular coolant channels (magenta) have a diameter of 16.0 mm. Both sets of coolant channels are 0.753 m long. The three regions of coolant channels (23 coolant channels in each region) outlet to three separate outlet plena (cyan). The outlet plena is 0.3 m long and has an equivalent cross-section to the inlet plenum, with the exception of the bypass area being removed. The outlet plena then lead to coolant pipes (orange) that outlet to atmosphere. The outlet coolant pipes are 1.8 m long. The bypass has its own separate outlet that outlets to atmosphere at the end of the test section (0.752 m). The bypass channel was made 1 mm shorter than the coolant channels to avoid Boolean errors where the two geometries would have contacted. The coolant channels, plena, bypass, and outlet pipe walls were all set to no-slip wall boundary conditions.

Two different geometric independent parameters were modeled in STAR-CCM+: the bypass gap width and the configuration. The three bypass gap widths modeled are shown in Figure 57, and are consistent with those used in the experimental studies. The three different configurations considered are shown in Figure 58. The F1 configuration represents an area of the core consisting of one fuel assembly and two neighboring moderator blocks (reference Figure 54). Flow does not pass through the moderator blocks, so the inlet plenum leads to two walls where the moderator blocks are, and all the flow goes into one region of coolant channels and the bypass channel. The F2 configuration represents two neighboring fuel assemblies and one moderator block, with only one region being blocked off to air flow. Lastly, the F3 configuration consists of three neighboring fuel assemblies where flow can pass through coolant channels in all three regions.

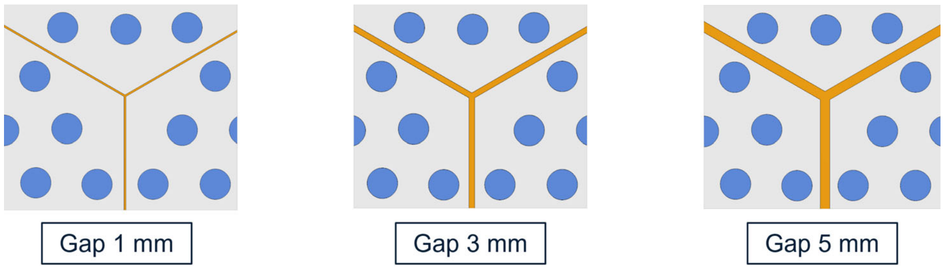

Figure 57. Varying bypass gap widths modeled in STAR-CCM+ for the KAERI unit cell facility.

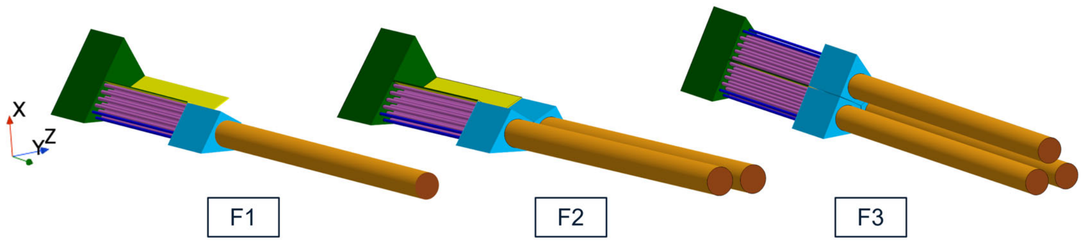

Figure 58. Varying unit cell configurations modeled in STAR-CCM+ for the KAERI unit cell facility.

The meshes for the different cases were created using the automated mesh feature in STAR-CCM+. The meshes consisted of polyhedral elements of base size 4 mm. Near-wall boundary layers were added by using the prism layer feature with 7 prism layers and a 1.5 progression. An example mesh is shown in Figure 59. The total element counts, which varied with the number of fuel assemblies modeled, were as follows: 5,928,434 elements for F1, 10,636,402 elements for F2, and 15,361,068 elements for F3. The cases were wall-resolved, and all the meshes satisfied $y^{+}_{max} < 1$ accordingly. A mesh refinement study was carried out by varying the base element size from 1 to 2 to 4 mm and then monitoring the global pressure drop.

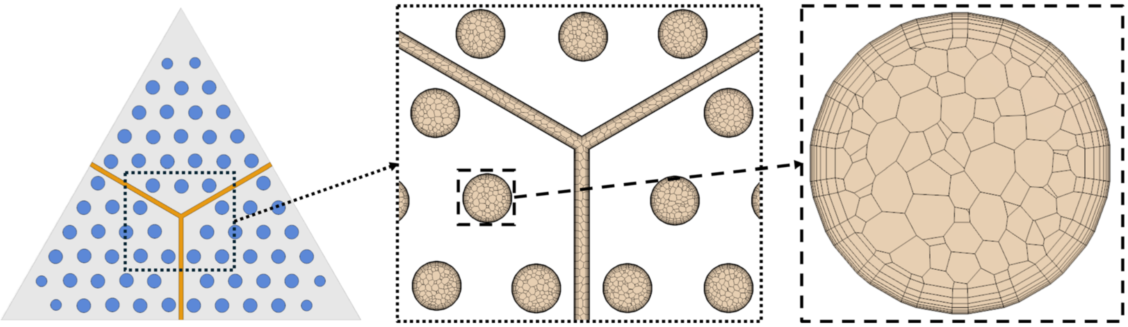

Figure 59. Example mesh section showing the coolant channel and bypass discretizations in STAR-CCM+ for the KAERI unit cell facility.

4.3.2. KAERI LES Modeling

LES was performed using NekRS. The meshes for LES were created using the open-source meshing tool Gmsh [55]. Due to the nature of the geometry, a singular conformal all-hexahedral mesh was not achievable across the whole domain. The limiting factor is that the blocking for the individual coolant channels would need to propagate through not only the outlet plena, but also the outlet coolant pipes as well. A conformal, structured hexahedral mesh is required for NekRS; therefore, the geometry was split into two parts that were each meshed separately to satisfy this requirement.

The first part, referred to as the inlet region, consists of the inlet plenum, coolant channels and bypass channel, and outlet plena. The blocking for the inlet plenum, coolant channels, and bypass channel is shown in Figure 60.

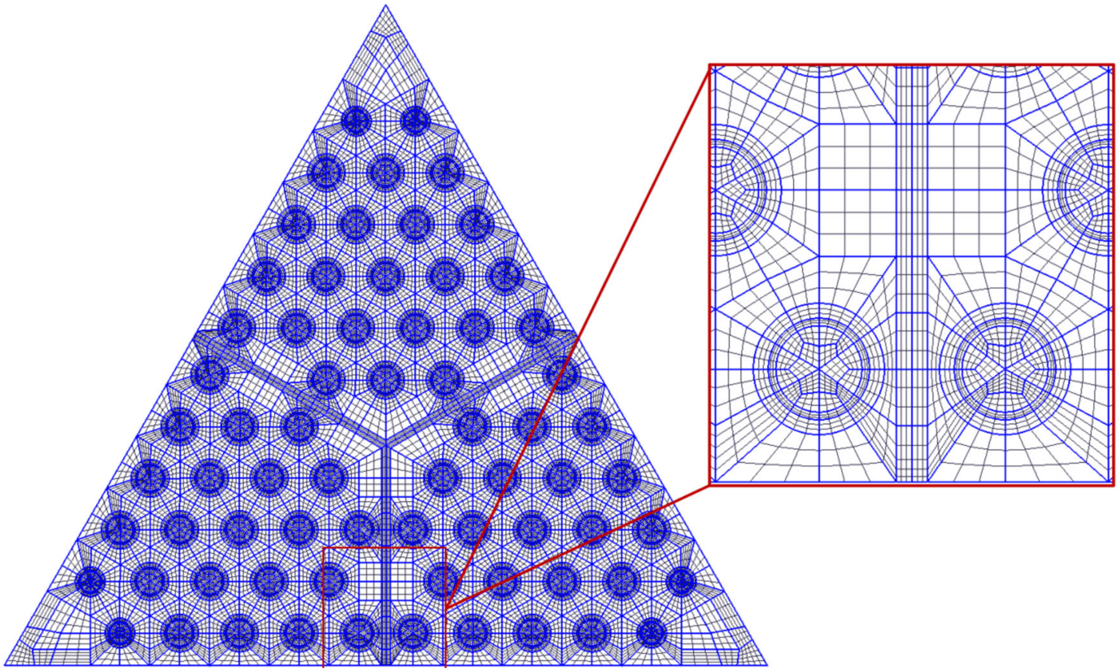

Figure 60. Inlet plenum, coolant channels, and bypass gap for LES cases of the KAERI unit cell facility.

The second part, referred to as the outlet region, consists of a portion of the outlet plena that overlaps with the inlet region as well as the outlet coolant pipes. The blocking for the outlet plena for the inlet region versus the outlet region is shown in Figure 61. The blocking varies greatly between the two outlet plenum meshes, and is largely driven by near-wall requirements in different regions—requirements that must be propagated through the whole domain to keep the mesh conformal. The base meshes were provided by Gmsh, then further discretized according to the polynomial order specified in NekRS. The NekRS discretization applied a progression toward the element boundaries in all directions, adding increased refinement in near-wall regions.

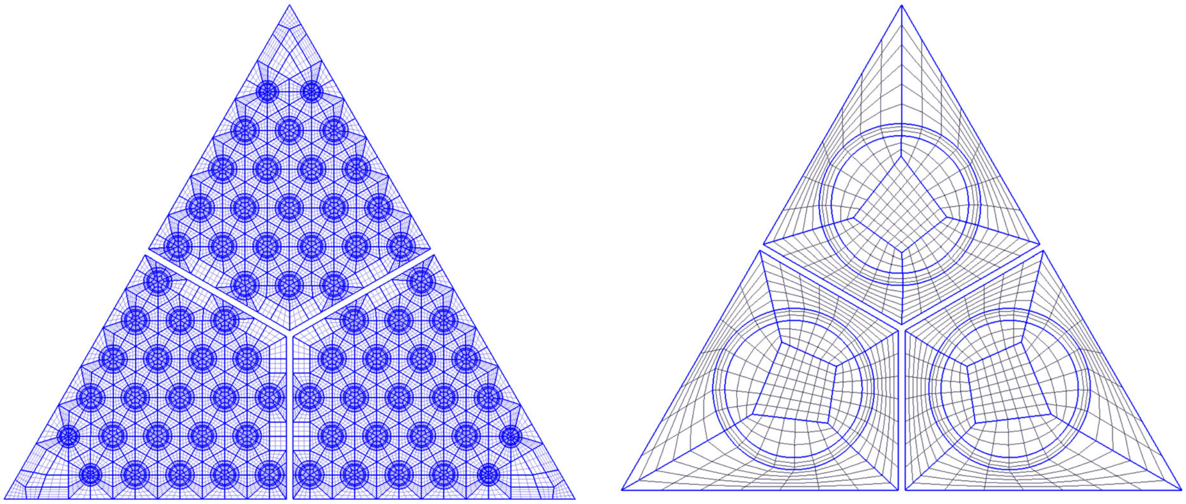

Figure 61. Outlet plena mesh for LES cases in the inlet domain (left) and the outlet domain (right) for the KAERI unit cell facility.

The domains were coupled using the native NekRS solver NekNek for overlapping domains. NekNek performs Schwarz iterations for the overlapping regions and interpolates the solution to the nearest nodal point. This couples the simultaneous solutions in the domains and allows for runtime transfer [56]. A larger overlap region aids in the stability of the coupled solver but increases the computational cost of the simulation. An axial slice of the overlap region between the two domains is shown in Figure 62.

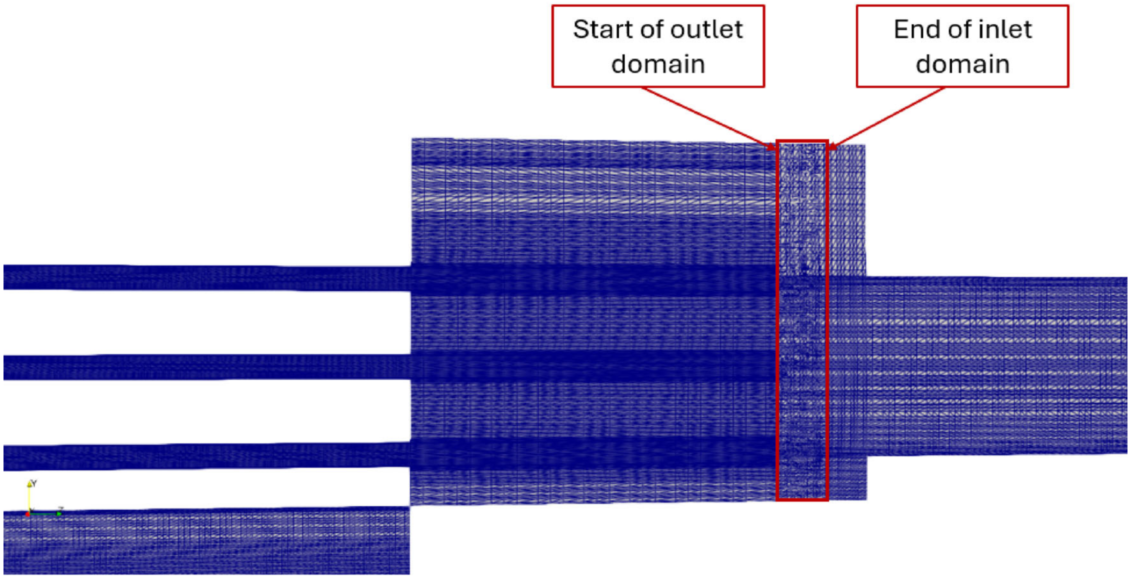

Figure 62. Overlap region between the inlet and outlet domains for the KAERI unit cell facility.

4.4. KAERI Results

The bypass split between the coolant channels and the bypass channel was determined by measuring the mass flow rate in each region and calculating the ratio of mass flow in the bypass versus the entire domain. Figure 63 shows the results for all 27 RANS cases in comparison to the experimental data from SNU/KAERI. Overall, the RANS cases showed decent agreement with the experimental data. However, the RANS models struggled to capture certain areas of the bypass split more than others.

Starting with the top-left plot in Figure 63, the RANS models deviated most from the experimental data for the larger gap sizes in the F1 configuration. As the gap size increases, so does the Reynolds number in the bypass channel. This causes greater entrance effects at the start of the coolant channels, thus leading to larger discrepancies between RANS predictions and experimental results. Such discrepancies clearly decrease while increasing the flow conditions (i.e., varying cases from W1 to W3). This trend may be potentially explained since friction losses becomes progressively larger compared to local effects, thus improving RANS predictions. All other cases involving smaller gap sizes in the F1 configuration provides general good agreement when comparing RANS results with the experimental data.

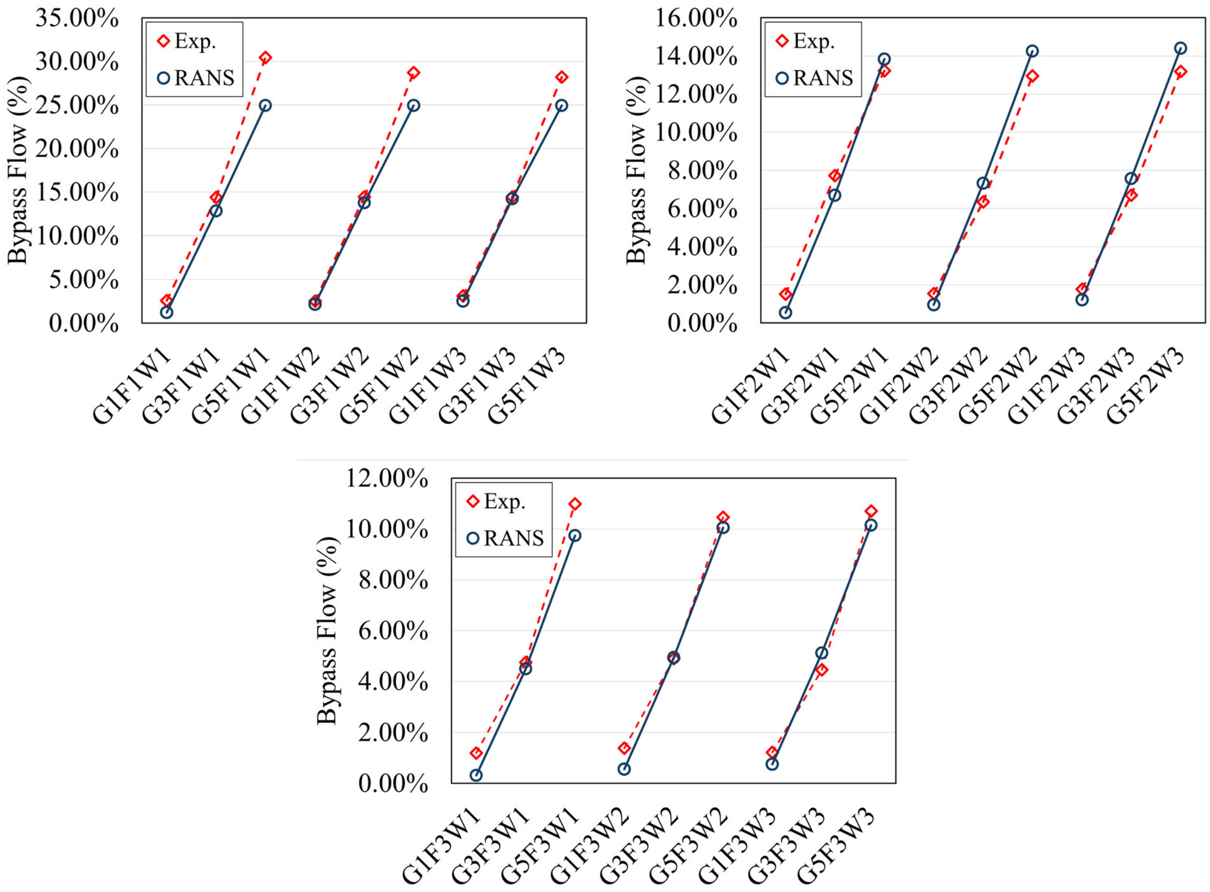

Figure 63. Bypass flow results as compared to the SNU experimental values for F1 (top left), F2 (top right), and F3 (bottom).

Moving to the top-right plot in Figure 63, RANS compared well overall for the F2 configuration. RANS slightly overpredicted the bypass flow for the larger gap sizes and underpredicted the bypass flow for the smaller gap size. Lastly, in the bottom plot of Figure 63, RANS again showed good agreement across the F3 configuration cases. RANS underpredicted the bypass flow for the smallest gap size, just as it did before; however, it also slightly underpredicted the bypass flow for the largest gap size.

Figure 64 shows velocity profiles at 0.1 m into the coolant channel inlets considering the bypass and three coolant channels. Velocity profiles are shown for the three block configurations with a gap size of 5 mm and with lower inlet mass flow rates (i.e., G5F1W1, G5F2W1, and G5F3W1 cases – see Table 17). The sampling line is displayed on the left of Figure 64 and is the same for the three selected reference cases. It is important to note that all three cases have increasing inlet mass flow rates when going from F1 to F3. All cases exhibit asymmetries in the coolant channel velocity profiles to varying degrees. These asymmetries are largely attributed to entrance effects, as the sampling lines are located roughly six diameters downstream from the inlet of the coolant channels. Two observations are noteworthy. First, the asymmetries become increasingly pronounced as the mass flow rates increases. This effect is expected due to stronger flow contractions and redistribution as the flow enters the coolant channels. Second, the velocity peaks—particularly in off-center coolant channels—tend to shift toward the center of the block. This effect is potentially explained by the pressure distribution within the inlet plenum, where the flow tends to stagnate near the lateral regions.

The velocity profiles in the bypass channel vary significantly across the different block configurations. In particular, configurations F2 and F3 exhibit two distinct peaks located near adjacent coolant channels. Such local velocity surges are explained by the proximity of these channels to the bypass gap, where their inlet dynamic pressure reduces local flow resistance, thereby facilitating the flow entering these portions of the bypass channel. This explanation is further supported by the observation that configuration F3, which lacks any adjacent coolant channels, does not exhibit such peaks.

Additionally, a consistent effect across all configurations is another local velocity surge at the intersection of the three bypass channels. This effect is attributed to the increased flow area at the intersection, which promotes higher velocities due to reduced flow resistance.

Figure 65 presents the same sampling line profiles as previously shown, this time, further downstream – at 0.3765 m from the inlet channel. These present plots are remarkably more symmetric compared to Figure 64, indicating that entrance effects have dissipated while the flow have developed. Similar to the upstream profiles, a local velocity peak is observed in the region where the three bypass gaps intersect, due to the increased flow area at that location.

Lastly, Figure 66 focuses on the flow redistribution within the bypass channel as it evolves along the streamwise direction. Configuration F3 is used as a reference case, as the bypass channel is has neighbor coolant channels in both sides, resulting in more pronounced local flow surges. These local effects dissipates as the flow develops through the channel. Nevertheless, the velocity peak at the intersection of the bypass channels persists. Again, this effect is explained by the increased cross-sectional area at that location.

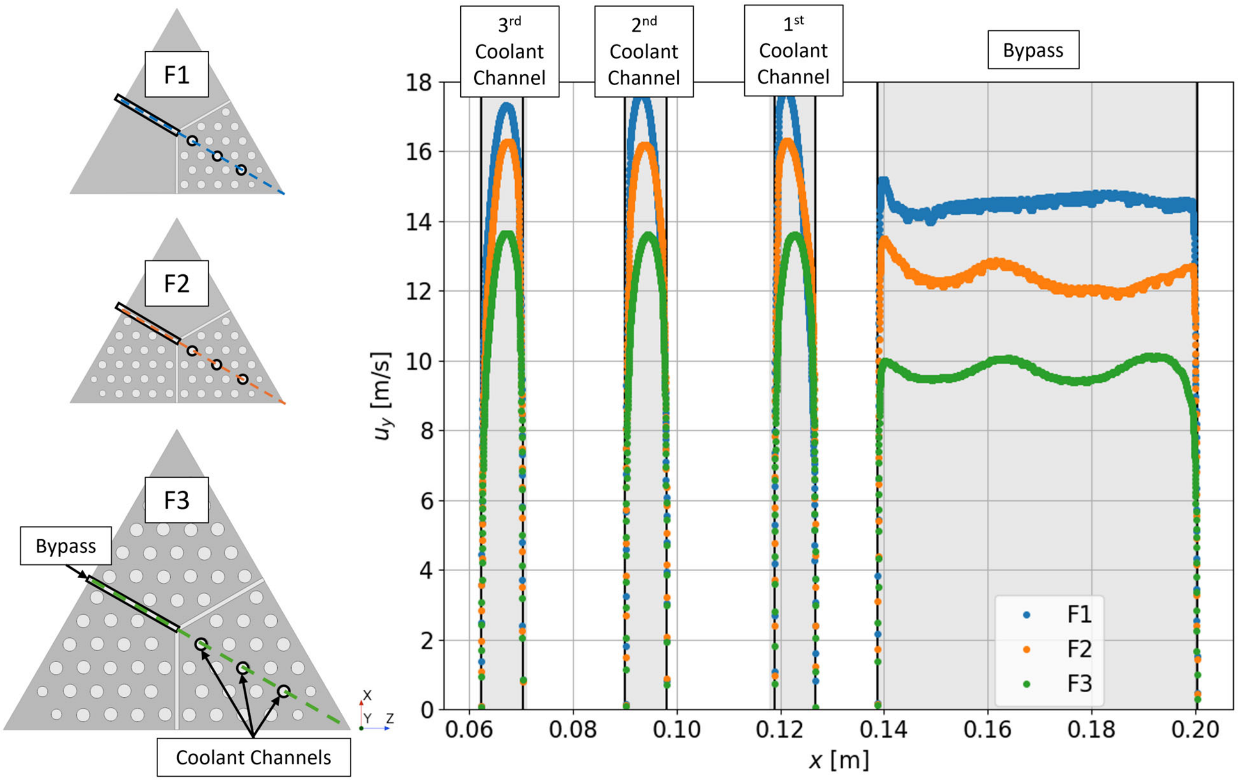

Figure 64. KAERI unit cell facility stream-wise velocity profiles located 0.1 m into the coolant/bypass channels for all three configurations, for a gap size of 5 mm at the lowest flow rates.

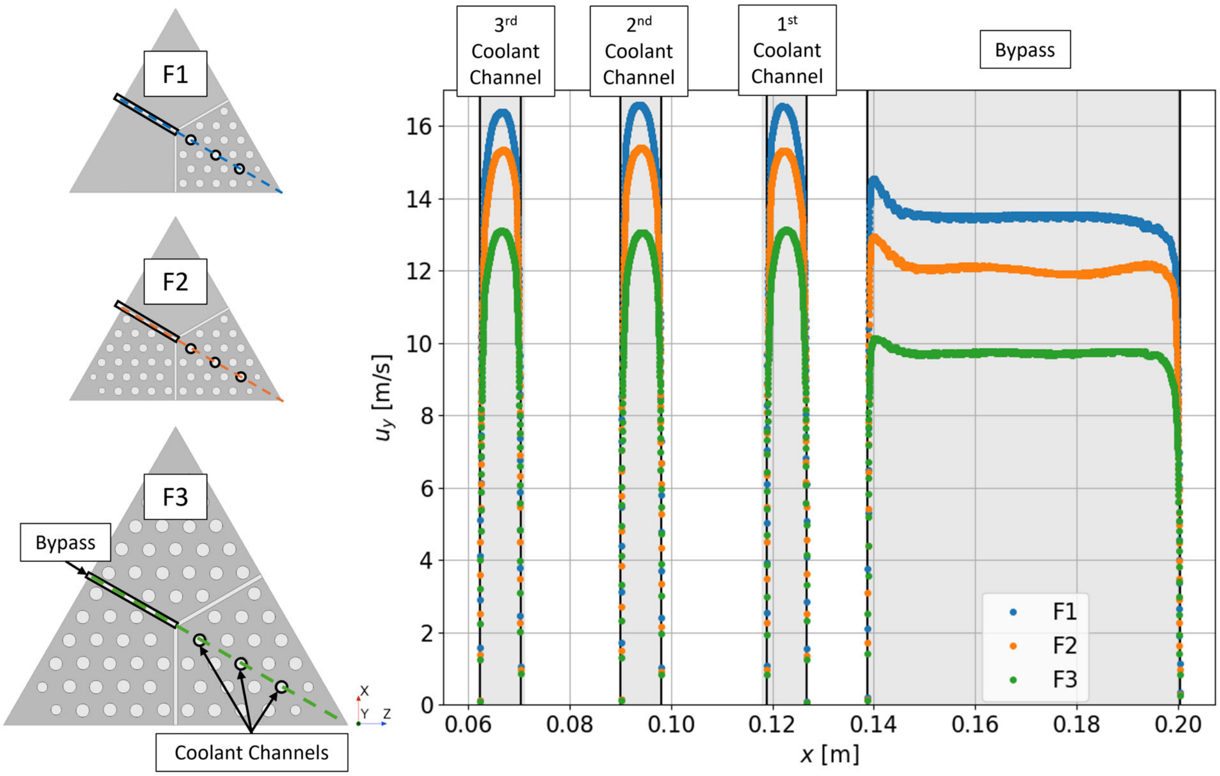

Figure 65. KAERI unit cell facility stream-wise velocity profiles located 0.3765 m into the coolant/bypass channels (midpoint) for all three configurations, for a gap size of 5 mm at the lowest flow rates.

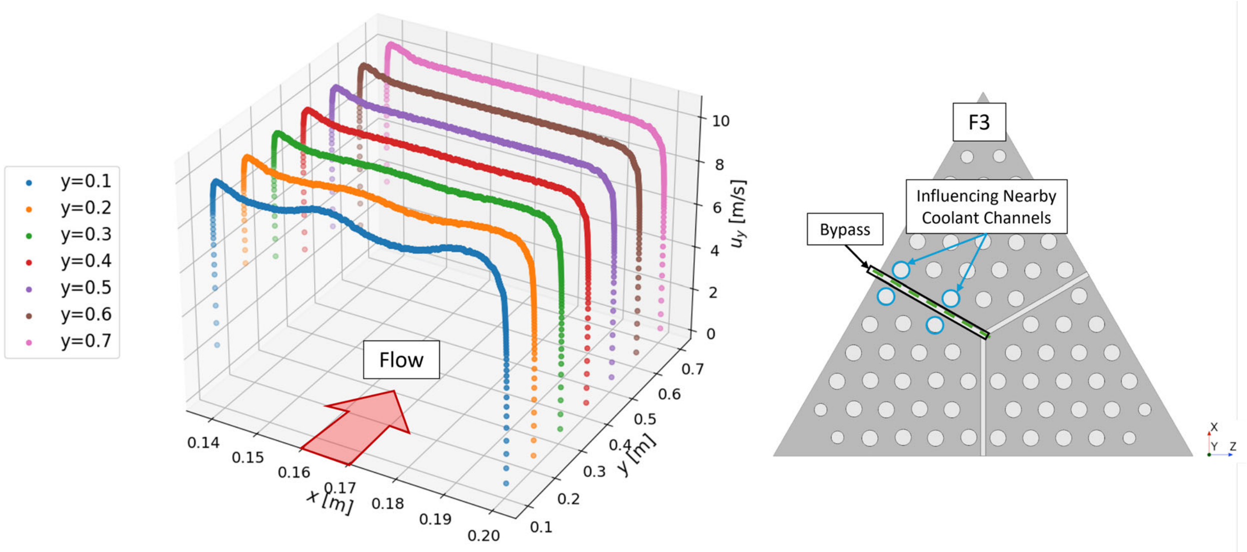

Figure 66. KAERI unit cell facility stream-wise velocity profiles for the G5F3W1 case at different y-positions down the length of the bypass gap.

5. LOWER PLENUM MIXING VALIDATION

Thermal mixing at the outlets of HTGRs is a critical design aspect for both safety and performance. At the core outlet, radial temperature variations can reach magnitudes on the order of $100°C$ [57, 58]. This variation mainly occurs because a portion of the coolant will bypass the core through gaps between the graphite reflector blocks. Poor thermal mixing of these coolant fractions not only deteriorates the heat transfer efficiency in the steam generator but also leads to structural damage due to cyclic thermal loading. Therefore, the lower plenum and its related components are designed to enhance thermal mixing and ensure the efficiency and reliability of HTGRs.

The ART-GCR program is aimed at validating computational tools that are both computationally affordable and accurate. To fulfill its goal, three numerical modeling approaches are employed to characterize and simulate thermal mixing in the lower plena of HTGRs: LES, RANS, and a 2D-RZ axisymmetric porous media model. The adopted models address the full spectrum of fidelity in thermal hydraulics.

The three modeling approaches highlighted will be evaluated with data from a 2:5 scaled experiment of the outlet plenum in the HTR-PM [21]. Validation of these models is performed at different stages of completion, as is discussed herein.

This section is organized as follows. Section 5.1 presents the reference scaled mixing experiments, and sections 5.2 to 5.3 present the current progress made in porous media simulation. RANS work is also being performed, and was detailed in a report from FY-24 [59].

5.1. Lower Plenum Design

The HTR-PM is a gas-cooled PBR currently in operation in China, with two modular reactors working together to drive a single turbine. The Hot-Gas Mixing experiment, shown in Figure 67, is a scaled replica of the HTR-PM lower plenum that was used to analyze mixing in the lower plenum.

This experiment used air as a working fluid. Experiments were performed at a variety of hot and cold gas mass flow rates, and at multiple temperature differences between the hot and cold gas. The experiments considered in this work relied on hot and cold gas entering with a temperature difference equal to 100 K.

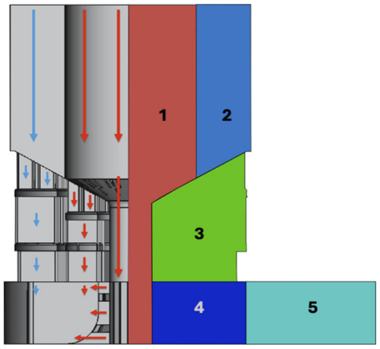

Figure 67. (Left) Hot and cold air coolant paths. (Right) Five distinct regions.

Region 1 represents the hot inlet and the smaller-diameter discharge pipe. Region 2 represents the cold inlet. Region 3 represents the reflector. Region 4 represents the hot-gas mixing chamber, and Region 5 represents the outlet pipe.

5.2. Large Eddy Simulation

This section presents the NekRS model based on the LES methodology of the scaled mixing experiment. The LES model is aimed at characterizing turbulence and turbulent heat in detail. Given the stringent computational requirements involved in LES, the model focuses on key components in which mixing occurs. Figure 68 shows the key regions for promoting thermal mixing. Specifically, 15 gas-mixing channels are designed to collect gases at different temperatures and promote thermal mixing through crossflow. As illustrated in the drawings, the hot gas exiting the core enters each of these channels radially, while cooler gas from the bottom reflector enters from the top. This flow setup promotes complex vortexes that enhance turbulent mixing. Following this intense mixing process, the flow is directed to a mixing chamber, from which it is subsequently discharged toward the outlet pipe.

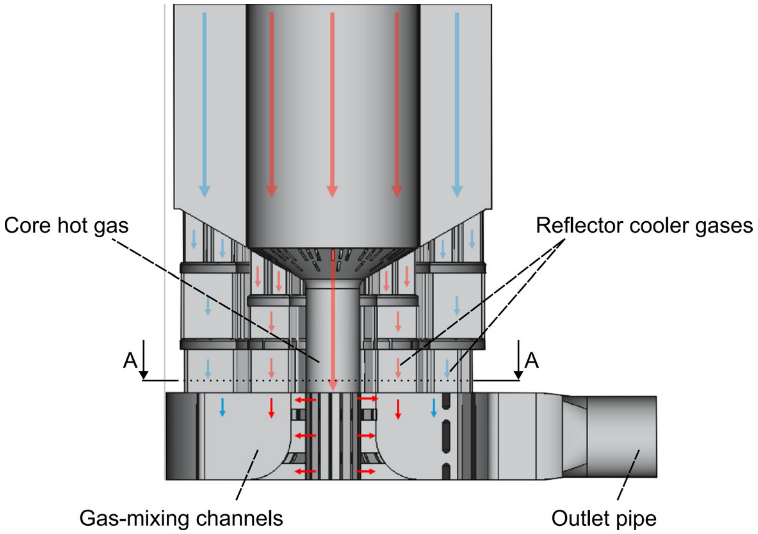

(a) Lateral view.

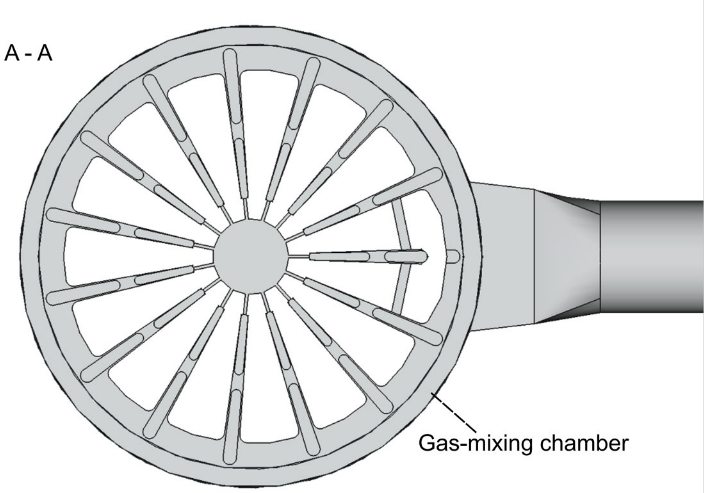

(b) Transversal view.

Figure 68. Key components involved in thermal mixing and considered by the LES model.

5.2.1. Computational domain

The LES computational mesh of the mixing experiment was developed using GMSH [55]. Figure 69 shows the multi-block mesh, including details on the hexahedron blocks in the interior of the gas-mixing channels. Additionally, Figure 70 provides detailed views of the conformal mesh blocks from two perspectives: a top view that includes a closeup of the core hot gas exhaust pipe, and a lateral view that focuses on the outlet pipe of the mixing facility. The developed mesh contains roughly 1.5 million elements. In this preliminary study, each element cast the solution with a third-order polynomial—thus yielding roughly 100 million grid points.

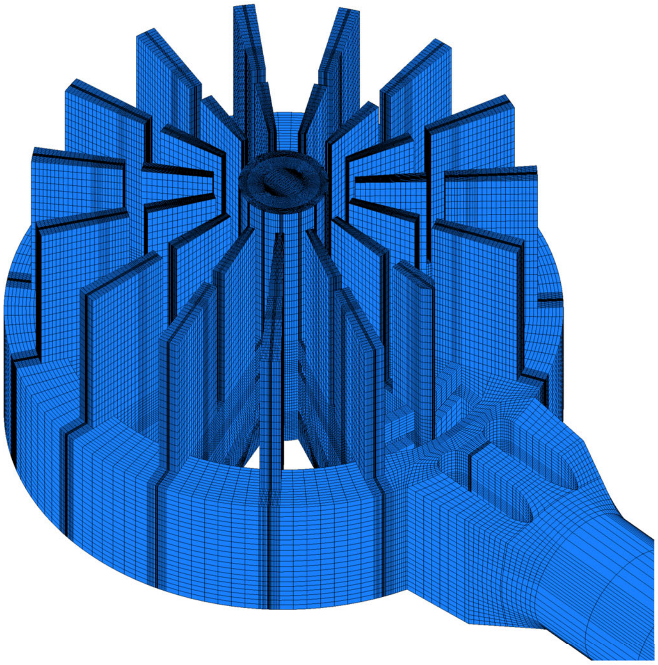

(a) Isometric view of the mesh.

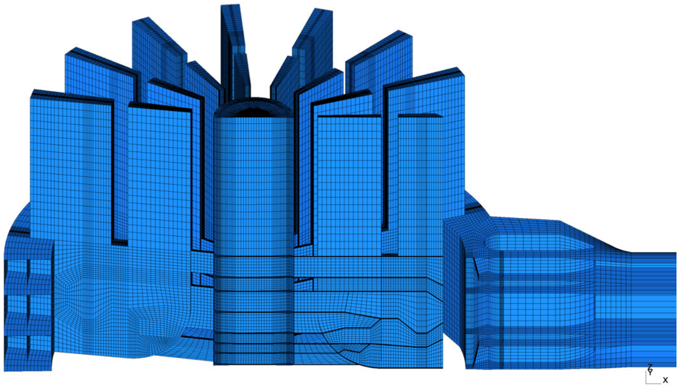

(b) Transversal cross-section of the mesh.

Figure 69. LES mesh of the scaled mixing facility.

5.2.2. Boundaries and flow conditions

The LES model is based on NekRS's incompressible solver and is performed using a dimensionless setup. Figure 71 illustrates the boundary conditions applied to the LES model. The inlets are divided into three categories: the hot inlet, where the hot fluid exiting the core enters the gas-mixing facility; the warm inlet, which primarily accounts for the heated coolant at the core's periphery; and the cold inlet, consisting of coolant used in the moderator. The velocity inlet profiles are implemented based on developed profiles obtained from separate periodic cases. Additionally, the outlet boundary condition considers a constant

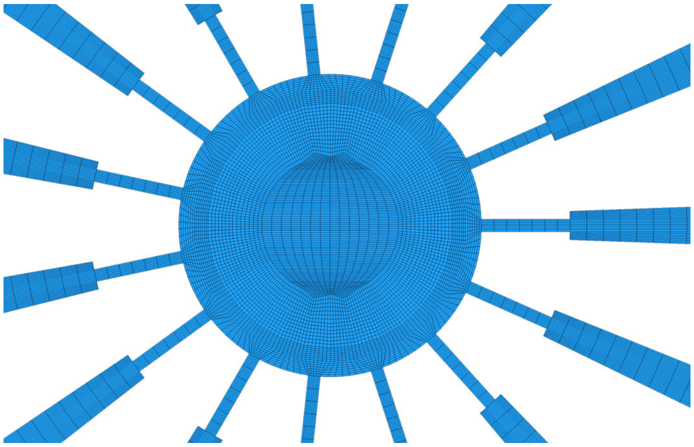

(a) Top view: closeup at the core's exhaust pipe.

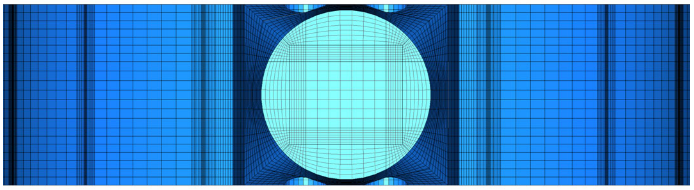

(b) Lateral view: closeup at the outlet pipe of the gas-mixing experiment.

Figure 70. Details of conformal mesh blocks.

pressure and the walls implement a non-slip condition.

The flow is characterized by an outlet Reynolds number of $Re = 400,000$. To ensure the dimensionless setup of the model, the computational domain is scaled such that the outlet diameter is $D = 1$, the fluid density is $\rho = 1$, and the inlet boundary conditions lead to a unity bulk velocity at the outlet pipe. Hence, the flow condition is characterized as the inverse of the dynamic viscosity (i.e., $Re = 1/\mu$).

Lastly, LES employs a Prandtl number of ($Pr = 0.7$) to match the experimental conditions. Normalized temperatures are prescribed at the inlets: the hot inlet has a temperature of ($T = 1$), the warm inlet has a temperature of ($T = 0.25$), and the cold inlet has a temperature of ($T = 0$).

5.2.3. Results

This section presents preliminary results of the LES model. Figure 72 shows the instantaneous velocity field through different planes of the mixing facility. The vertical cross-section (Figure 72a) shows the coolant discharge into the gas-mixing chamber, which is then directed toward the outlet pipe. This view also shows the mixing vanes at the outlet pipe nozzle. These vanes cause a local speed burst that enhances turbulence mixing. Regarding the lateral cross-section, Figure 72b details the vortex formation due to the interaction between lateral flow (hot inlet) and the vertical flow (warm and cold inlets). Additionally, one can also observe the speed burst where the mixing vanes are located at the outlet nozzle.

Figure 73 presents the instantaneous temperature field over the same planes as the previous velocity results. The vertical cross-section (Figure 73a) shows the temperature distribution as the coolant is discharged into the gas-mixing chamber and directed toward the outlet. The temperatures toward the outlet are significantly more uniform in comparison to the upstream locations—in particular, through the gas-mixing channels. The lateral view (Figure 73b) illustrates the thermal mixing effects of the vortices generated by the crossflow.

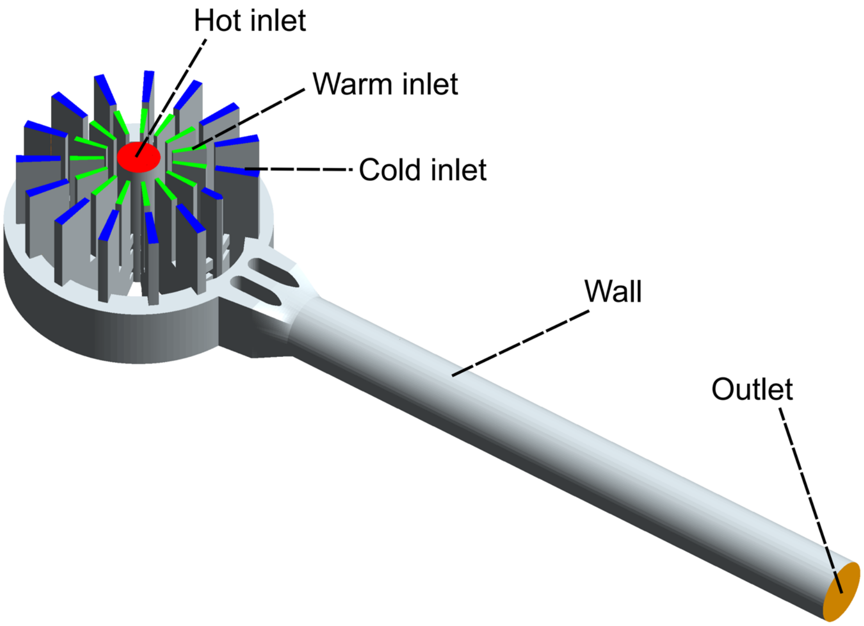

Figure 71. Boundary conditions in the LES model.

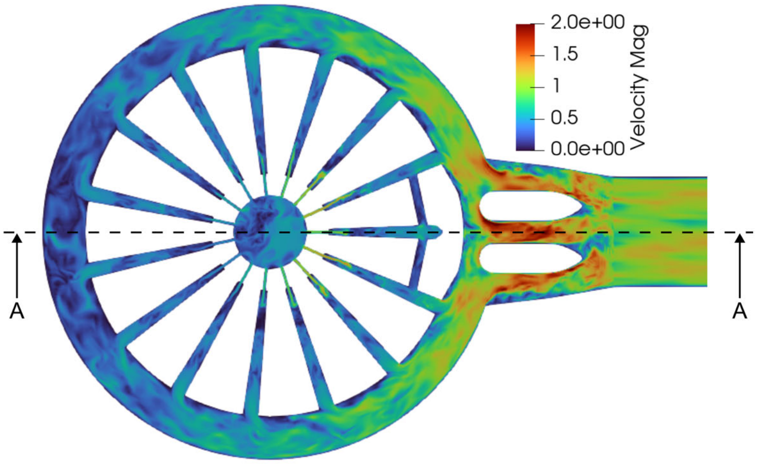

(a) Vertical cross-section.

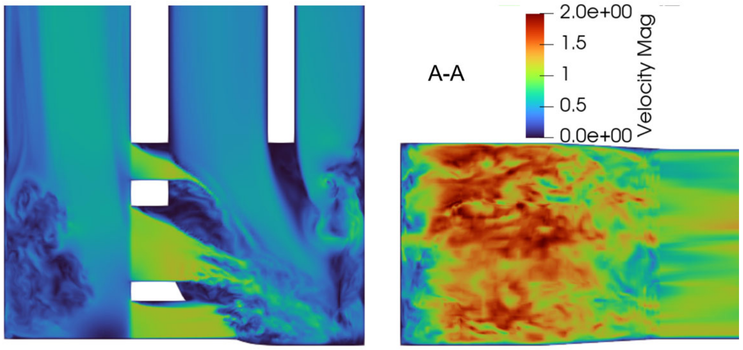

(b) Lateral cross-section.

Figure 72. LES results: instantaneous velocity magnitude.

The formation of the vortexes in these channels is a key aspect for promoting thermal mixing as the coolant enters the the mixing chamber.

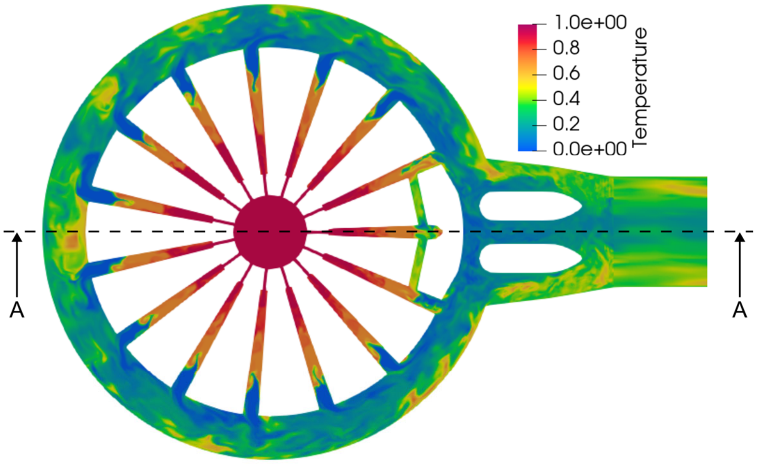

(a) Vertical cross-section.

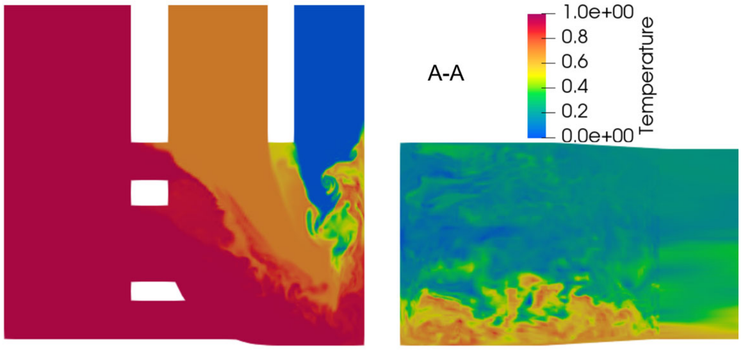

(b) Lateral cross-section.

Figure 73. LES results: instantaneous temperature field.

5.3. Porous Media Simulation

Porous media models are commonly used for intermediate-fidelity modeling of PBRs. These models rely on the use of many closures to approximate unresolved effects. Therefore, it is important to verify the accuracy of these closures for the complex geometries found in PBRs. For this section, the coarse-mesh thermal hydraulics code Pronghorn was used to simulate the hot-gas mixing experiment. Pronghorn's utility and limitations for this geometry were demonstrated and compared with experimental and RANS results. Section 5.3.3 concludes by summarizing the findings and discussing next steps.

5.3.1. Porous Media Introduction

Helium-cooled HTGRs operate with elevated outlet temperatures, often around 750-900°C, enabling efficient power production, hydrogen production, and process heat applications. However, excessive thermal gradients and hot streaking can cause structural issues and lead to worse performance of downstream turbines and intermediate heat exchanges. Numerical investigation of the hot-gas mixing in the lower plenum can inform design decisions that remove problematic thermal gradients and thermal streaking.

Pronghorn, a porous media thermal hydraulics code, holds promise for informing fast iterative design and safety analysis for the lower plenum hot-gas chamber. It is a coarse-mesh code that operates at an intermediate fidelity, with more degrees-of-freedom than a lumped system model but less than a RANS simulation. It is designed for safety analysis, operation studies, transient simulations, and real-time simulations for advanced reactors.

In this work, we demonstrate Pronghorn's capability and we outline the progress toward new frictional pressure loss correlations. Because of the unique geometry in the hot-gas mixing chamber, existing frictional pressure drop correlations likely cannot accurately determine pressure drop through this region. Although when using methods outlined in Subsection 5.3.2, the results from a RANS simulation can be compared with the Pronghorn simulation to identify deficiencies in current pressure drop correlations. Although results from a RANS simulation can inform a Pronghorn model with some utility, it is more desirable to develop new correlations that do not require iteration between the RANS and Pronghorn models. Ultimately, this would enable quick analysis of various lower plenum mixing structures and mass flow rates. Additionally, it would improve validation studies by enabling independent development of fluids modeling approaches.

Section 5.3 is divided into five subsections. Subsection 5.3.2 describes the methods used to generate a fast, accurate porous media model of the hot-gas mixing experiment. Subsection 5.3.3 demonstrates the results for three different test cases and summarizes findings, current utility and next steps.

5.3.2. Porous Media Methods

This subsection begins by introducing the fundamental equations and numerical methods. Second, the homogenized regions and boundary conditions are defined. Third, the viscous (friction) loss and inertial (form) loss correlations are outlined. Finally, interphase heat transfer and effective thermal conductivity are introduced in the context of methods used for ongoing work.

The porous media model makes the following changes to homogenize Navier-Stokes for a representative elementary volume (REV).

$$\epsilon\frac{\partial\rho_f}{\partial t}+\frac{\partial(\epsilon\rho_f u_i)}{\partial x_j}=0 \tag{23}$$

$$\epsilon\frac{\partial(\rho_f u_i)}{\partial t}+\frac{\partial(\epsilon\rho_f u_i u_j)}{\partial x_j}+\epsilon\frac{\partial P}{\partial x_i}+W\rho_f u_i+\frac{\mu\partial^2 u_i}{\partial x_j^2}-\epsilon\rho g_i=0 \tag{24}$$

$$\epsilon\frac{\partial(\rho_f E_f)}{\partial t}+\frac{\partial(\epsilon\rho_f H_f u_i)}{\partial x_j}-\epsilon\rho_f g_i u_i-\frac{\partial}{\partial x_j}(k_f\frac{\partial T_f}{\partial x_j})+\alpha(T_s-T_f)-q_f'''=0 \tag{25}$$

$$(1-\epsilon)\rho_s C_{p,s}\frac{\partial(T_s)}{\partial t}-\frac{\partial}{\partial x_j}(k_f\frac{\partial T_f}{\partial x_j})+\alpha(T_f-T_s)-q_f'''=0 \tag{26}$$

Numerical methods are required to solve for these equations. Pronghorn solves for the REV Navier-Stokes equations by using the finite volume method, which solves the conservation equations at the center of each representative cell.

Critical to the development of a porous media model, porosity is defined as the ratio of the coolant volume to the total volume.

$$\epsilon = \frac{V_{coolant}}{V_{total}} \tag{27}$$

Five REV regions are outlined in Figure 74. The primary consideration when choosing these regions was axial symmetry. Here, the regions correlate with the physical components found in the hot-gas mixing experiment.

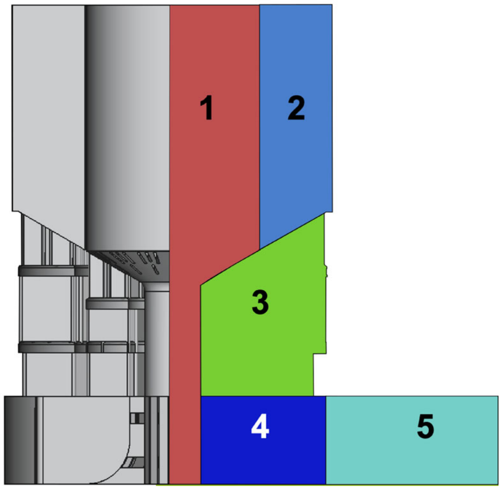

Figure 74. (Left) Physical components. (Right) 2D axisymmetric porous regions.

Each porous region homogenizes the respective volume and represents a 2D axially symmetric plane. As previously outlined, Region 1 represents the hot inlet and the smaller-diameter discharge pipe. Region 2 represents the cold inlet. Region 3 represents the reflector. Region 4 represents the hot-gas mixing chamber, and region 5 represents the outlet pipe.

The porosity is defined for each REV. The coolant volume is extracted from the Star-CCM+ model and divided by the total volume of each region. Because the outlet pipe is not axially symmetric about the RZ axis, region 5 requires a porosity function related to the radial and axial distance from the origin to conserve fluid volume.

Each region is captured by the following coarse-mesh shown in Figure 75.

Boundary conditions can be found in Figure 76.

Axisymmetry is defined along the left-most plane. Slip walls are defined for the two external and the two internal planes. A constant pressure outlet is defined to be equal to atmospheric pressure. Finally, a constant mass flow rate boundary condition is defined for the inlet. In this work, four different mass flow rates are compared to experimental results.

This study explores the application of three different pressure loss correlations: the Blasius, Churchill, and Kerntechnischer Ausschuss (KTA) correlations. Understanding each pressure closure's range of applicability is important when determining the correct application.

The Blasius closure, given by Equation 28, is commonly used to approximate frictional pressure loss of flow in a smooth pipe.

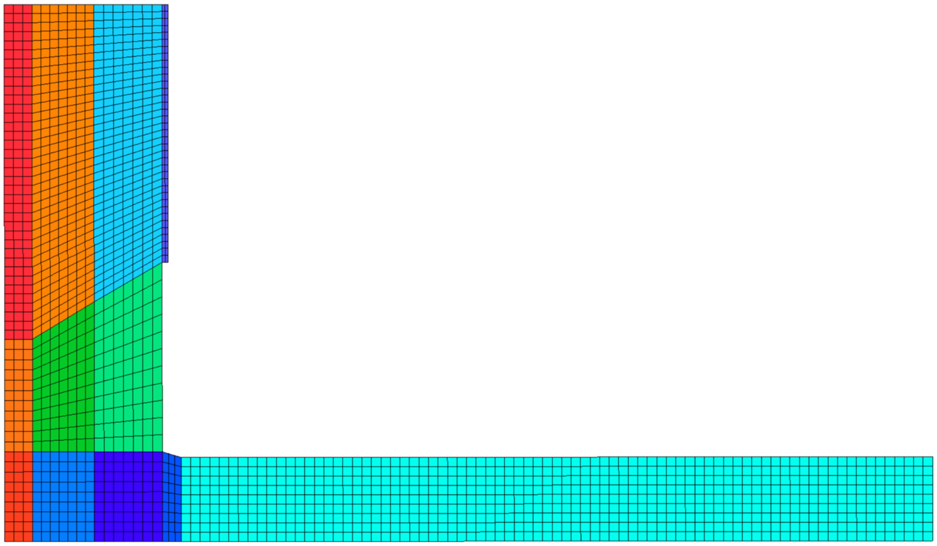

Figure 75. Coarse-grid mesh used for porous media simulations in Pronghorn.

$$f_{Blasius} = \frac{0.316}{Re^{1/4}} \tag{28}$$

The Blasius correlation is used for the hot and cold inlet regions. Blasius is valid for a smooth pipe with a no-slip boundary, a constant free stream velocity, and $3000 < Re < 2 \cdot 10^4$. At higher Reynolds numbers ($2 \cdot 10^4 < Re < 2 \cdot 10^6$), the Blasius correlation is given by $f = \frac{0.184}{Re^{0.2}}$.

The Churchill closure, given by Equation 29, is commonly used to find the pressure drop for transitional and fully developed turbulent flow in a rough pipe.

$$f_{Churchill} = 8\left[\left(\frac{8}{Re}\right)^{12} + (A+B)^{-\frac{3}{2}}\right]^{\frac{1}{12}} \tag{29}$$

where:

$$A = \left[2.457 \cdot \log\left(\frac{1}{\left(\frac{7}{Re}\right)^{0.9} + 0.27\epsilon}\right)\right]^{16}$$

$$B = \left(\frac{37530}{Re}\right)^{16}$$

The Churchill frictional pressure loss correlation is used for the reflector, hot-gas mixing chamber, and outlet region. Churchill is valid for turbulent flow in a pipe, where $2300 < Re < 10^8$ and the relative roughness (ϵ/D) is between 0.00001 and 0.04.

In some experiments, pebbles are included in the bottom of the hot gas region, so they are introduced in this work for completeness and future comparison. Pebbles are modeled in the Discharge Pipe in Pronghorn

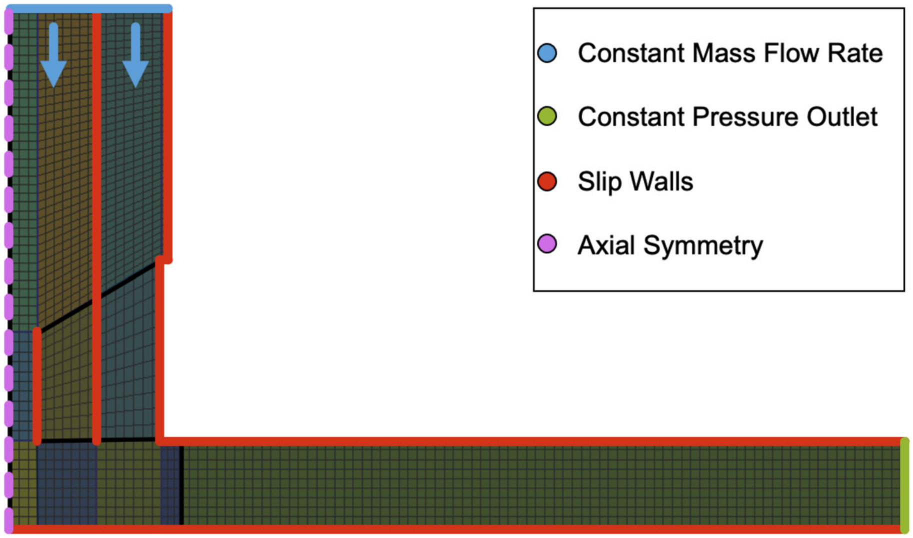

Figure 76. Pronghorn boundary conditions. For this work, mass flow rates of 1.1–5.28 kg/s are modeled, and the constant pressure outlet is equal to 100000 Pa.

by adjusting the porosity and incorporating the KTA closure. This closure determines the total pressure loss, and is defined by Equation 30.

$$\left(\frac{\Delta P}{L}\right)_{KTA} = \left(\frac{320}{Re_m} + \frac{6}{Re_m^{0.1}}\right)\frac{1-\epsilon}{\epsilon^3}\frac{\rho^2 v_s^2}{D_p}\frac{1}{2\rho} \tag{30}$$

Region 3 attempts to homogenize 328 flow channels with hydraulic diameters that range from 0.0128 to 0.0451 m. Additionally, this region aims to characterize the flow through two regions where expansion, contraction, and crossflow occur. Region 4 attempts to homogenize 15 mixing vanes. Each mixing vane has two inlets at the top from the reflector, three inlets at the side from the Discharge Pipe, and one outlet. Flow at the vane outlet undergoes expansion and is directed toward the outlet pipe. Additionally, each vane outlet has a different pressure that varies with the distance from the outlet pipe. The mixing vane closest to the outlet is the one exception. To encourage better mixing, the outlet of this vane is redirected to the two adjacent mixing vanes.

Existing closures are likely insufficient for the complex geometries in Regions 3 and 4. To develop improved closures, the existing closures must be benchmarked. Three benchmark cases are outlined in Table 18.

Table 18. Three Pronghorn benchmark cases.

Benchmark	**Blasius**	**Churchill**	**KTA**	**RANS Informed**
1	✓	✓	✓	X
2	✓	✓	X	X
3	✓	✓	X	✓

Benchmarks 1 and 2 provide baseline results for comparison between Pronghorn, RANS, LES, and the experiment. Since not all the lower plenum experiments include pebbles in the Discharge Pipe, the simulation was run both with and without them so as to analyze their effect on the resulting flow. Benchmark 1 was aimed at highlighting the effect pebbles can have on the pressure distribution. Benchmark 2 was aimed at demonstrating pressure loss through the hot-gas mixing experiment, without making any reference to the RANS model. Benchmark 3 utilizes the RANS model and aims to account for inertial pressure losses between regions that went unaccounted for by Benchmark 2.

Unlike the KTA closure, the Blasius and Churchill drag closures do not account for minor pressure loss through or between the respective regions. The inertial losses are expressed by Equation 31:

$$\Delta P = \frac{1}{2} k \rho \vec{v}^2 \tag{31}$$

where k is the form loss factor and $\vec{v}$ is the interstitial velocity. Currently, two methods are used to account for inertial pressure losses. Benchmarks 1 and 2 approximate k by summing k factors commonly used in piping systems. These correlations, however, are intended for use in single pipes with a constant flow area. In the lower plenum geometry, the representative volumes contain many expansions and contractions that are lost when the region is homogenized for porous media. Benchmark 3 aims to account for these missing losses by determining the form loss coefficients to match the RANS pressure drop across each region interface. This side set pressure drop informs the form loss factor. The k factor for each scenario is shown in Table 19.

Table 19. Minor loss factors that inform pressure drop at the boundaries of Regions 3 and 4.

Benchmark	Region 3, top	Region 3, bottom	Region 4, left	Region 4, right
1	3	2	4.5	6.75
2	3	2	4.5	6.75
3	<10>	<5>	54	17.72

5.3.3. Porous Media Results

This subsection outlines the initial Pronghorn results and describes the methods used to improve the accuracy of pressure drop correlations. Additionally, Pronghorn benchmarks are compared with experimental results.

The pressure field in Benchmark 1 is shown in Figure 77. Here, it can be seen that the majority of the pressure losses occur between regions of different porosity. Additionally, the pressure gradient is highest in the discharging chute where the pebbles are included. This is as was expected, as inclusion of pebbles drastically increases the flow resistance in this region.

Conversion of the lower plenum geometry into a homogenized RZ model results in many flow expansions and contractions that are unresolved. These geometric features, however, can have a major impact on the resulting pressure drop. Failing to include the effects of these features in the Pronghorn pressure drop closure therefore results in severe underpredictions of the pressure drop, as seen in Figure 79. Including pebbles in the defueling chute does lead to slightly higher pressure drops, but there yet remains a large underprediction of the pressure drop in Pronghorn.

A high-to-low correlation development methodology can be applied to use the RANS or LES simulations to inform improved porous media closures. An overview of a typical high-to-low development process is shown in Figure 78. For this work, the RANS results are used to inform the form loss coefficients between each of the regions in the porous media model. This helps better capture the expansions and contractions that are not resolved in Pronghorn. The pressure drop as a function of flow rate is shown in Figure 79, revealing

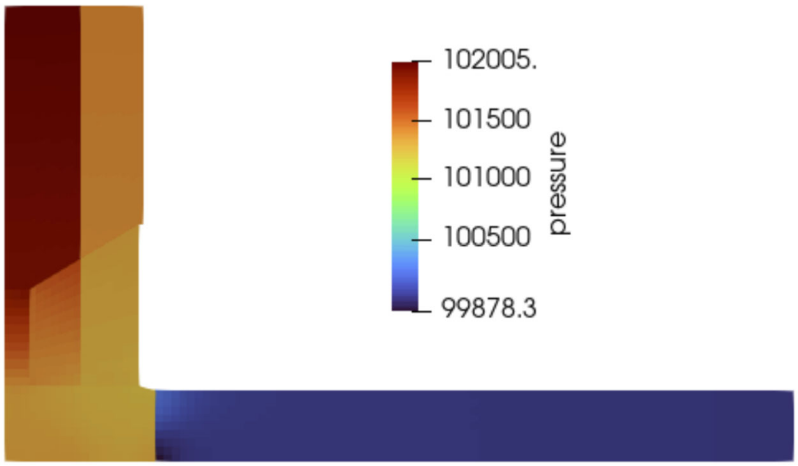

Figure 77. Pronghorn Benchmark 1 pressure results for a mass flow rate of 4.8 kg/s. The pressure field is shown in Pascals.

that adjusting the form loss coefficients greatly improves the resulting pressure drop in Pronghorn. In this work, this process merely serves a demonstrative purpose, as the form loss coefficients were simply increased until the pressure drop in Pronghorn matched the pressure drop in RANS. A more ideal method would be to use the RANS flow field to determine a more generalized correlation for application in Pronghorn. This superior approach will be applied in the future to more comprehensively improve lower-plenum modeling capabilities in porous media models. Nonetheless, this result demonstrates the use of high-to-low correlation development for improving lower-fidelity models.

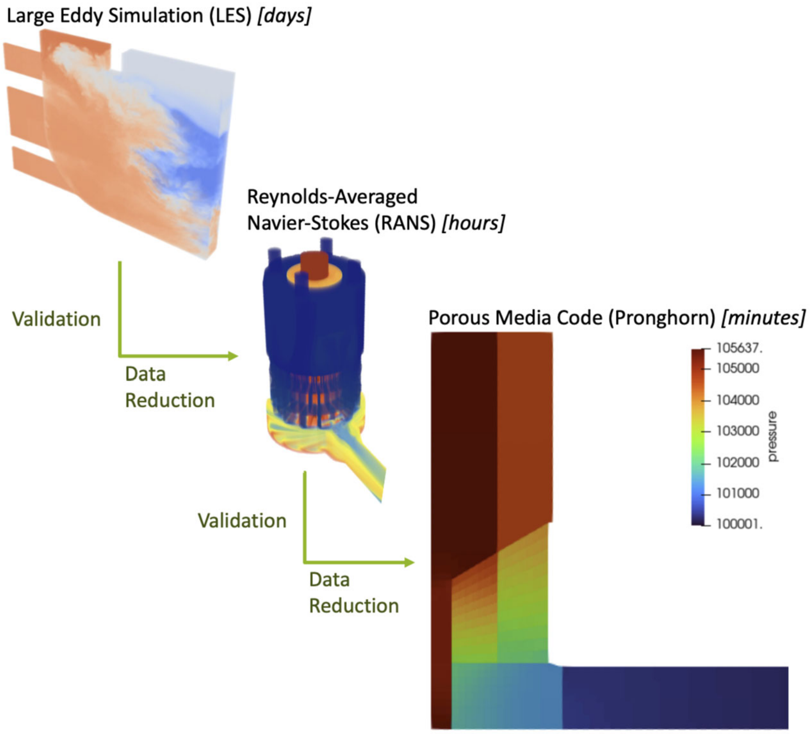

Figure 78. Illustration of LES results informing RANS, which then informed the Pronghorn Benchmark 3 results for a mass flow rate of 4.8 kg/s. The pressure field is shown in Pascals at the bottom right.

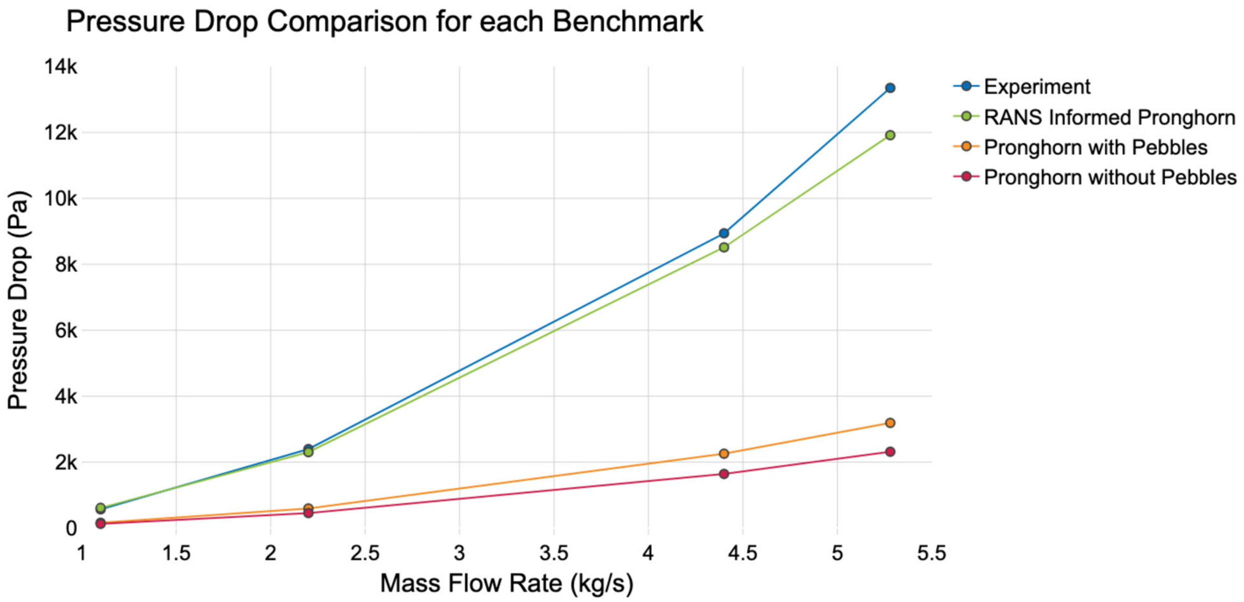

Figure 79. Each Pronghorn benchmark pressure drop is compared for four different mass flow rates (1.1, 2.2, 4.4, and 5.28 [kg/s]).

6. CONCLUSIONS

This report summarized the recent progress on CFD V&V efforts in the ART-GCR program. Three HTGR phenomena were targeted for this work: RCCS performance, core bypass flow, and lower plenum mixing. Simulations were performed at various levels of fidelity, including LES, RANS, and porous media. The results can contribute to bencharmking efforts within the GIF CMVB in order to further leverage these simulations and gain an enhanced understanding of how modeling assumptions or the use of different tools can affect comparisons made with experimental data.

Simulation of the UW-Madison RCCS facility was performed using both LES and RANS methods. LES was only performed on the RCCS to decide the RANS turbulence modeling strategy for forced convection simulations. Then the RANS model of the experimental facility was developed, and includes the RCCS and heated cavity (mimics the reactor cavity in an HTGR). RANS simulations were performed for both forced and natural convection experimental conditions at multiple heater power levels. Overall, good agreement was achieved between the RANS predictions and the experimental data. This investigation highlighted the importance of choosing a proper turbulence model that is appropriate for the flow conditions, as models that performed well for forced convection did not perform as well for natural convection. Therefore, an additional RANS turbulence model sensitivity study was performed for natural convection simulations. Additionally, the importance of modeling radiative heat transfer was demonstrated, as radiative heat transfer was found to account for roughly 75% of all the heat transfer between the heaters and riser channels in the forced convection case, and for roughly 85% in the natural convection case.

V&V of core bypass flow predictions was performed using experimental data from the INL MIR facility and the SNU/KAERI unit cell facility. As with the RCCS investigation, LES and RANS models were chosen as the methods for investigation. For the INL MIR facility, both the LES and RANS models agreed well with experimental measurements of bypass flow, pressure drop, and PIV velocity. LES consistently saw slightly better agreement than did the RANS model, though both were sufficiently accurate for engineering purposes. The RANS simulation of the SNU unit-cell facility yielded similarly good agreement to experimental measurements of bypass flow. The SNU facility consisted of three flow configurations representing different combinations of fuel and reflector blocks. It was observed that the cases with fewer fuel blocks—and thus fewer coolant channels—saw worse agreement with the experimental data than did the case involving a uniform arrangement of fuel blocks. This difference was attributed to complex vortices that occur in the inlet and outlet plenum and that are not well captured by the RANS models. The LES models remain under development, although progress has been made in developing a computational mesh, along with some preliminary calculations. Future work will continue these LES model developments, and will compare LES to both RANS and the experimental data.

Finally, simulation of the lower plenum mixing facility is being performed with LES, RANS, and porous media models. This report mainly focused on progress with the LES and porous media methods, as a previous report had already documented the progress made with RANS methods [59]. An all-hexahedral mesh was created for the lower-plenum mixing facility, and preliminary LES simulations have been performed. These preliminary results will be used to improve the mesh before production-level simulations are conducted. Additionally, a porous media model of the lower-plenum mixing facility was developed and then compared against RANS and the experimental data. It was found that existing closures severely underestimate the pressure drop in the lower plenum as a result of homogenizing the geometry. This homogenization leads to a lack of form losses that typically dominate in this complex geometry. Initial efforts into high-to-low model development demonstrated that the RANS simulation can be used to improve pressure drop predictions in the porous media model.

Page intentionally left blank

7. REFERENCES

[1] A. Leonard, “Energy cascade in large-eddy simulations of turbulent fluid flows,” in *Turbulent Diffusion in Environmental Pollution* (F. Frenkiel and R. Munn, eds.), vol. 18 of *Advances in Geophysics*, pp. 237–248, Elsevier, 1975.

[2] V. Coppo Leite, “Towards temperature field reconstruction, an innovative method for advanced reactors monitoring,” 2023.

[3] S. B. Pope, *Turbulent Flows*. Cambridge University Press, 2000.

[4] E. Merzari, A. Obabko, P. Fischer, and M. Aufiero, “Wall resolved large eddy simulation of reactor core flows with the spectral element method,” *Nuclear Engineering and Design*, vol. 364, p. 110657, 2020.

[5] *Performance Analysis of Nek5000 for Single-Assembly Calculations*, vol. Volume 2: Development and Applications in Computational Fluid Dynamics; Industrial and Environmental Applications of Fluid Mechanics; Fluid Measurement and Instrumentation; Cavitation and Phase Change of *Fluids Engineering Division Summer Meeting*, 07 2018. V002T09A031.

[6] E. Merzari, V. Coppo Leite, J. Fang, D. Shaver, M. Min, S. Kerkemeier, P. Fischer, and A. Tomboulides, “Energy Exascale Computational Fluid Dynamics Simulations With the Spectral Element Method,” *Journal of Fluids Engineering*, vol. 146, p. 041105, 02 2024.

[7] P. SPALART and S. ALLMARAS, *A one-equation turbulence model for aerodynamic flows*.

[8] S. D. I. Software, “Simcenter STAR-CCM+ User Guide, version 2021.1,” in *Adaptive Mesh Refinement for Overset Meshes*, pp. 3067–3070, Siemens, 2021.

[9] “The prediction of laminarization with a two-equation model of turbulence,” *International Journal of Heat and Mass Transfer*, vol. 15, no. 2, pp. 301–314, 1972.

[10] W. Rodi, “Experience with two-layer models combining the k-e model with a one-equation model near the wall,” in *29th Aerospace Sciences Meeting*, no. AIAA 91-0216, (Reno, NV), AIAA, January 7-10 1991.

[11] T.-H. Shih, W. Liou, A. Shabbir, Z. Yang, and J. Zhu, “A new k-ϵ eddy viscosity model for high reynolds number turbulent flows – model development and validation,” Tech. Rep. TM 106721, NASA, 1994.

[12] D. C. Wilcox, *Turbulence Modeling for CFD*. La Canada, CA: DCW Industries, 1995.

[13] D. Wilcox, *Turbulence Modeling for CFD*. DCW Industries, Inc, 2nd ed., 1998.

[14] F. Menter, “Two-equation eddy-viscosity turbulence modeling for engineering applications,” *AIAA Journal*, vol. 32, no. 8, pp. 1598–1605, 1994.

[15] P. R. Spalart and C. L. Rumsey, “Effective inflow conditions for turbulence models in aerodynamic calculations,” *AIAA Journal*, vol. 45, no. 10, pp. 2544–2553, 2007.

[16] S. Sarkar and L. Balakrishnan, “Application of a reynolds-stress turbulence model to the compressible shear layer,” NASA Contractor Report ICASE Report No. 90-18, NASA CR 182002, NASA Langley Research Center, Hampton, VA, 1990.

[17] C. G. Speziale, S. Sarkar, and T. B. Gatski, “Modelling the pressure-strain correlation of turbulence: an invariant dynamical systems approach,” *Journal of Fluid Mechanics*, vol. 227, pp. 245–272, 1991.

[18] D. M. Wells, "Overview of cfd round robin benchmark of the high fidelity fuel rod bundle nestor experimental data," 2015.

[19] D. Lisowski, Q. Lv, B. Alexandreanu, Y. Chen, R. Hu, and T. Sofu, "An overview of non-lwr vessel cooling systems for passive decay heat removal," tech. rep., Argonne National Laboratory (ANL), IL (United States), may 2021.

[20] Z. Dong, Z. Zhang, Y. Dong, L. Shi, X. Huang, Y. Zhu, and D. Jiang, "Testing the feasibility of multi-modular design in an htr-pm nuclear plant," *Nature Communications*, vol. 16, no. 1, p. 2778, 2025.

[21] Z. Zhang, Y. Dong, F. Li, X. Huang, Y. Zheng, Z. Dong, H. Zhang, Z. Chen, and X. Li, "Loss-of-cooling tests to verify inherent safety feature in the world's first htr-pm nuclear power plant," *Joule*, vol. 8, no. 7, pp. 2146–2159, 2024.

[22] D.-H. Shin, C. S. Kim, G.-C. Park, and H. K. Cho, "Experimental analysis on mixed convection in reactor cavity cooling system of htgr for hydrogen production," *International Journal of Hydrogen Energy*, vol. 42, no. 34, pp. 22046–22053, 2017.

[23] D. D. Lisowski, C. D. Gerardi, D. J. Kilsdonk, N. C. Bremer, S. W. Lomperski, R. Hu, A. R. Kraus, M. D. Bucknor, Q. Lv, T. Lee, and M. T. Farmer, "Final project report on rccs testing with air-based nstf," tech. rep., Argonne National Laboratory, 8 2016.

[24] S. Sulaiman, *Experimental Investigations of Flow Behavior Inside the Upper Plenum of TAMU Air-Cooled Reactor Cavity Cooling System*. PhD thesis, 2015.

[25] M. Corradin, M. Anderson, M. Muci, Y. Hassan, A. Dominguez, A. Tokuhiro, and K. Hamman, "Thermal-hydraulic analysis of an experimental reactor cavity cooling system with air. part i: Experiments; part ii: Separate effects tests and modeling," tech. rep., Argonne National Laboratory, 10 2014.

[26] D. D. Lisowski, C. D. Gerardi, R. Hu, D. J. Kilsdonk, N. C. Bremer, S. W. Lomperski, A. R. Kraus, M. D. Bucknor, and M. T. Farmer, "Water nstf design, instrumentation, and test planning," tech. rep., Argonne National Laboratory, 8 2017.

[27] D. D. Lisowski, A. R. Kraus, M. D. Bucknor, R. Hu, and M. T. Farmer, "Experimental observations of natural circulation flow in the nstf," *Nuclear Engineering and Design*, vol. 306, pp. 124–132, 2016. 7th International Topical Meeting on High Temperature Reactor Technology (HTR 2014).

[28] S. Lomperski, W. Pointer, C. Tzanos, T. Y. Wei, and A. Kraus, "Generation iv nuclear energy system initiative; air-cooled option rccs studies and nstf preparation.," tech. rep., Argonne National Lab.(ANL), Argonne, IL (United States), 2012.

[29] S. A. Sulaiman, E. E. Dominguez-Ontiveros, T. Alhashimi, J. L. Budd, M. D. Matos, and Y. A. Hassan, "Design considerations and experimental observations for the TAMU air-cooled reactor cavity cooling system for the VHTR," *AIP Conference Proceedings*, vol. 1659, p. 030002, 04 2015.

[30] R. Hu, A. Kraus, M. Bucknor, Q. Lv, and D. Lisowski, "Final project report on computational modeling and analysis of air-based nstf," tech. rep., Argonne National Laboratory, 6 2016.

[31] R. Hu, D. D. Lisowski, M. D. Bucknor, A. R. Kraus, and Q. Lv, "Ambient and building condition effects modeling of air-cooled natural circulation systems," *Applied Thermal Engineering*, vol. 137, pp. 23–31, 2018.

[32] Y. A. H. Angelo Frisani and V. M. Ugaz, “Computational fluid dynamics analysis of very high temperature gas-cooled reactor cavity cooling system,” *Nuclear Technology*, vol. 176, no. 2, pp. 238–259, 2011.

[33] O. Koekemoer, C. du Toit, and P. Niemand, “Investigation into different 1d/3d co-simulation methodologies applied to a natural circulation loop,” *Nuclear Engineering and Design*, vol. 390, p. 111698, 2022.

[34] R. Freile, M. Tano, P. Balestra, S. Schunert, and M. Kimber, “Improved natural convection heat transfer correlations for reactor cavity cooling systems of high-temperature gas-cooled reactors: From computational fluid dynamics to pronghorn,” *Annals of Nuclear Energy*, vol. 163, p. 108547, 2021.

[35] S.-Y. Kim, C.-S. Kim, and H. K. Cho, “Local flow structure and turbulence quantities inside a heated rectangular riser in turbulent forced and mixed convection heat transfers,” *Experimental Thermal and Fluid Science*, vol. 122, p. 110297, 2021.

[36] “CUBIT.” `https://cubit.sandia.gov`, 2022.

[37] S. Dong and J. Shen, “A pressure correction scheme for generalized form of energy-stable open boundary conditions for incompressible flows,” *Journal of Computational Physics*, vol. 291, pp. 254–278, 2015.

[38] M. Min, Y.-H. Lan, P. Fischer, T. Rathnayake, and J. Holmen, “Nek5000/rs performance on advanced gpu architectures,” *Frontiers in High Performance Computing*, vol. Volume 2 - 2024, 2025.

[39] E. Merzari, V. Coppo Leite, J. Fang, D. Shaver, M. Min, S. Kerkemeier, P. Fischer, and A. Tomboulides, “Energy Exascale Computational Fluid Dynamics Simulations With the Spectral Element Method,” *Journal of Fluids Engineering*, vol. 146, p. 041105, 02 2024.

[40] M. Wolfstein, “The velocity and temperature distribution in one-dimensional flow with turbulence augmentation and pressure gradient,” *International Journal of Heat and Mass Transfer*, vol. 12, pp. 301–318, 1969.

[41] P. Durbin, “A reynolds stress model for near-wall turbulence,” *Journal of Fluid Mechanics*, vol. 249, no. 1, pp. 465–498, 1993.

[42] R. Manceau, “Recent progress in the development of the elliptic blending reynolds-stress model,” *International Journal of Heat and Fluid Flow*, vol. 51, pp. 195–220, 2015. Theme special issue celebrating the 75th birthdays of Brian Launder and Kemo Hanjalic.

[43] S. Okyay, D. Reger, V. Coppo Leite, E. Merzari, P. Balestra, and G. Strydom, “High-fidelity forced convection simulations of the university of wisconsin-madison air-cooled reactor cavity cooling system,” *Nuclear Engineering and Design*, 2025. Accepted for publication.

[44] C. Viljoen, S. Sen, F. Reitsma, O. Ubbink, P. Pohl, and H. Barnert, “The re-evaluation of the avr melt-wire expeirmrent using modern methods with specific focus on bounding the bypass flow effects,” in *Proc. Int. Conf. on High Temperature Reactor Technology (HTR2008)*, (Washington D.C. September 28–October 1), American Society of Mechanical Engineers, 2008.

[45] H. Gottaut and K. Kruger, “Results of experiments at the avr reactor,” *Nuclear Engineering and Design*, vol. 121, pp. 143–153, 1990.

[46] J. van Rensburg and M. Kleingeld, “Investigating leakage and bypass flows in an htr using a cfd methodology,” *Nuclear Engineering and Design*, vol. 241, pp. 4960–4971, 2011.

[47] S. Ximing, C. Zhipeng, S. Jun, L. Yuan, Z. Yanhua, L. Fu, and S. Lei, “Cfd investigation of bypass flow in htr-pm,” *Nuclear Engineering and Design*, vol. 329, pp. 147–155, 2018.

[48] Y. Zhou, X. Sun, P. Hao, F. Li, L. Shi, Y. Liu, F. He, Y. Dong, and Z. Zhang, “Performance of thermmal mixing structure of htr-pm regarding bypass flow and power effect,” *Nuclear Engineering and Design*, vol. 335, pp. 291–302, 2018.

[49] S. Yoon, C. Jin, M. Kim, and G. Park, “Experimental and computational assessment of core bypass flow in block-type very high temperature reactor,” *Nuclear Technology*, vol. 175, 2011.

[50] R. Schultz, M. Kim, R. Vilim, C. Park, and Y. Hassan, “Experimental and analytic study on the core bypass flow in a very high temperature reactor,” Tech. Rep. INL/EXT-12-24603, Idaho National Laboratories, 2012.

[51] P. Sabharwall, T. Conder, R. Skifton, C. Stoots, and E. S. Kim, “Piv uncertainty methodologies for cfd code validation at the mir facility,” Tech. Rep. INL/EXT-12-27728, Idaho National Laboratories, 2013.

[52] T. Conder, *Particle image velocimetry measurements in a representative gas-cooled prismatic reactor model for the estimation of bypass flow*. PhD thesis, University of Idaho, 2012.

[53] D. Reger, E. Merzari, P. Balesetra, S. Schunert, Y. Hassan, and S. King, “Direct numerical simulation and large eddy simulation of a 67-pebble bed expeirment,” *Nuclear Technology*, vol. 210, 2024.

[54] S.-J. Yoon, C.-Y. Jin, M.-H. Kim, and G.-C. Park, “Experimental and computational assessment of core bypass flow in block-type very high temperature reactor,” *Nuclear Technology*, vol. 175, no. 2, pp. 419–434, 2011.

[55] C. Geuzaine and J.-F. Remacle, “Gmsh: A 3-d finite element mesh generator with built-in pre- and post-processing facilities,” *International Journal for Numerical Methods in Engineering*, vol. 79, no. 11, pp. 1309–1331, 2009.

[56] “Multi-Component RANS - Nek5000 documentation.” `https://nek5000.github.io/NekDoc/tutorials/multi_rans.html`, 2023.

[57] G. Damm and R. Wehrlein, “Simulation tests for temperature mixing in a core bottom model of the htr-module,” *Nuclear Engineering and Design*, vol. 137, no. 1, pp. 97–105, 1992.

[58] Y. Zhou, P. Hao, F. Li, L. Shi, F. He, Y. Dong, and Z. Zhang, “Experiment study on thermal mixing performance of htr-pm reactor outlet,” *Nuclear Engineering and Design*, vol. 306, pp. 186–191, 2016. 7th International Topical Meeting on High Temperature Reactor Technology (HTR 2014).

[59] S. Okyay, J. Cogliati, V. C. Leite, D. Reger, P. Balestra, and G. Strydom, “Summary report of the fy24 doe contributions to the gif vhtr cmvb,” Tech. Rep. INL/RPT-24-80355, Idaho National Laboratories, 2024.